Department of Applied Physics

Lasing and Bose-Einstein condensation in plasmonic lattices at weak and strong coupling regimes

Aaro I. Väkeväinen

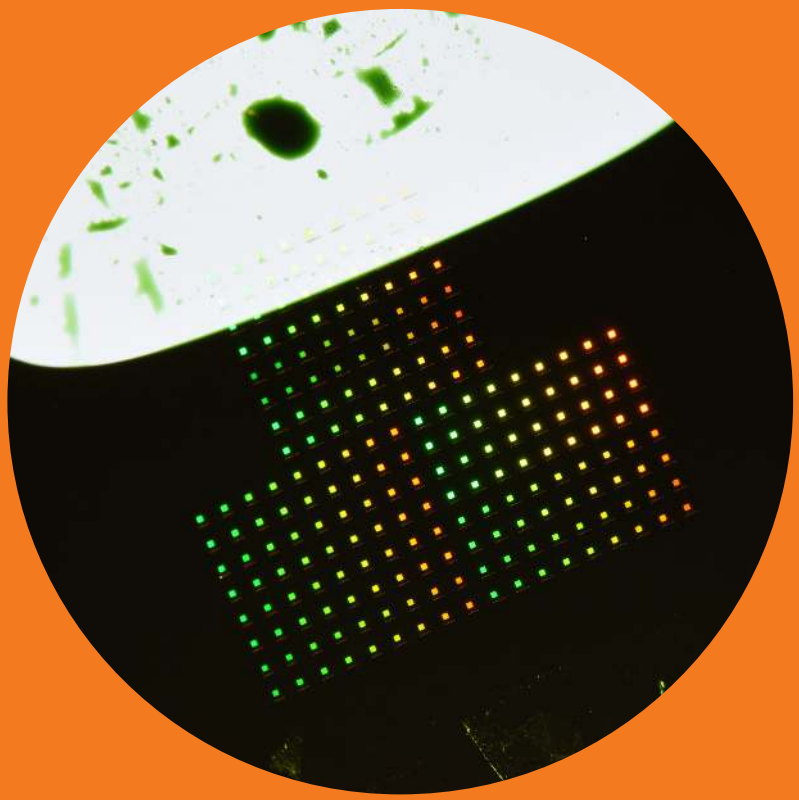

Aalto University

DOCTORAL DISSERTATIONS

Aalto University publication series
DOCTORAL DISSERTATIONS 227/2019

Lasing and Bose-Einstein condensation in plasmonic lattices at weak and strong coupling regimes

Aaro I. Väkeväinen

A doctoral dissertation completed for the degree of Doctor of Science (Technology) to be defended, with the permission of the Aalto University School of Science, at a public examination held in the lecture hall M1 of the school on the 20th of December 2019 at 12.

Aalto University
School of Science
Department of Applied Physics
Quantum Dynamics

Supervising professor
Prof. Päivi Törmä, Aalto University, Finland

Thesis advisor
Prof. Päivi Törmä, Aalto University, Finland

Preliminary examiners
Prof. Jan Klaers, University of Twente, The Netherlands
Prof. Humeyra Caglayan, Tampere University, Finland

Opponent
Prof. Lukas Novotny, ETH Zurich, Switzerland

Aalto University publication series
DOCTORAL DISSERTATIONS 227/2019

ISBN 978-952-60-8860-0 (printed)
ISBN 978-952-60-8861-7 (pdf)
ISSN 1799-4934 (printed)
ISSN 1799-4942 (pdf)
http://urn.fi/URN:ISBN:978-952-60-8861-7

Unigrafia Oy
Helsinki 2019

Finland

NORDIC SWAN ECOLABEL
Printed matter
4041-0619

Aalto University

Abstract

Aalto University, P.O. Box 11000, FI-00076 Aalto www.aalto.fi

Author
Aaro I. Väkeväinen

Name of the doctoral dissertation
Lasing and Bose-Einstein condensation in plasmonic lattices at weak and strong coupling regimes

Publisher School of Science

Unit Department of Applied Physics

Series Aalto University publication series DOCTORAL DISSERTATIONS 227/2019

Field of research Nano-optics, Quantum physics

Manuscript submitted 17 June 2019 **Date of the defence** 20 December 2019

Permission for public defence granted (date) 22 August 2019 **Language** English

☐ **Monograph** ☒ **Article dissertation** ☐ **Essay dissertation**

Abstract

Plasmonics takes advantage of the coupling of light to charge oscillations in metals, which enables breaking the diffraction limit and confining the optical fields in sub-wavelength volumes. The extreme field confinement can greatly enhance the light-matter interaction of photons and quantum emitters, such as atoms and molecules. In this dissertation, I have studied metal nanoparticles arranged in regular two-dimensional lattices, combined with organic dye molecules. The aim is to study strong light-matter interaction as well as lasing and condensation phenomena in these plasmonic lattices.

I have fabricated the nanoparticle arrays with electron beam lithography that allows precise control of the shape and size of the nanoparticle, and periodicity and geometry of the lattice. Optical modes of the plasmonic lattices are characterized by white light transmission and reflection measurements. Angular and spatial distribution of the photoluminescence intensity is measured, together with the corresponding spectra, under optical excitation of 50 fs laser pulses. I have developed a rate-equation model to understand the dynamics of stimulated processes.

In Publication I, we show strong-coupling between the lattice modes and the molecular excitations. Lasing action in both bright and dark modes of the plasmonic lattice is demonstrated in Publication II. In Publication III, we probe the dynamics of ultrafast laser pulse generation and observe a modulation speed of more than 100 GHz. The pulse build-up time and pulse duration is measured with a double-pump spectroscopy technique that utilizes the non-linearity of photoluminescence at the lasing threshold.

In Publication IV, we demonstrate Bose-Einstein condensation of excitations in the plasmonic lattice, the first realization of condensation in plasmonic systems. We establish a measurement scheme that provides a direct access for observing thermalization and the accumulation of macroscopic population to the energy ground state. The scheme utilizes open-cavity character and propagating modes in the plasmonic lattice. Thermalization is explained with recurrent absorption-emission cycles in the dye molecules forming a thermal bath, in the weak coupling regime.

In Publication V, we achieve a Bose-Einstein condensate of strongly-coupled lattice plasmons. This condensate is hundred-thousand fold brighter in luminescence intensity compared to the first one. We observe a distinct thermalized population distribution extending over one decade, in time integrated luminescence signal. Multiple condensation peaks are observed at the lowest energy states with a thermal tail at higher energies that follows Maxwell-Boltzmann distribution at room temperature (333 K). The thermalization occurs in a 200 fs timescale, which is explained with stimulated processes and strong coupling. Room-temperature operation, significant robustness and high luminescence of the samples provide an excellent platform for future studies of luminous driven-dissipative condensates, non-equilibrium quantum dynamics and topological photonics.

Keywords plasmonics, strong coupling, nanoparticle array lasers, Bose-Einstein condensation

ISBN (printed) 978-952-60-8860-0 **ISBN (pdf)** 978-952-60-8861-7

ISSN (printed) 1799-4934 **ISSN (pdf)** 1799-4942

Location of publisher Helsinki **Location of printing** Helsinki **Year** 2019

Pages 280 **urn** http://urn.fi/URN:ISBN:978-952-60-8861-7

Aalto-yliopisto

Tiivistelmä

Aalto-yliopisto, PL 11000, 00076 Aalto www.aalto.fi

Tekijä
Aaro I. Väkeväinen

Väitöskirjan nimi
Laserointi ja Bosen-Einsteinin kondensaatio plasmonihiloissa heikon ja vahvan kytkennän alueella

Julkaisija Perustieteiden korkeakoulu

Yksikkö Teknillisen fysiikan laitos

Sarja Aalto University publication series DOCTORAL DISSERTATIONS 227/2019

Tutkimusala Nano-optiikka, Kvanttifysiikka

Käsikirjoituksen pvm 17.06.2019 **Väitöspäivä** 20.12.2019

Väittelyluvan myöntämispäivä 22.08.2019 **Kieli** Englanti

☐ **Monografia** ☒ **Artikkeliväitöskirja** ☐ **Esseeväitöskirja**

Tiivistelmä

Plasmoniikka hyödyntää valon kytkeytymistä elektronien värähtelyihin metallisissa nanorakenteissa mahdollistaen sähkömagneettisten kenttien keskittämisen valon aallonpituutta pienempiin tilavuuksiin. Energian lokalisaatio vahvistaa merkittävästi valon ja materian vuorovaikutusta. Tässä väitöskirjassa tutkin metallisia nanopartikkelihiloja, jotka on päällystetty kerroksella väriainemolekyylejä. Tavoitteena on tutkia hilan optisten muotojen ja molekyylien vahvaa kytkentää, sekä laserointia ja kondensoitumista.

Olen valmistanut nanopartikkelihilat elektronisuihkulitografialla, joka mahdollistaa yksittäisen nanopartikkelin muodon ja koon, sekä hilaperiodin ja geometrian tarkan kontrolloinnin nanometrimittakaavassa. Karakterisoin hilan optiset resonanssit transmissio ja reflektiomittauksilla. Mittaan näytteen säteilyintensiteetin paikka- ja kulmajakauman, sekä vastaavat luminesenssispektrit, kun fluoresoivaa väriainetta viritetään 50 fs mittaisilla laserpulsseilla. Mallinnan näytteessä tapahtuvia stimuloituja prosesseja rakentamallani tasapainoyhtälömallilla.

Julkaisussa I näytämme vahvan kytkennän hilan optisten resonanssien ja molekyylien välillä. Julkaisussa II saamme näytteen laseroimaan sekä hilan kirkkaassa että pimeässä resonanssimuodossa. Julkaisussa III tutkimme laseroinnin dynamiikkaa ja saavutamme yli 100 GHz modulaationopeuden, jolla kehittämämme hilalaser säteilee pulssin, sen jälkeen kun se on viritetty. Hyödynnämme dynamiikan tutkimuksessa spektroskopiatekniikkaa, jossa systeemi viritetään kahdella perättäisellä laserpulssilla, joiden erotusta ajassa voidaan säätää.

Julkaisussa IV demonstroimme ensimmäistä kertaa maailmassa Bosen-Einsteinin kondensaation plasmonisessa systeemissä, ja se esiintyy huoneenlämpötilassa. Pystymme mittaamaan luminesenssispektrin evoluution paikan funktiona, jossa näemme näytteessä virittyvien kvasipartikkelien termalisoitumisen sekä makroskooppisen populaation muodostumisen alimmalle energiatilalle. Kvasipartikkelit ovat osittain valoa ja osittain elektronien värähtelyä nanopartikkeleissa. Termalisoitumisen eli Bosen-Einsteinin statistiikan mukaisen termisen tasapainotilan saavuttamisen tekee mahdolliseksi edestakainen emissio-absorptiosykli väriainemolekyyleissä.

Julkaisussa V saavutamme Bosen-Einsteinin kondensaatin vahvan kytkennän alueella. Tämä kondensaatti säteilee satatuhatta kertaa kirkkaampana kuin ensimmäinen kondensaatti. Mittausten perusteella termalisaatio tapahtuu ultranopeasti 200 fs aikaskaalassa, mikä selittää sen, että Bosen-Einsteinin statistiikan mukainen tasapainojakauma näkyy aikaintegroidussa signaalissa. Tämä siitäkin huolimatta, että ilman väriaineen vahvistavaa vaikutusta kvasipartikkelit hajoavat ja vuotavat valona näytteeltä ulos jopa alle 100 fs ajassa. Toiminta huoneenlämpötilassa, kondensaatin kirkkaus sekä näytteen kestävyys luovat erinomaisen alustan säteilevien kvasipartikkelikondensaattien, kvanttidynamiikan sekä topologisen fotoniikan tutkimukselle.

Avainsanat plasmoniikka, vahva kytkentä, nanohilalaser, Bosen-Einsteinin kondensaatio

ISBN (painettu) 978-952-60-8860-0 **ISBN (pdf)** 978-952-60-8861-7

ISSN (painettu) 1799-4934 **ISSN (pdf)** 1799-4942

Julkaisupaikka Helsinki **Painopaikka** Helsinki **Vuosi** 2019

Sivumäärä 280 **urn** http://urn.fi/URN:ISBN:978-952-60-8861-7

Preface

In this book, I will talk a lot about plasmons. But what are those tiny little buddies? Before going into details, I would like to thank the people who have helped me in this long journey of studying, up to the point of completing a doctoral degree.

First of all, the research of this doctoral dissertation was carried out in the Quantum Dynamics research group in the Department of Applied Physics at Aalto University School of Science, and in Micronova Nanofabrication Centre. I thank my supervisor and advisor Prof. Päivi Törmä for providing me the opportunity to work in her group. Time flies and it feels crazy to think about that little boy on the first day I started working for Päivi in the summer 2010. I am incredibly grateful for her support during over nine years I have known her. I appreciate her deep knowledge in physics, vision and leadership, and also the flexibility in times like the final spurt of completing a dissertation. Secondly, I would like to thank the pre-examiners Prof. Jan Klaers (University of Twente) and Prof. Humeyra Caglayan (Tampere University) for their very positive evaluation of the dissertation.

I want to thank Prof. Tommi Hakala for the discussions and guidance, and sharing his extraordinary intuition in physics questions. Special thanks to Dr. Robert Moreland who guided me as an undergraduate student and has taught me so many things in physics, science, and life in general. I thank Antti Moilanen for extremely fruitful collaboration, especially with the latest and greatest work on Bose-Einstein condensation. I thank Dr. Heikki Rekola for his help, and fun times, inside and outside the lab. I thank Dr. Konstantinos Daskalakis, Dr. Rui Guo, Dr. Jani-Petri Martikainen, Dr. Antti-Pekka Eskelinen, Marek Nečada, Aleksi Julku, Prof. Dong-Hee Kim, Jani Taskinen and Rebecca Heilmann, for all the great collaborations. I also want to thank all other colleagues, over the years, in the Quantum Dynamics research group.

Next, I want to thank my dear physics student mates since the day one, Dr. Jyri Salpakari and Lauri Lehtola. I am grateful for the teamwork we had when getting through the first-year courses in Engineering Physics (and winning the Fuksipeijaiset). During that year I gained a lot of confidence in being able to learn difficult things. I thank Olli Hasu and other gentlemen in Artistikommuuni™, everybody within Polirytmi community, and all other friends who I have had a privilege to hang around with, experience, and do stuff not related to plasmonic nanoparticle arrays.

Above all, I want to thank my mom and dad for their invaluable support and pushing

me forward, towards high education. I thank my sisters and their families for being there. Special thanks to my parents in law for their endless support. I also want to acknowledge our dear dog Brutus for taking me out for those relaxing walks. Finally, thank you for all of your support and love, my beautiful wife, the woman of my life, Meeri. This is for you.

Otaniemessä, November 18, 2019,

Aaro I. Väkeväinen

Contents

List of Publications

This thesis consists of an overview and of the following publications which are referred to in the text by their Roman numerals.

I A. I. Väkeväinen, R. J. Moerland, H. T. Rekola, A.-P. Eskelinen, J.-P. Martikainen, D.-H. Kim, and P. Törmä. Plasmonic surface lattice resonances at the strong coupling regime. *Nano Letters*, 14 (4), pp. 1721–1727 (2014), April 2014.

II T. K. Hakala, H. T. Rekola, A. I. Väkeväinen, J.-P. Martikainen, M. Nečada, A. J. Moilanen, and P. Törmä. Lasing in dark and bright modes of a finite-sized plasmonic lattice. *Nature Communications*, 8, 13687 (2017), January 2017.

III K. S. Daskalakis, A. I. Väkeväinen, J.-P. Martikainen, T. K. Hakala, and P. Törmä. Ultrafast pulse generation in an organic nanoparticle-array laser. *Nano Letters*, 18 (4), pp. 2658–2665 (2018), March 2018.

IV T. K. Hakala, A. J. Moilanen, A. I. Väkeväinen, R. Guo, J.-P. Martikainen, K. S. Daskalakis, H. T. Rekola, A. Julku, and P. Törmä. Bose-Einstein Condensation in a Plasmonic Lattice. *Nature Physics*, 14, pp. 739–744 (2018), April 2018.

V A. I. Väkeväinen, A. J. Moilanen, M. Nečada, T. K. Hakala, K. S. Daskalakis, P. Törmä. Sub-picosecond thermalization dynamics in condensation of strongly coupled lattice plasmons. Submitted to *Science*, 44 pages. Submission date 18th May 2019.

Author's Contribution

Publication I: "Plasmonic surface lattice resonances at the strong coupling regime"

The author fabricated the samples and performed the experiments. He analysed the experimental data and discussed the results together with other authors. He participated in writing the manuscript.

Publication II: "Lasing in dark and bright modes of a finite-sized plasmonic lattice"

The author had a significant role in designing the experiment and analysing the data. He fabricated the samples. He participated in performing the experiments, discussion of the results, and writing the manuscript.

Publication III: "Ultrafast pulse generation in an organic nanoparticle-array laser"

The author did the rate-equation modelling of the lasing dynamics, and he had an important role in analysing and interpreting the experimental results. He also fabricated the samples and helped in the experiments. The author wrote the manuscript together with K. S. Daskalakis.

Publication IV: "Bose-Einstein Condensation in a Plasmonic Lattice"

The author contributed in designing the samples, he studied different emitters and found a suitable one for the experiment. He participated in analysing the data and writing the manuscript. He also performed the pump-probe experiment.

Publication V: "Sub-picosecond thermalization dynamics in condensation of strongly coupled lattice plasmons"

The author was driving the project on the experimental side. He fabricated the samples and conducted the experiments. He did the data analysis together with A. J. Moilanen. The author performed the rate-equation simulations, and he wrote the manuscript together with A. J. Moilanen and P. Törmä.

The author has also contributed to the following related publications that are not included in this dissertation:

- R. J. Moerland, H. T. Rekola, G. Sharma, A.-P. Eskelinen, A. I. Väkeväinen, and P. Törmä. Surface plasmon polariton-controlled tunable quantum-dot emission. *Applied Physics Letters*, vol. 100, no. 22, p. 221111, May 2012.

- R. Guo, S. Derom, A. I. Väkeväinen, R. J. A. van Dijk-Moes, P. Liljeroth, D. Vanmaekelbergh, and P. Törmä. Controlling quantum dot emission by plasmonic nanoarrays. *Optics Express*, vol. 23, no. 22, pp. 28206–28215, Nov. 2015.

- R. J. Moerland, T. K. Hakala, J.-P. Martikainen, H. T. Rekola, A. I. Väkeväinen, and P. Törmä. Strong Coupling Between Organic Molecules and Plasmonic Nanostructures, in *Quantum Plasmonics* (S. I. Bozhevolnyi, L. Martin-Moreno, and F. Garcia-Vidal, eds.). Springer Series in Solid-State Sciences, pp. 121–150, Cham: Springer International Publishing, 2017.

- W. Wang, M. Ramezani, A. I. Väkeväinen, P. Törmä, J. G. Rivas, and T. W. Odom. The rich photonic world of plasmonic nanoparticle arrays. *Materials Today*, vol. 21, no. 3, pp. 303–314, Apr. 2018.

- R. Guo, M. Nečada, T. K. Hakala, A. I. Väkeväinen, and P. Törmä. Lasing at K Points of a Honeycomb Plasmonic Lattice. *Physical Review Letters*, vol. 122, no. 1, p. 013901, Jan. 2019.

Abbreviations

BA Benzyl Alcohol

BEC Bose-Einstein Condensate / Condensation

CCD Charge-Coupled Device

CDA Coupled Dipole Approximation

DMSO Dimethyl Sulfoxide

DO Diffracted Order

EBL Electron Beam Lithography

FDTD Finite-Difference Time-Domain

FWHM Full Width at Half Maximum

LASER Light Amplification by Stimulated Emission of Radiation

LSPR Localized Surface Plasmon Resonance

NA Numerical Aperture

OPA Optical Parametric Amplifier

PMMA Poly(methyl methacrylate)

PVA Poly(vinyl alcohol)

R6G Rhodamine 6G

SEM Scanning Electron Microscope

SLR Surface Lattice Resonance

TE Transverse Electric

TM Transverse Magnetic

QY Quantum Yield

Symbols

β spontaneous emission coupling factor

θ angle

λ wavelength

λ_{B} de Broglie wavelength

σ_{ext} extinction cross section

τ lifetime / decay time

ω angular frequency

c speed of light

$\mathbf{e}$ polarization vector

E energy

f frequency

g degeneracy

$\mathbf{G}$ reciprocal lattice vector

h Planck constant

$\hbar$ reduced Planck constant

I intensity

$\mathbf{k}$ wave vector

k_{B} Boltzmann constant

m_{eff} effective mass

n_i population density / particle number in energy state i

n_{ph} photon population density / photon number

N_i population density / particle number in molecular state i

p lattice period

P pump fluence

P_{th} threshold pump fluence

Q quality factor of a resonance

t time

T absolute temperature

1. Introduction

Nano-optics studies the interaction of light with physical objects that have features on the nanometer scale – smaller than the diffraction limit of light [1]. Plasmonics is an active research field within nano-optics, which focuses on metallic nanostructures. In this dissertation, I have studied metal nanoparticle arrays combined with organic dye molecules, and the emphasis is on the generation of coherent light through lasing action and Bose-Einstein condensation. I will begin with an introduction where I briefly explain all the important terms in the title of the dissertation.

1.1 Plasmonics

Plasmonics studies the light-matter interaction in metallic nanostructures and surfaces [2–4], and how these structures can be utilized for concentrating, manipulating and guiding light below the diffraction limit [5–9].

A plasmon refers to a quantum of electron plasma oscillations in metal. In other words, a plasmon is a collective excitation or *a quasiparticle* that actually consist of multiple particles and their interactions. The concept is analogous to a "free electron" in metal whose motion can be determined by considering a particle in free space with a certain *effective mass* that is different to the physical mass of an electron. The effective mass takes into account interactions with all other electrons and nuclei which disturb the motion of an electron in a complex way. A plasmon typically refers to a plasma oscillation in bulk of metal whereas a *surface plasmon polariton* refers to a coupled photon and electron plasma oscillation on a metal surface. A surface plasmon polariton is a surface wave that bounds the electromagnetic field at the metal-dielectric interface [10, 11].

Surface plasmon polaritons can be excited also in metallic nanoparticles that act as optical antennas, analogously to the antennas for longer wavelengths (e.g. radio waves), by converting the propagating electromagnetic radiation to localized oscillation of the electromagnetic field [12–16]. Plasmonic nanoparticles greatly enhance the interaction between light and quantum emitters, such as atoms and molecules, by focusing the energy of optical fields into sub-wavelength spatial regions where the emitters can be placed. Drastically increased energy density in plasmonic hotspots can enhance weak

non-linear processes such as frequency conversion [17], Raman scattering [18, 19] and fluorescence of (low quantum yield) emitters [20, 21]. Plasmonic structures also enable achieving so-called strong coupling between the optical modes and emitters at room temperature [22], and hold promise for such applications as nanolasers.

A plasmonic resonance at an individual nanoparticle is called a single particle resonance or alternatively a localized-surface plasmon resonance (LSPR). The resonance frequency strongly depends on the size, shape and material of the nanoparticle, and also surrounding dielectric environment [23]. Silver is generally the best plasmonic material due to its low ohmic losses throughout the entire visible spectrum [24, 25]. However, in the near-infrared, it can be replaced with gold which provides almost as low losses [26] in addition to a major benefit of being resistant to oxidization. Gold nanostructures can survive in ambient condition for long times, contrary to silver structures that we have seen to degrade due to oxidation within a week.

When nanoparticles are arranged in a periodic lattice, radiative coupling of the particles gives rise to non-localized plasmonic resonances. These dispersive plasmonic modes are called *surface lattice resonances* (SLRs), and they can produce remarkably narrow spectral line shapes [27–35]. Coupling of counter-propagating SLR modes can open a photonic band gap in the dispersion creating zero group velocity at the band edges (standing waves). Therefore, an SLR mode can provide feedback for lasing action and an energy ground state for Bose-Einstein condensation, in plasmonic lattices.

1.2 Lasing action

Interaction between light quanta (photons) and matter was formulated for the first time by Albert Einstein in 1917 [36]. He identified *three processes* by which a photon can interact with a (two-level) atom: 1) absorption, 2) stimulated emission and 3) spontaneous emission. Laser refers to a light source that employs optical amplification, namely Light Amplification by Stimulated Emission of Radiation (LASER), to generate spatially and temporally coherent electromagnetic radiation. Spatial coherence of light enables a high degree of collimation and tight focusing, making the available intensity (power per unit area) huge. Temporal coherence allows continuous operation with a very narrow frequency spectrum (single color), or alternatively, making it possible to produce ultrashort laser pulses with a broadband spectrum [37, 38]. These coherence properties make laser light useful for numerous practical applications. Lasers are nowadays used in laser printers, barcode scanners, projectors, laser surgery, cutting and welding material, just to name a few. One of the most important applications of the laser is in optical telecommunication, where the lasers are used to transfer data through optical fibres over large distances, with the help of optical amplifiers. Optical telecommunication establishes the basis of the Internet in the current magnitude and speed [39].

Miniaturising the coherent light sources down to micro- and nanometer scale has been under intensive research during the past two decades [40–42]. Plasmonic lasers

have been realised in various geometries, and those will be reviewed in Section 2.1. The generation of coherent radiation by sub-wavelength structures is highly attractive for its potential in applications ranging from on-chip optical communication [43–46] to bioimaging [47]. In this dissertation, I study the generation of coherent light in a plasmonic lattice through lasing action, and for the first time, Bose-Einstein condensation.

1.3 Bose-Einstein condensation

Bose-Einstein condensation is a manifestation of Bose-Einstein statistics that describes the energy distribution of bosons, one of the two classes of particles our universe consist of, at thermodynamic equilibrium [48]. Bose-Einstein condensate (BEC) is a phase of matter where multiple microscopic particles can be described with a single wave-function, which in ordinary language means that many microscopic particles act in concert – like one large particle.

All particles in the universe can be divided in two particle classes, bosons and fermions, based on one of their internal quantum property – the spin [49]. Bosons are spin-integer particles that include all the known force-carrying particles in the standard model of elementary particles. An example of these force-carrying particles is the photon (for the electromagnetic force). Bosons include also many atoms and nuclei, the ones with an even mass number, as well as many quasiparticles, e.g., phonons and plasmons. Fermions are spin-half particles that include all quarks (that constitute protons and neutrons) and all leptons (e.g. electrons and neutrinos), as well as composite particles made of an odd number of these (such as protons, neutrons, and many nuclei and atoms) [50].

The fundamental difference between these two classes of particles is that they follow different quantum statistics. The quantum statistics describes the distribution of identical particles, with negligible mutual interactions, over a discrete set of available energy states of a system in thermodynamic equilibrium. Fermions obey the Pauli exclusion principle and follow Fermi-Dirac statistics which strictly prohibits two particles occupying the same quantum state simultaneously. In contrast, there is no such restriction for bosons that follow Bose-Einstein statistics. Bosons rather prefer to occupy a single state as manifested by laser light that consist of photons occupying a single energy state. Bose-Einstein statistics produces a macroscopic population (condensate) into the energy ground state when the upper energy states are occupied by the maximum allowed number at a certain fixed temperature, and particles added to the system cannot go anywhere else than into the ground state. This phenomenon is called the Bose-Einstein condensation, which can explain for instance, the helium-4 superfluidity [51, 52] and superconductivity of metals [53–55].

An overview on the experimental research of Bose-Einstein condensates is given in Section 2.2. Brief theoretical discussion on the Bose-Einstein statistics and condensation can be found in Section 3.4.

1.4 Strong coupling regime

If two physical entities (particles or fields) can exchange energy, they are said to be coupled. In quantum mechanics, such interaction between two or more entities can be classified to weak or strong, and the system is said to be either at the weak or strong coupling regime, respectively.

The Hamiltonian that describes the time evolution of the system can be separated into non-interacting part and an interaction part. If the interaction part is small compared to the non-interacting part, the interaction can be treated with perturbation theory to find an approximate solution to the problem [49], and the system is said to be at the weak coupling regime. If this approximation fails, that is the interaction part cannot be treated as a small perturbation, we say that the system is at the strong coupling regime. In this case, the system of two (or more) interacting entities cannot be described with the original eigenstates of the individual entities but the system forms new eigenstates that are shifted in energy and are hybrids of the original states. For example, if a photon is strongly coupled to an electronic transition of an atom, the hybridized eigenstates are partly photons and partly excited atoms (the hybrid quasiparticle is partially light and partially matter).

One can draw an analogy from a system of two coupled harmonic oscillators, e.g., two mass-spring oscillators coupled with a third spring. This classical picture is used in Section 3.5 to develop a coupled-modes model that describes the hybrid modes of a strongly coupled system. In this dissertation, we are interested in strong light-matter interaction in plasmonic structures, which is comprehensively reviewed with necessary theoretical details by Törmä and Barnes in [22]. A nice review of recent experiments of strong coupling in plasmonic and photonic nanostructures is also given in [56].

1.5 Dissertation scope and structure

The scope of this dissertation is experimental study of strong light-matter interaction, lasing, and Bose-Einstein condensation in plasmonic nanoparticle arrays overlaid with organic dye molecules. The dissertation is divided to six chapters. After the introduction, Chapter 2 provides an overview on plasmonic lasers and experimental study of BECs. Chapter 3 discusses the theoretical foundations and methods required in the analysis of the experimental results. Chapter 4 introduces the sample fabrication, experimental setup and important details of the experimental procedures. In Chapter 5, I present the results of Publications I-V, focusing on the experiments. Strong coupling of molecular excitation and the optical modes of a plasmonic lattice is studied in Publication I, lasing action in the lattice modes is studied in Publications II-III, and Bose-Einstein condensation in the plasmonic lattices, at the weak and strong coupling regimes, is studied in Publications IV-V. Finally, I draw conclusions and give recommendations for future directions of the research presented in the dissertation. The original journal articles of Publications I-IV and the manuscript of Publication V are available as an appendix.

2. Background

2.1 Plasmonic lasers

Optical amplification by stimulated emission was demonstrated first at the microwave regime in 1955. The device was named a maser (microwave amplification by stimulated emission of radiation) [57]. After a couple of years, the concept was theoretically proposed to work also in the infrared and optical frequencies [58] and the first laser was demonstrated in 1961, at wavelength of 694.3 nm using ruby as the gain material [59]. Since the first demonstration the lasers have developed enormously and have found numerous applications in different areas of science and everyday life. Nowadays compact solid-state diode laser span the entire visible spectrum and are available on stock. However, miniaturizing the laser sources even further is an intensive on-going research effort [40–42].

Plasmonic lasers can work as laser sources beyond the diffraction limit, and they also hold promise of ultrafast modulation speeds [60–62]. The first laser based on surface plasmons was demonstrated by Sirtori et al. in 1998 in the infrared [63]. In the beginning of 2000s, a spaser (surface-plasmon amplification by stimulated emission of radiation) was proposed by Bergman and Stockman [64], and the original idea was to amplify surface plasmons at a single nanoparticle resonator [65, 66]. Since the first proposal, spasers has been experimentally studied [47, 67–69] but a direct evidence of spasing action truly at a single nanoparticle level is yet to be shown [70].

Besides single nanoparticle resonators, there are various other interesting systems that utilize plasmonic modes for lasing action. Lasing (or spasing) of propagating surface-plasmon polaritons has been achieved by using block reflectors to form a cavity on an ultrasmooth silver surface [71] and by using nanohole arrays as cavity mirrors on a gold film [72]. One extensive class of plasmonic lasers is semiconductor nanostructures placed on metal surfaces. These devices cover a semiconductor nanowire [44, 73–79], nanodisk [80] and nanosquare [43, 81, 82] placed on top of a metal surface, and they span a wavelength range from the UV [76, 77] to the telecom wavelengths of 1.3 μm [79, 80]. Lasing has been demonstrated also in silver nanowires surrounded by gain medium [83, 84] as well as in metal-insulator-metal

plasmonic waveguides and metallic-coated nanocavities with optical [46, 85] and electrical [86–89] pumping. A great review of semiconductor plasmonic nanolasers is given in [90].

Distributed-feedback type plasmonic lasers have drawn a significant attention during the last five years and they have been demonstrated by several research groups. In this dissertation, I study metal nanoparticle arrays that can support lasing action in surface-lattice-resonance modes which are hybrid modes containing a photonic and a plasmonic part. In Publication II we demonstrate lasing action in both bright and dark modes of the plasmonic lattice in the visible wavelength. In Publication III the dynamics of the laser pulse generation is studied with a similar pump-probe spectroscopy technique that has been previously applied for dynamics study of semiconductor nanowire lasers [77, 78]. Besides the work presented here, lasing action has been obtained in two-dimensional square or rectangular lattice of metal nanoparticles, combined with organic dye molecules, also in [34, 91–100]. Moreover, lasing has been achieved in a honeycomb lattice of nanoparticles (K-point lasing [101]), one-dimensional nanoparticle chain [102], and in nanoparticle arrays made of magnetic materials [103]. Finally, lasing has been achieved also in two-dimensional semiconductor nanoparticle arrays [104] and metal nanohole arrays with semiconductor gain material [105–108] and with an organic laser dye [109].

2.2 Bose-Einstein condensates

Bose-Einstein condensation was originally predicted by Bose and Einstein in 1924 [110–112]. For a long time the only known example of a BEC, in a real system, was liquid helium-4 in its superfluid phase. The superfluidity of helium-4 was discovered in 1938 [113, 114] and associated to the condensation phenomenon of the Bose-Einstein statistics [115, 116] but it had remained under debate if it was truly a BEC, with macroscopic ground state population, as liquid helium is a strongly interacting system, far from an ideal BEC. It took until 1995 when the BEC was experimentally unambiguously demonstrated in a system that consisted of dilute gas of alkali atoms at ultralow temperatures of 100 nK – 2 μK [117–119].

After the first observations, the BEC research has expanded rapidly, and the BEC has been demonstrated in a variety of different systems. First, in the late 1990s, a BEC was achieved with spin-polarized atomic hydrogen [120, 121]. In 2000s, the BEC was demonstrated for quasiparticles such as magnetic spin-wave excitation in a ferro-, ferri- and antiferromagnets, so-called magnons [122–127], as well as strongly-coupled exciton-polaritons in inorganic semiconductor quantum wells placed inside a high-Q optical microcavity [128–132]. Later on, also magnons in a dense gas of spin-polarized atomic hydrogen were shown to condense [133], which is different from the BEC of atomic hydrogen (real particle) in [120, 121]. All of these works were still done at liquid helium temperatures but in 2006 the BEC was obtained at room temperature for magnons [134], and in 2008 for exciton-polaritons [135]. The observations of room-temperature condensates were continued with BECs of

exciton-polaritons in organic semiconductor microcavities [136–145], and with a BEC of photons in a dye-filled high-Q microcavity, shown by Klaers et al. in 2010 [146]. Strikingly, also superfluidity was demonstrated for exciton-polariton condensates at cryogenic [147–150] and even at room [151] temperature.

Observation of the photon BEC triggered a vivid research effort on condensation of light, which is closely related to the condensation of exciton-polaritons or polariton lasing in optical microcavities. The photon BEC has been studied experimentally in a dye-filled microcavity [152–165] and in an optical fiber cavity [166, 167]. Similarities and differences of laser operation and Bose-Einstein condensation are discussed in [132, 168].

In Publication IV-V, we introduce a new member to the expanding family of room-temperature BECs, namely a BEC of excitations in a plasmonic lattice. Our condensate, as also many other condensates introduced above, is not a text-book type BEC of non-interacting particles in thermal equilibrium but the system is rather in non- or quasi-equilibrium. It means that the particle number does not stay constant during the condensation process due to decay of quasiparticles that form the condensate. Non- and quasi-equilibrium condensates have recently attracted growing attention due to their possibilities in studies of non-equilibrium quantum dynamics. Theoretical studies of photon BECs and driven-dissipative or non-equilibrium condensates can be found in [169–174] and for example in [175–183], respectively.

3. Theoretical foundation

This chapter introduces the theoretical foundation and the theoretical methods applied in this dissertation. In Section 3.1, I start with introducing the concept of a resonance and a mode in physical systems. In Section 3.2, I discuss the optical modes in a plasmonic lattice, particularly the surface lattice resonances (SLRs), the origin of which is described in detail. In Section 3.3, I continue with a discussion of laser theory and a rate-equation model for a four-level gain medium with pulsed excitation. In Section 3.4, I explain some basics of Bose-Einstein statistics and condensation, and finally in Section 3.5, I introduce the coupled-modes model that is used to describe strongly-coupled systems.

3.1 Resonances in physical systems

Let us start by specifying the meaning of a mode and a resonance in physical systems. A mode or a *normal mode* refers to a pattern of motion in an oscillating system in which all parts of the system move sinusoidally, with the same frequency and a fixed phase relation [184]. The motion of the system is often a superposition of multiple normal modes that are in mathematical terms orthogonal to each other, meaning that they can be excited independently, without excitation of any other mode. Each normal mode describes a free motion of the system with a certain resonant frequency constituting a set of *natural frequencies* with which the systems likes to oscillate. An easy example of a mode in a dynamical mechanical system is a guitar string, in which the string is the medium, stress applied by the player is the excitation, the displacement of the string with respect to its static state is the modal variable. The lowest resonant frequency is called the fundamental frequency and the higher resonant frequencies are called higher harmonics or overtones. The mode concept can be generalized also to optics and quantum mechanics. For example, in optics an accelerating charged particle is the excitation, the electromagnetic field is the modal variable, and the medium can be just the free space. In quantum mechanics, a normal mode corresponds to an energy eigenstate of the system, or in other words, it can be considered as a quantum state that corresponds to a certain energy.

A resonance refers to a condition that a driving force is periodically applied to the

system at one of its natural frequencies. Due to damping forces, resonances are not delta peaks in the frequency spectrum but have certain widths. A resonance can be characterized by the frequency dependent response of the amplitude of the modal variable. At resonance, the system stores the minimum amount of energy for a given oscillation amplitude. Or equivalently, for a given stored amount of energy or for a given driving force, the oscillation amplitude is the largest exactly at the resonant frequency. One important measure of a resonance is its quality factor, or Q factor, that is defined as

$$Q = \frac{f_0}{\Delta f_0} \tag{3.1}$$

where f_0 is the resonant frequency and Δf_0 is the spectral linewidth. The linewidth is proportional to the damping rate of the stored energy, and the quality factor describes how many oscillations occur before the energy stored in the system is lost and the oscillation dies out. The quality factor is therefore proportional to the lifetime of the mode, that is an essential parameter generally in physics, and also in the study of this dissertation. The lifetime is inversely proportional to the spectral linewidth,

$$\tau = \frac{Q}{2\pi f_0} = \frac{1}{\Delta\omega_0}, \tag{3.2}$$

where ω_0 refers to an angular frequency, $\omega = 2\pi f$.

Next, we are going to focus on modes and resonance in optical systems. An optical mode is a spatial pattern of oscillating electromagnetic field that is supported by the structure (boundary conditions of the system). In free space, there is a continuum of optical modes but confinement of the optical field in a cavity restricts the number of available modes to a discrete set of normal modes that fulfil the boundary conditions [37,38]. In a simple optical cavity formed by two mirrors (or a three-dimensional box), the possible modes are waves with an integer multiple of half the wavelength matching the distance of the mirrors (or walls). As each mode has a certain resonant frequency or *resonance frequency*, the term *mode* and the term *resonance* are often used interchangeably.

3.2 Surface lattice resonances in plasmonic lattices

Let us consider plasmonic nanoparticles that are arranged in a regular periodic lattice. This system composes a so-called *plasmonic lattice* that supports two different types of plasmonic resonances. First, the individual nanoparticles have resonances that occur when an electromagnetic field induces resonant oscillation of free electrons (electron plasma) in the metal. The single particle resonances are called localized surface plasmon resonances (LSPRs) and their resonant frequency strongly depends on the particle size and shape. Typically these resonances occur at optical frequencies, and thus the nanoparticles can be considered as optical antennas, as discussed in Section 1.1. Besides the single particle resonance, collective resonances arise due to a radiative coupling of individual nanoparticles in the lattice. These non-localized

modes are called surface lattice resonances (SLRs) and they can be considered as hybrid modes comprised by the LSPR and diffracted order (DO) modes of the periodic structure. The SLRs are of interest because of their long lifetimes, due to a much larger photonic part of the mode compared to the LSPR alone. The LSPR has a Q factor of the order 10 but for the SLR it can easily reach a value of more than 100; values beyond 300 have been experimentally obtained [185]. In the work presented in this dissertation, the SLRs have a Q factor between 100 and 250. The SLR linewidth strongly depends on the spectral distance between the LSPR and the DO, and the spectral position of the DO depend on the lattice periodicity and the incident angle (in-plane **k** vector).

The electromagnetic field of the SLR mode is bound to the plane of the lattice and the LSPR provides plasmonic enhancement in the hot-spots close to each nanoparticle. Dispersion of the SLR closely follows the DOs of the lattice, except at the crossing points with the LSPR. We can calculate the spectral position of the DOs in a so-called empty lattice approximation [186], where we consider optical plane waves travelling in a two-dimensional plane with an infinitesimally small periodic refractive index modulation. Here we focus on the SLR modes in square and rectangular nanoparticle lattices. However, by calculating the DOs and taking into account the polarization of the nanoparticle (dipole orientation), the dispersion of the SLR modes can be obtained also for more complicated lattice geometries. A pragmatic study of the SLR modes in square, rectangular, hexagonal, honeycomb and Lieb lattices can be found in [187].

Let us start with the dispersion relation of light in free space:

$$E = \frac{\hbar c k}{n} = \frac{\hbar c}{n}\sqrt{k_x^2 + k_y^2 + k_z^2}, \tag{3.3}$$

where E is the photon energy, $\hbar = h/2\pi$ the reduced Planck constant, c the speed of light, and n the refractive index. The wave number, k, is the absolute value of the wave vector, **k**, that has components in the Cartesian coordinate system (x, y, z). If we restrict ourselves to the waves propagating in the (x, y) plane, then $k_z = 0$, and the dispersion relation defines a conical surface in the three-dimensional space of (k_x, k_y, E), see Figure 3.1a. Inside this so-called light cone, the plane waves can propagate in free space, but outside the cone, at least one of the wave numbers must become imaginary to fulfil the dispersion relation in Equation 3.3.

We assume an infinite two-dimensional periodic lattice with periodicities of p_x and p_y, in the x and y direction, respectively. The propagating light waves in the (x, y) plane, shifted by the reciprocal lattice vectors $\mathbf{G}_x = \pm 2\pi/p_x\hat{x}$ or $\mathbf{G}_y = \pm 2\pi/p_y\hat{y}$, do all have the same energies, given by the Bloch's theorem [188]. This results in repeated light cones in the reciprocal (or momentum) space, shifted by the momentum kick given by the lattice ($\mathbf{G}_x$ and / or $\mathbf{G}_y$). Figure 3.1b illustrates the light cones of the first DOs (0,-1) and (0,+1), given by the momentum kick of $\mathbf{G}_y$ in $-y$ and $+y$ direction. The black lines depict the cross sections of the conical surfaces along k_x and k_y, representing the dispersion of the mode in these two principal directions. In Figure 3.1c, the first DOs in $-x$ and $+x$ direction, (-1,0) and (+1,0), are added to the picture. As the lattice here is rotationally symmetric ($p_x = p_y$), one can observe equal cross sections along both k_x and k_y, see Figure 3.1d.

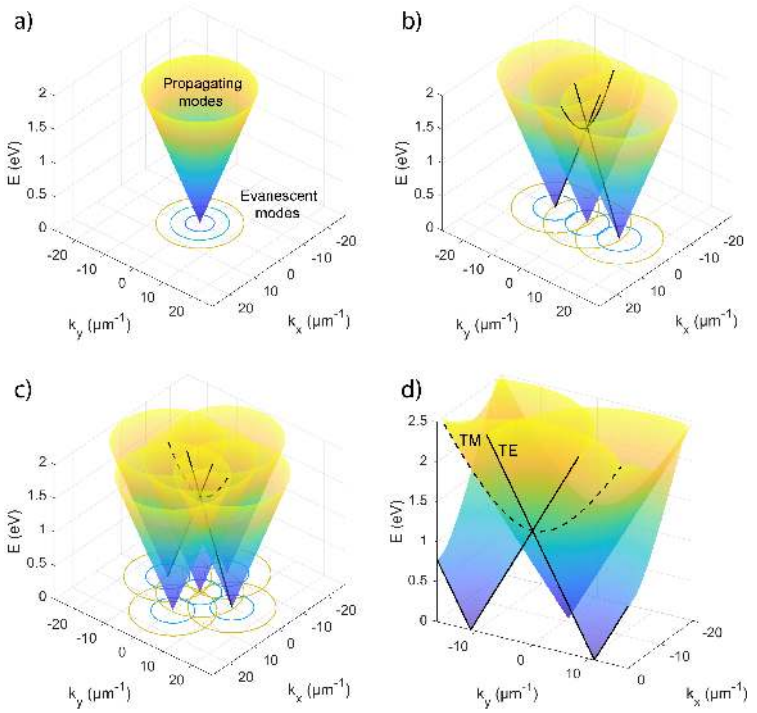

Figure 3.1. Light cones in a diffractive periodic lattice given by the empty lattice approximation [186]. (a) Conical surface formed by the dispersion of propagating plane waves along (x, y) plane. (b) First DOs in y direction (0,±1), for x polarized particles ($\mathbf{e}_x$). Black lines indicate the cross sections along k_x and k_y. (c) First DOs in both x direction (±1,0) and y direction (0,±1) of a two-dimensional square lattice ($p_x = p_y$). Solid lines denote the TE mode ($\mathbf{e}_x$,k_y) arising from DOs (0,±1), the dashed line denotes the TM mode ($\mathbf{e}_y$,k_y) arising from DOs (±1,0). (d) shows an illustrative crosscut of (c).

Let us now move on from the empty lattice approximation to the lattice of nanoparticles. The LSPR modifies the dispersion but far from the LSPR frequency the SLRs closely follow the DOs of the lattice. Near the LSPR, the two modes undergo an avoided crossing that can be identified as strong coupling, see Publication I. The LSPR in each nanoparticle can be approximated as a point dipole that radiates predominantly to the perpendicular direction with respect to its polarization. Therefore, the DOs in y direction correspond to x-polarized ($\mathbf{e}_x$) particles, and vice versa. In other words, momentum kick $\mathbf{G}_y$ is only available for the modes supported by x-polarized particles. The solid lines in Figure 3.1b are given by

$$E = \frac{\hbar c}{n}\sqrt{(k_x \pm G_x)^2 + (k_y \pm G_y)^2}, \tag{3.4}$$

by setting $G_y = 0$, and $k_y = 0$ or $k_x = 0$. The refractive index used here is $n = 1.52$, corresponding to borosilicate glass substrates. Note that Equation 3.4 is symmetric with respect to x and y for a square lattice but the diffracted orders can be separated in energy by making the periodicity asymmetric ($p_x \neq p_y$). We classify the SLR modes to transverse magnetic (TM) or transverse electric (TE) depending on the polarization

and the propagation direction. For the TE modes, the polarization is perpendicular to the propagation direction ($\mathbf{e}_x, k_y$ or $\mathbf{e}_y, k_x$), and for the TM modes they are parallel ($\mathbf{e}_x, k_x$ or $\mathbf{e}_y, k_y$). The TE modes are linear lines intersecting at the Γ-point ($k_x, k_y = 0$) in contrast to TM modes that are parabolic at small k values, see Figure 3.1d.

The crossing points of the light cones are essential because those are the points the SLR modes, propagating in different directions, can couple. At the Γ-point, two counter-propagating waves can couple with the second-order Bragg scattering ($2\mathbf{G}_{x,y}$) whereas the first-order scattering ($\mathbf{G}_{x,y}$) couples the wave in or out from the lattice at an angle perpendicular to the lattice plane. The two counter-propagating waves form a standing wave that has either the anti-node or the node at each nanoparticle location. The position of the standing wave is determined by a phase-matching requirement of forward and backward propagating Bragg scattered waves as explained with a simple quarter-wave dielectric stack in [189,190]. Coupling of the counter-propagating modes opens a photonic band gap at the Γ-point where the single mode splits into two [33]. The two modes arising from coupling shift in energy, one downward and one upward.

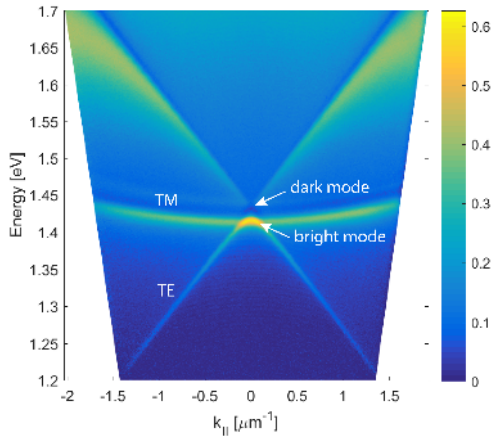

Figure 3.2. Measured extinction spectrum (1 – Transmission) that reveals the SLR dispersion of an array of cylindrical nanoparticles with the lattice period $p_x = p_y = 570$ nm (square lattice). The orientation of the spectrometer slit defines the direction of the in-plane **k** vector, k_{II}, along which the dispersion is measured. The figure clearly shows both TE and TM modes and a bandgap opening at the Γ-point ($k_{||} = 0$). Here, the lower branch is the *bright* and the upper one is *dark* (indicated with arrows). At high energies one can observe bending of the TE mode due to the LSPR, the energy of which is outside the measured range.

Figure 3.2 shows an experimentally measured angle-resolved extinction spectrum of a plasmonic lattice. It is basically a cross section along either k_x or k_y of the dispersion surfaces introduced in Figure 3.1. The extinction spectrum reveals the dispersion of the SLR mode. A clear band gap opening can be observed at the Γ-point, and interestingly, there is only one mode (lower branch) visible. The lower branch is called a *bright mode* and it corresponds to dipolar excitation in the nanoparticles (anti-node at each particle), thus enabling the coupling to the far-field radiation. In contrast, the upper branch is not visible in the extinction spectrum and it is therefore called a *dark mode*. It corresponds a quadrupolar excitation in the nanoparticles

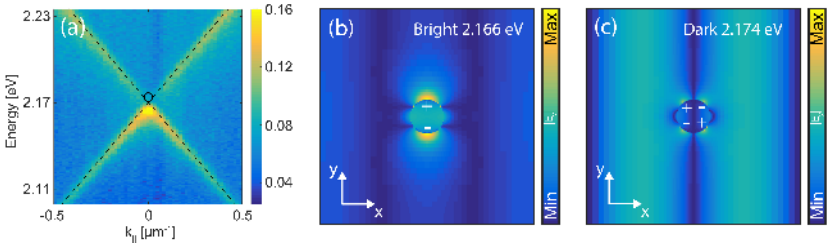

Figure 3.3. (a) Measured extinction spectrum of a typical sample, revealing the SLR dispersion. First diffracted orders are depicted with dashed lines and the location of the dark mode is indicated by the black circle. (b-c) Charge and field distributions (electric field amplitude $|\mathbf{E}_y|$) of the bright and dark modes for an infinite lattice, obtained from FDTD simulations with periodic boundary conditions. Here, the particles are excited by dipole sources with random orientation, location and phase, in the beginning of simulation. The details can be found in Methods of Publication II. The observed modes correspond to an array of nanoparticles mainly polarized along y direction and thus radiating predominantly along $-x$ and $+x$ direction. Two counter-propagating radiation fields result to a standing wave which has either an anti-node or a node at each particle location, corresponding to the bright or dark mode, respectively. The bright mode exhibits a dipolar and the dark mode a quadrupolar charge distribution. Figure adapted with permission from Publication II (© CC BY 4.0).

(node at each particle) and thus cannot couple to the far-field, due to zero net dipole moment. However, this is exactly true only for an infinite lattice as is shown in the lasing experiments in Publication II. Figure 3.3 further explicates the formation of the dark and bright modes, including the charge distribution in the nanoparticles for both modes. The dark mode is essentially the same as a *bound state in continuum*, a term sometimes used for subradiant modes, see for example in [104].

When the DO is relatively far from the LSPR, the formation of the SLR mode can be analytically described by Fano theory [191–195]. It explains the asymmetric line shape of a resonance with interference effects in the coupled system that has a narrow (high-Q) resonance and a broad (low-Q) resonance. In the case of a plasmonic lattice, the high-Q resonance is the purely photonic DO mode, and the low-Q resonance is obviously the LSPR. In addition, the shape and dispersion of the SLRs can be accurately calculated with a coupled-dipole approximation (CDA) model described in [27, 28, 186, 196]. In Publication I, we have analysed the SLR modes with both the Fano theory and CDA but as they are not in the scope of this dissertation, I do not discuss them here in further detail.

A two-dimensional dispersion surface of the SLR mode can be measured by taking cross sections of (k_x, k_y, E) along different k-directions. In the transmission experiment, this is done by rotating the sample (lattice) with respect to the spectrometer slit. Then, the extinction maxima found in each cross section are combined to a one 3D plot. An example of the dispersion surface is shown in Figure 3.4a, measured for an array of cylindrical gold nanoparticles with a diameter of 100 nm, a height of 50 nm, and lattice periods of $p_y = 570$ and $p_x = 620$ nm. This is the sample used in Publication V for BEC experiments. Figure 3.4b displays examples of the measured cross sections as a function of the angle between the y axis of the lattice and the spectrometer slit.

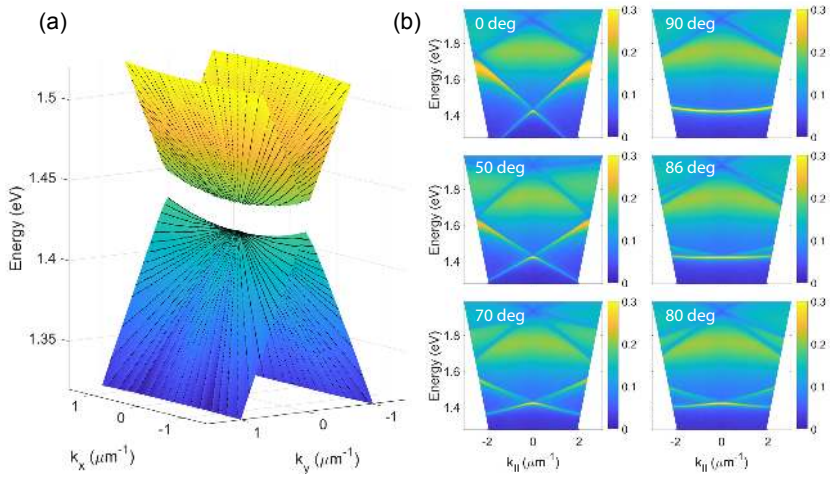

Figure 3.4. (a) A measured dispersion surface where the black dots indicate the extinction maxima. (b) Examples of the measured extinction spectra that are cross sections of the 2D dispersion along the in-plane k-vectors determined by the spectrometer slit when rotating the sample. The angle values denoted in the figure refer to the angle between k_y and the k-vector determined by the slit.

3.3 Laser theory

In this section, I develop the laser rate-equation model used in Publications III and V.

3.3.1 Stimulated emission

Lasing action is based on stimulated emission of photons that provides optical gain in the system (see Fig. 3.5). Stimulated emission unleashes the energy of excited atoms (or molecules / other quantum emitters) by emission of photons into the lasing mode, which has a well-defined frequency and phase determined by the cavity geometry. Accumulation of stimulated photons results in temporally and spatially coherent laser light.

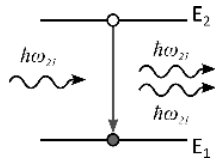

Figure 3.5. Schematic of light-matter interaction via stimulated emission of a photon. The photon energy is $\hbar\omega_{21} = E_2 - E_1$. In a laser system, energy level E_2 corresponds to the upper laser level and E_1 to the lower laser level, respectively.

In general, lasing action requires population inversion between the two energy levels between which the stimulated emission occurs. That is because stimulated

emission competes with the absorption of photons. Moreover, the optical gain needs to overcome the total loss of the system. The total loss is often called the *cavity loss*. The available optical gain depends on the inversion density as

$$N^* = N_2 - \frac{g_2}{g_1} N_1, \tag{3.5}$$

where N_2 and N_1 are the population densities, and g_2 and g_1 are the degeneracies, of the upper and lower laser levels, respectively. The requirement of amplification, that is the optical gain overcoming the system losses, leads to a threshold value for the inversion density, N^*_{th}.

3.3.2 Four-level gain medium

An organic dye molecule can be modelled as a four-level system when used as a laser gain medium. The four-level model is based on Franck-Condon principle and the resulting Stokes shift in absorption and emission process of the molecule, see Figure 3.6. First, let us consider a molecule that is in its ground state. We can define the highest occupied molecular orbital (HOMO) to be the electronic ground state, S_0, and the lowest unoccupied molecular orbital (LUMO) to be the electronic excited state, S_1. As the molecule interacts with light, an electron can undergo transition between these two states. Moreover, the molecule has vibrational and rotational degrees of freedom that produce a tightly-spaced fine-structure of states for each electronic state. This fine-structure is called the *ro-vibrational manifold*. The Franck-Condon principle says that the electronic transitions are very fast compared to the time it takes for nuclei to move and re-configure themselves to a new equilibrium state. This is because nuclear masses are much larger than the mass of an electron, which yields a much larger inertia. Thus, a transition between vibrational states owning similar nuclear coordinates is more probable than other transitions, and the electronic transitions can be drawn as a straight vertical line in the energy diagram (see Fig. 3.6). In other words, the electronic transition is most probable between ro-vibrational states that have the highest spatial overlap of their wave functions.

Now again, let us consider a molecule in its ground state. The molecule interacts with electromagnetic radiation. It absorbs a photon that excites an electron from the lowest ro-vibrational state of S_0 to some higher ro-vibrational state of S_1. Absorption is most probable to a state that has the highest spatial overlap of the wave-function with the initial state. Then, the electron undergoes vibrational relaxation process and moves down to the lowest ro-vibrational state of S_1. The excitation can decay to S_0 either non-radiatively or radiatively. Radiative decay occurs by emission of a photon with an energy that corresponds to the transition, that again takes place between states with the highest wave-function overlap. The difference in absorption and emission energies, namely the energy lost in the process, is called the Stokes shift. It is important to keep in mind that the picture in Figure 3.6 describes a single molecule. There are effects, such as different microscopic dielectric environment, which can move the respective location of S_0 and S_1, leading to inhomogeneous broadening of absorption and emission spectra.

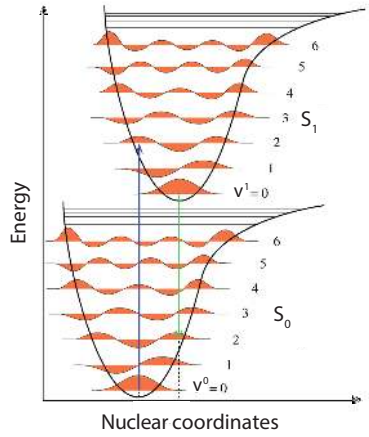

Figure 3.6. Energy diagram of two electronic states $S_{1,2}$ dressed with ro-vibrational states $v^{1,2} = 0, 1, 2, ...$ The diagram illustrates the Franck–Condon principle. The wave functions of the ro-vibrational states are sketched with orange color. Electronic transitions are most probable between ro-vibrational states that have high wave-function overlap. This corresponds to a minimal change in the nuclear coordinates. Electronic excitation (absorption) is depicted with a blue arrow, and emission of a photon (fluorescence) with a green arrow. Figure is modified from one in [197].

An energy diagram of the four-level model for laser gain medium is presented in Figure 3.7. It is a simplified model of a molecule where the absorption transition is assumed to occur from the lowest ro-vibrational state of S_0 (level 0) to some higher ro-vibrational state of S_1 (level 3), then the electron looses energy via vibrational relaxations and ends up to the lowest ro-vibrational state of S_1 (level 2, upper laser level). The emission occurs from that state to a higher ro-vibrational state of S_0 (level 1, lower laser level) and the electron again relaxes to the ground state of the system.

3.3.3 Rate-equation model

In this dissertation, I study lasing dynamics with a four-level rate-equation model. I perform the simulations with realistic (or measured) decay times of the molecule, and the cavity lifetime based on measured SLR line widths. Therefore, the simulations provide somewhat quantitative results with respect to the lasing dynamics, which can be compared to the experiments. With respect to the pump fluence and output energy, the simulations provide only qualitative results. The total number of molecules is chosen arbitrarily by only requiring that the gain does not yet saturate near the threshold pump fluence. Based on the experiments, the absorbed energy and the number of active dye molecules is very difficult to estimate because the volume of the lasing mode is hard to define. Einstein formulated [36] that the rate of absorption depends on the atomic population density in the lower energy level, the spectral energy density of radiation, $\rho(\omega_{21})$, and the Einstein coefficient B_{12}. Respectively, the rate of stimulated emission depends on the population density in the upper level,

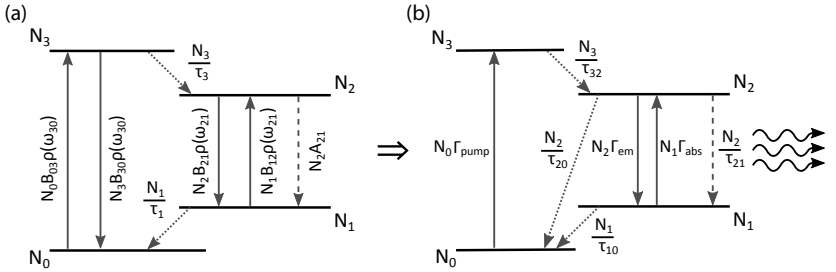

Figure 3.7. Energy level diagram of the four-level model. Left: four-level energy diagram with the transition rates defined by the spectral energy density of radiation at the transition energies, $\rho(\omega_{30})$ and $\rho(\omega_{21})$, and by the Einstein coefficients, B_{03}, B_{30}, B_{12}, B_{21}, and A_21 [198]. The rates depend also on the population density at the corresponding levels. Here, N_i is the population density and τ_i is the lifetime of each level i. Right: Simplified model where, instead of population density, N_i describes a population number normalized to the total number of emitters. The pump rate is denoted by Γ_{pump}, and absorption and stimulated emission rates between the levels 2 – 1 with Γ_{abs} and Γ_{em}, respectively. The Einstein coefficient $A_{21} = \frac{1}{\tau_{21}}$ by definition, the other rates are defined along with the rate equations in the text. Here, we have discarded the absorption term between levels 0 – 3, not being relevant for the lasing dynamics after a pulsed excitation. On the other hand, we have added a non-radiative decay path from level 2 to 0, as it is significant for most dye molecules.

the spectral energy density, $\rho(\omega_{21})$, and the Einstein coefficient B_{21}. In contrast, the rate of spontaneous emission depends only on the upper level population density, and the Einstein coefficient A_{21}, and not on the radiation field [37,38]. The Einstein coefficients are defined as [198]

$$A_{21} = 1/\tau_{21} \tag{3.6}$$

$$B_{21} = \frac{\pi^2 c^3}{\hbar \omega_{21}^3} A_{21} \tag{3.7}$$

$$B_{12} = \frac{g_2}{g_1} B_{21}, \tag{3.8}$$

where τ_{21} is a spontaneous emission lifetime, that is a material dependent parameter, and $\hbar\omega_{21}$ is the separation of the energy levels. The equality in Equation 3.8 follows from Planck's law for spectral density of black body radiation in thermal equilibrium [38].

Einstein's definition for transition rates is used in the energy-level diagram in Figure 3.7a. Here, I have included the absorption and stimulated emission rates between the levels 0 – 3 and 1 – 2, as well as the spontaneous emission between the levels 1 – 2. Between the levels 3 – 2 and 1 – 0 there are rates for the vibrational relaxation. A slightly simplified energy-level diagram is depicted in Figure 3.7b, where I have discarded the absorption term between the levels 0 – 3 and added a non-radiative decay path from the level 2 to 0. The former modification can be justified because we are interested in the time evolution after the system is excited with a pump pulse, with a given number of excited emitters on level 3. Pump rate $\Gamma_{\mathrm{pump}} = r$ is the rate of absorbed energy from an external pump. Additionally, the degeneracies of the laser levels are assumed to be equal ($g_1 = g_2$) so the absorption and stimulated

emission terms are equal as well. Based on a linear gain model [199, 200] we can write

$$N_2\Gamma_{\text{em}} - N_1\Gamma_{\text{abs}} = \frac{\beta n_{ph}}{\tau_2}(N_2 - N_1) = \frac{\beta n_{ph}}{\tau_2}N^*, \tag{3.9}$$

where both the Γ_{em} and Γ_{abs} are expressed with the spontaneous emission coupling factor β, photon number in the lasing mode n_{ph}, and the radiative decay time τ_{21}.

Finally, we can formulate the four-level rate equation model that describes population of each energy level as a function of time, taking into account rates between the levels. This model can be used to calculate lasing dynamics when the system is excited with an external energy source (pump). The model consists of the following coupled equations:

$$\frac{dn_{ph}}{dt} = \beta n_{ph}\frac{(N_2 - N_1)}{\tau_{21}} + \beta\frac{N_2}{\tau_{21}} - \frac{n_{ph}}{\tau_{cav}} \tag{3.10}$$

$$\frac{dN_0}{dt} = -rN_0 + \frac{N_2}{\tau_{20}} + \frac{N_1}{\tau_{10}} \tag{3.11}$$

$$\frac{dN_3}{dt} = rN_0 - \frac{N_3}{\tau_{32}} \tag{3.12}$$

$$\frac{dN_2}{dt} = -\beta n_{ph}\frac{(N_2 - N_1)}{\tau_{21}} - \frac{N_2}{\tau_{21}} - \frac{N_2}{\tau_{20}} + \frac{N_3}{\tau_{32}} \tag{3.13}$$

$$\frac{dN_1}{dt} = \beta n_{ph}\frac{(N_2 - N_1)}{\tau_{21}} + \frac{N_2}{\tau_{21}} - \frac{N_1}{\tau_{10}}, \tag{3.14}$$

where the population of each level is denoted with N_i and decay times with τ_i. The β factor gives the fraction of spontaneously emitted photons to the lasing mode compared to the total number of spontaneous photons, τ_{cav} is the cavity lifetime.

The threshold value for population inversion can be defined by comparing the gain and loss terms for the photon number n_{ph} in Equation 3.10. The optical gain must overcome the loss, and at the threshold they are equal

$$\beta n_{ph}\frac{(N_2 - N_1)}{\tau_{21}} = \frac{n_{ph}}{\tau_{cav}}, \tag{3.15}$$

So the threshold value becomes

$$N^*_{th} = \frac{\tau_{21}}{\beta\tau_{cav}}. \tag{3.16}$$

3.3.4 Gain-switching

In the experiments, we pump our plasmonic lattice lasers with external laser pulses with a duration of the order 100 fs. The excitation pulses are very short compared to the fluorescence lifetime (spontaneous decay) of the dye molecule, that is of the order hundreds of picoseconds. Therefore, the plasmonic lattice laser can be considered as a gain-switched laser that exhibits dynamics similar to Q-switched lasers [37, 38]. Figure 3.8 shows typical time evolution of a gain-switched laser, obtained with the rate-equation model presented above. In gain switching the built-up of population inversion is very rapid compared to the upper laser level lifetime. Therefore, the population inversion can built up to values much higher than that of the threshold before stimulated emission is triggered and begins to deplete the population. Similarly to Q-switched lasers, the population inversion N^* is burned down to much lower than the threshold value and an output pulse is generated. The output pulse peaks when the dropping N^* equals the threshold value $N^* = N^*_{th}$.

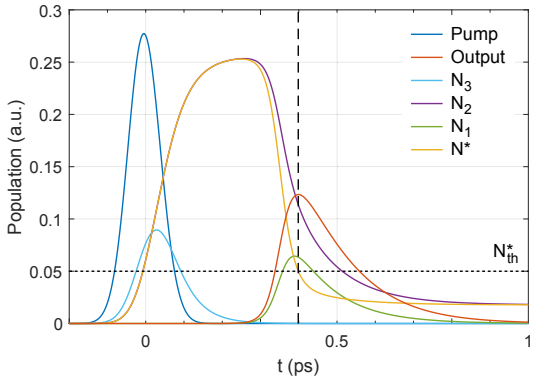

Figure 3.8. Rate-equation simulation with the four-level gain medium. The system is excited with a 100 fs pump pulse that lifts the population inversion to a value much higher than the threshold (dotted line). When the lasing is triggered the population inversion is burned to a value much below the threshold. The dashed vertical line marks the peak of the output pulse which occurs exactly when the inversion crosses its threshold value, $N^* = N^*_{th}$. The population of molecular levels and the photon mode are calculated as a function of time. The population of molecular levels is normalized to the total number of molecules. The figure shows population trajectories for N_3, N_2, N_1 and $N^* = N_2 - N_1$, as well as pump and output rate trajectories. The pump pulse is given by the term rN_0 in Equation 3.11-3.12, and output pulse by the term n_{ph}/τ_{cav} in Equation 3.10. The pump and output pulses have arbitrary units in y axis but they are in scale with respect to each other.

In the example simulation here, the system is pumped with a Gaussian shaped pulse arriving at $t = 0$, having a FWHM of 100 fs. The molecule lifetimes are of $\tau_{21} = \tau_{20} = 500$ ps, $\tau_{32} = \tau_{10} = 50$ fs, and the cavity lifetime is $\tau_{cav} = 75$ fs. The β-factor is given here a value of 0.001 which is based on a typical inverse value of the non-linear increase of the output intensity at the threshold for our plasmonic lattice lasers.

3.4 Bose-Einstein statistics

Bose-Einstein condensate is a manifestation of the quantum statistics of bosons by a macroscopic occupation in the ground state [48]. If at given temperature there is a high enough density of bosons with thermalized population over all available quantum states of the system, then all additional particles brought into the system must go into the ground state forming a BEC. The requirement can be formulated as follows: 1) given a fixed number of bosonic particles (e.g. in a trap potential), there is a critical temperature below which the BEC emerges, 2) at a fixed temperature, there is a critical density of particles above which the BEC emerges. The original theory of BEC was formulated for non-interacting particles. The first BECs were observed with dilute *weakly interacting* gases of alkali atoms at ultralow temperatures [48].

At thermodynamic equilibrium, bosons follow the Bose-Einstein statistics, given by the distribution function [49]

$$n_i(E_i) = \frac{g_i}{\mathrm{e}^{(E_i-\mu)/(k_\mathrm{B}T)} - 1}, \tag{3.17}$$

which describes the expected number of particles in an energy state i, with energy E_i. Here, g_i is the degeneracy of energy state i, μ is the chemical potential that defines the ground state energy of the system, k_B is the Boltzmann constant and T is the absolute temperature. In contrast, fermions follow the Fermi-Dirac statistics

$$n_i(E_i) = \frac{g_i}{\mathrm{e}^{(E_i-\mu)/(k_\mathrm{B}T)} + 1}. \tag{3.18}$$

The main difference between these two quantum statistics is that two or more fermions cannot simultaneously occupy the same energy state of the system (Pauli exclusion principle) but there is no such restriction for bosons. This can lead to macroscopic population of the ground state, so-called Bose-Einstein condensation. At high temperatures and low particle densities, when the quantum effects are negligible, the statistics of both bosons and fermions can be described with the Maxwell-Boltzmann distribution function

$$n_i(E_i) = g_i\,\mathrm{e}^{-(E_i-\mu)/(k_\mathrm{B}T)}, \tag{3.19}$$

which is derived for classical non-interacting particles (ideal gas). Even at the condensation regime, the thermalized population in higher energy states can be approximated with the Maxwell-Boltzmann distribution that displays the temperature of the system. The thermalized population in higher energies is typically referred as a *thermal tail*.

As stated above, the condensation occurs below a critical temperature and above a critical density. This condition corresponds to the point when the de Broglie wavelength of the condensing particles becomes comparable to the particle distance, i.e., the wave functions of the particles start to significantly overlap. De Broglie wavelength is given by

$$\lambda_\mathrm{B} = \sqrt{\frac{2\pi\hbar^2}{m_\mathrm{eff}k_\mathrm{B}T}}, \tag{3.20}$$

and it is inversely proportional to both the temperature T and effective mass of the particle, m_eff. A smaller effective mass gives a longer de Broglie wavelength so

bosons with a very small effective mass can lead to a BEC at higher temperature. The critical temperature of Bose-Einstein condensation scales with the effective mass of the condensing particles as [48]

$$T_c \propto \frac{\hbar^2 n^{2/3}}{m_{\text{eff}} k_{\text{B}}}, \tag{3.21}$$

where n is the particle density. The effective mass can be estimated from the dispersion relation, $E(k)$, which gives energy of the quasiparticle as a function of its momentum (wave number k being proportional to the momentum). If the dispersion can be approximated as a parabola, the effective mass can be calculated from

$$E(\mathbf{k}) = E_0 + \frac{\hbar^2 \mathbf{k}^2}{2m_{\text{eff}}}. \tag{3.22}$$

One can say that the steeper the parabolic dispersion the smaller the effective mass. A flat dispersion would correspond to an infinite effective mass (localized excitation), and on the other hand, dispersion of light (massless photons) in free space is linear. In Publication IV, we have calculated the effective mass of the SLR excitations to be of the order 10^{-7} electron masses, which enables the condensation at room temperature.

3.5 Strong coupling and coupled-modes model

In this section I develop the coupled-modes model used in Publications I and V. In general, two modes are coupled if they can exchange energy. If the exchange of energy quantum is faster than the decay of the modes, the frequencies of initial modes are modified and new eigenstates are formed for the coupled system. In this limit, the system is said to enter the strong coupling regime. An avoided crossing of these new hybridized modes arises in the dispersion at the location where the initial modes intersect (i.e. are in resonance). The avoided crossing is called normal mode splitting (in quantum physics Rabi splitting) and its size is directly proportional to the coupling strength of the modes.

3.5.1 Coupling of classical harmonic oscillators

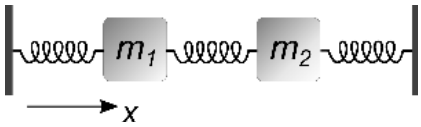

Figure 3.9. Mass-spring oscillator system used as a paradigm model of a strongly coupled system.

We begin by using a paradigm model of two classical harmonic oscillators that show a normal mode splitting when strongly coupled [201]. The treatment here follows the one in [184]. In this example, let us think of two mechanical spring-mass oscillators coupled with a third spring, see Figure 3.9. We assume no gravity, equal

masses $m_1 = m_2 = m$, and that the spring constant of all three springs is the same, k. Thus, the normal mode of the individual oscillators has the same resonant frequency $\omega_0 = \sqrt{\frac{k}{m}}$. The masses move along the x axis, and we denote the displacement of the left and right masses as $x_1(t)$ and $x_2(t)$, respectively. The equations of motion are

$$m\frac{d^2x_1}{dt^2} = -kx_1 + k(x_2 - x_1) = -2kx_1 + kx_2 \tag{3.23}$$

$$m\frac{d^2x_2}{dt^2} = -kx_2 + k(x_1 - x_2) = -2kx_2 + kx_1. \tag{3.24}$$

We expect oscillatory motion with the same angular frequency ω, and by substituting $x_1(t) = A_1e^{i\omega t}$ and $x_2(t) = A_2e^{i\omega t}$ we obtain

$$-\omega^2 mA_1e^{i\omega t} = -2kA_1e^{i\omega t} + kA_2e^{i\omega t} \tag{3.25}$$

$$-\omega^2 mA_2e^{i\omega t} = -2kA_2e^{i\omega t} + kA_1e^{i\omega t}, \tag{3.26}$$

and further

$$(\omega^2 m - 2k)A_1 + kA_2 = 0 \tag{3.27}$$

$$kA_1 + (\omega^2 m - 2k)A_2 = 0, \tag{3.28}$$

which in matrix form yields

$$\begin{pmatrix} \omega^2 m - 2k & k \\ k & \omega^2 m - 2k \end{pmatrix} \begin{pmatrix} A_1 \\ A_2 \end{pmatrix} = 0. \tag{3.29}$$

We can solve the eigenvalues by setting the determinant equal to zero, and obtain $\omega_1 = \sqrt{\frac{k}{m}}$ and $\omega_2 = \sqrt{\frac{3k}{m}}$. These are the resonant frequencies of the normal modes of the coupled system. By substituting ω_1 and ω_2 to Equation 3.29, we can calculate the eigenvectors (A_1, A_2) and get (1,1) and (1,-1). The first normal mode of the coupled system becomes

$$\eta_1 = \begin{pmatrix} x_1^1(t) \\ x_2^1(t) \end{pmatrix} = \frac{1}{\sqrt{2}} \begin{pmatrix} 1 \\ 1 \end{pmatrix} cos(\omega_1 t + \varphi_1), \tag{3.30}$$

which corresponds to both masses moving in the same direction, at the same time, at frequency ω_1. And the second normal mode becomes

$$\eta_2 = \begin{pmatrix} x_1^2(t) \\ x_2^2(t) \end{pmatrix} = \frac{1}{\sqrt{2}} \begin{pmatrix} 1 \\ -1 \end{pmatrix} cos(\omega_2 t + \varphi_2), \tag{3.31}$$

which corresponds to the masses moving in the opposite direction, at the same time, at frequency ω_2.

3.5.2 Jaynes-Cummings model

A similar treatment can be applied to coupled systems in quantum mechanics. The Hamiltonian can be used to calculate the time evolution of a quantum state, and for a quantized bosonic field interacting with a two-level atom, one can write a so-called Jaynes-Cummings Hamiltonian [202]:

$$\hat{H} = \frac{1}{2}\hbar\omega_{eg}\hat{\sigma}_z + \hbar\omega\hat{a}^\dagger\hat{a} + \frac{1}{2}\hbar\Omega(\hat{a}\hat{\sigma}_+ + \hat{a}^\dagger\hat{\sigma}_-), \tag{3.32}$$

where ω_{eg} is the atomic transition frequency and ω the frequency of a photonic mode, $\hat{a}^\dagger$ and $\hat{a}$ are the creation and annihilation operators of a photon, $\hat{\sigma}_+ = |e\rangle\langle g|$ and $\hat{\sigma}_- = |g\rangle\langle e|$ are the raising and lowering operators of the two-level atom, $\hat{\sigma}_z = |e\rangle\langle e| - |g\rangle\langle g|$ is the atomic inversion operator, and Ω is the coupling constant.

The quantized field can be described in the basis of Fock states, $|n\rangle$, where n is simply the number of photons in the photonic mode. By combining the Fock states with $|e\rangle$ and $|g\rangle$, which describe the excited and ground state of the two-level atom, the Hamiltonian can be written in a basis [22]:

$$\begin{pmatrix} 1 \\ 0 \end{pmatrix} = |e\rangle|n\rangle \quad \begin{pmatrix} 0 \\ 1 \end{pmatrix} = |g\rangle|n+1\rangle.$$

Here, the first basis vector describes a state in which the atom is in the excited state and the photonic mode has n photons. The second basis vector describes a state in which the atom is in the ground state and the mode has $n+1$ photons. The Hamiltonian yields

$$\hat{H} = \hbar\omega\left(n + \frac{1}{2}\right)\begin{pmatrix} 1 & 0 \\ 0 & 1 \end{pmatrix} + \frac{\hbar}{2}\begin{pmatrix} -\delta & 2\Omega\sqrt{n+1} \\ \hbar\Omega\sqrt{n+1} & 2\omega\left(n+\frac{1}{2}\right)+\delta \end{pmatrix}, \tag{3.33}$$

where $\delta = \omega - \omega_{eg}$ is the detuning of the photonic mode and the atomic transition frequency. By combining the Hamiltonian into a single matrix, it becomes

$$\hat{H} = \begin{pmatrix} \hbar\omega\left(n+\frac{1}{2}\right) - \frac{\hbar\delta}{2} & \hbar\Omega\sqrt{n+1} \\ \hbar\Omega\sqrt{n+1} & \hbar\omega\left(n+\frac{1}{2}\right) + \frac{\hbar\delta}{2} \end{pmatrix}, \tag{3.34}$$

where the diagonal elements are the energies of the initial modes and the off-diagonal element is the coupling constant. If the system is at the zero-photon limit, $\langle n\rangle = 0$, which is typical when characterizing experimental systems with weak probes, a possible energy splitting of the modes is called the vacuum Rabi splitting. Diagonalizing Equation 3.34 results in the following eigenvalues that correspond to the eigenenergies of the new hybrid modes:

$$E_{1n} = \hbar\omega\left(n + \frac{1}{2}\right) - \frac{1}{2}\hbar\sqrt{\sigma^2 + 4\Omega^2(n+1)} \tag{3.35}$$

$$E_{2n} = \hbar\omega\left(n + \frac{1}{2}\right) + \frac{1}{2}\hbar\sqrt{\sigma^2 + 4\Omega^2(n+1)} \tag{3.36}$$

where

$$\omega_{Rabi} = \sqrt{\delta^2 + 4\Omega^2(n+1)}, \tag{3.37}$$

is the Rabi frequency. Normalized eigenvector coefficients give the relative weights of the initial modes in the hybrid modes of the strongly-coupled system. The sum of squared coefficients should be normalized to unity, as they correspond to probability of being in each initial state.

At resonance $\delta = 0$, the Hamiltonian in Equation 3.34 can be written as

$$\hat{H}_I = \begin{pmatrix} E_1 & \hbar\Omega \\ \hbar\Omega & E_2 \end{pmatrix}, \tag{3.38}$$

where E_1 and E_2 are the energies of the uncoupled (initial) modes. This is the coupled-modes model that can be also extended to more than two modes, and can be fitted to experimentally measured dispersions to obtain the coupling strength between the modes. The eigenenergies take the form

$$E_{1n} = \hbar\omega\left(n + \frac{1}{2}\right) - \hbar\Omega\sqrt{n+1} \tag{3.39}$$

$$E_{2n} = \hbar\omega\left(n + \frac{1}{2}\right) + \hbar\Omega\sqrt{n+1}, \tag{3.40}$$

and the eigenstates are hybrids of the two uncoupled states with equal weights

$$|1n\rangle = \frac{1}{\sqrt{2}}(-|e\rangle|n\rangle + |g\rangle|n+1\rangle) \tag{3.41}$$

$$|2n\rangle = \frac{1}{\sqrt{2}}(|e\rangle|n\rangle + |g\rangle|n+1\rangle), \tag{3.42}$$

and the Rabi frequency becomes

$$\omega_{Rabi} = 2\Omega\sqrt{n+1}. \tag{3.43}$$

Figure 3.10 presents an example of the Rabi splitting in the frequency domain, and respective Rabi oscillation in the time domain, for a hypothetical strongly coupled system of two modes whose initial resonant frequencies intersect as a function wave vector. It is important to note that although the resonant frequencies are typically investigated as a function of wave vector (actual dispersion relation), the coupled-modes model can successfully describe the strongly coupled system if the two modes can be brought into resonance as a function of *any given system parameter*. In Publication I the resonant frequency of the SLR mode is scanned as a function of lattice period, and LSPR as a function of particle diameter.

For a number of N quantum emitters coupled to an optical mode, in the semi-classical and quantum models, the coupling constant has the relation [22]

$$\Omega \propto \sqrt{\frac{\omega_0}{\hbar\epsilon_0}} d \sqrt{\frac{N}{V}}, \tag{3.44}$$

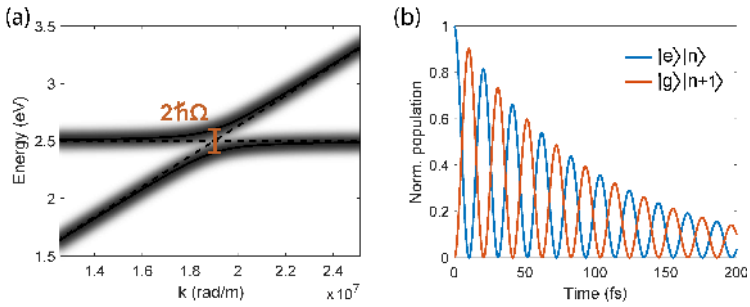

Figure 3.10. (a) Schematic illustration of Rabi splitting of two modes intersecting as a function of wave vector **k**. The initial modes can be thought, for example, as a dispersive optical mode (diagonal dashed line, $E = \hbar ck$) and a molecular absorption transition (horizontal dashed line). The hybrid modes are depicted with blurred solid lines. The size of the Rabi splitting is $\hbar\Omega$, the splitting must be larger than the mode linewidths to be experimentally observable. Such a splitting is the experimental signature of strong coupling. (b) Illustration of Rabi oscillation that occurs in the time domain at frequency ω_{Rabi}. The population oscillates between the states $|e\rangle|n\rangle$ and $|g\rangle|n+1\rangle$. Here, ω_{Rabi} is calculated for a coupling constant of 100 meV that corresponds to the splitting of $\hbar\Omega = 200$ meV, indicated in (a). This is on the same order as the largest experimentally observed splittings in Publication I. The population is set to decay exponentially with a time constant of $\tau = 100$ fs. The trajectories are obtained for $\cos^2(\Omega t)e^{-t/\tau}$ and $\sin^2(\Omega t)e^{-t/\tau}$.

where ω_0 is the frequency at resonance, d is the dipole moment, ϵ_0 the vacuum permittivity and V the mode volume. Here, one can see that the coupling strength is directly proportional to the dipole moment (and number of emitters) and inversely proportional to the mode volume. In the experiments, the actual mode volume is very difficult to estimate but we know the concentration of the emitters, that is $\frac{N}{V}$. Therefore, we may conclude that the coupling strength, and thus the experimentally observed Rabi splitting should scale with a square root of concentration, $\sqrt{\frac{N}{V}}$, if the splitting is truly due to the coupling of the modes. The square-rood dependence is used as a standard criteria for proving strong coupling in the system, studied also in Publication I.

A comprehensive review on strong coupling in plasmonic structures can be found in [22], along with the theoretical discussion of classical, semi-classical and quantum models for strong coupling.

4. Experimental methods

In this chapter, I introduce the sample fabrication and the optical measurements. The plasmonic nanoparticle arrays are fabricated with electron beam lithography (EBL) on glass substrates in a clean room environment. The transmission, reflection and photoluminescence properties of the samples are studied with different variations of a home-built experimental setup.

4.1 Sample fabrication

The plasmonic nanoparticle arrays consist of either silver or gold particles that are fabricated on 0.17 mm or 1 mm thick glass substrates (borosilicate, pre-cleaned Schott Nexterion) with electron beam lithography. First, approximately a 200 nm thick resist layer of Poly(methyl methacrylate) (PMMA) is spin-coated on the substrate. The resist solution has 4 wt% of 950,000 molecular weight PMMA in anisole (made by MicroChem), and the spinning is done at 3000 rpm for 60 s. After evaporating 10 nm of aluminium as a conduction layer, the sample is exposed by an electron-beam writer (Vistec, EPBG 5000pES). The aluminium layer is etched away with a 1:1 mixture of de-ionized water and AZ351B developer containing NaOH, and the resist is developed in a MIBK(methyl isobutyl ketone):IPA(isopropanol) 1:3 solution for 15 s and in pure IPA for 30 s. The sample is blow-dried with a nitrogen pistol. Silver or gold is evaporated onto the substrate with the same electron-beam evaporator as the aluminium, and finally the excess metal is removed with a lift off in acetone. For the lift off the samples are typically brought outside the clean room, and the sample is immersed in acetone for over night or at lest a few hours. For the silver samples, a 1 nm layer of silver is evaporated and oxidized prior to the final silver deposition as an adhesion layer (after plasma-cleaning inside the evaporator), whereas for the gold samples a 1 nm layer of titanium is used to better adhesion. A scanning electron microscope (SEM Zeiss Supra 40) image of a typical sample is shown in Figure 4.1.

It is worth mentioning that a distorting Fabry–Pérot interference may occur in the measured spectra for the 0.17 mm thick substrates, when a high wavelength resolution is used. A Fabry–Pérot interference can arise from the reflection by the substrate's front surface and the metal nanoparticle array, which together form a Fabry–Pérot

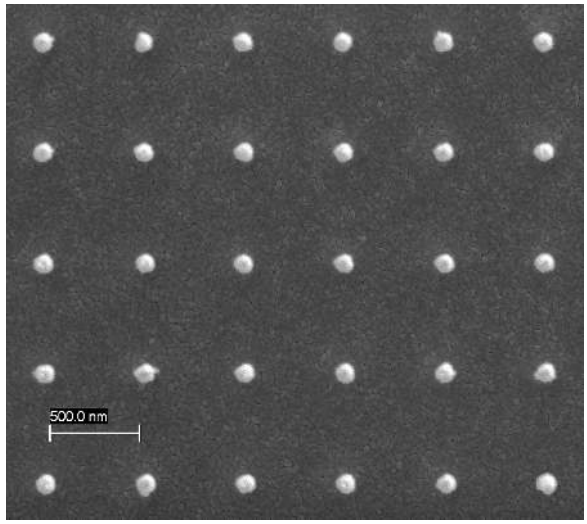

Figure 4.1. A zoomed-in scanning-electron microscope image of a typical nanoparticle array sample. For the imaging, the sample is coated with an additional metal layer. Here, the nanoparticles are gold and the conduction coating is aluminium.

cavity with a length of the substrate thickness. On the contrary, for 1 mm thick substrates, no such effect is visible due to a small enough free spectral range even in the near infrared. Another advantage of the 1 mm thick substrates is that they are much easier to handle in the fabrication process.

Depending on the experiment, either a ~50 nm thick layer of dye molecules in PMMA (host polymer matrix) is spin-coated on top of the array, or the nanoparticles are overlaid with a liquid solution of dye molecules. In the first case, an index-matching oil is applied between the glass substrate and a glass superstrate to create a homogeneous refractive index environment, which is important for obtaining high-quality SLRs [31]. In the latter case, the solvent is index-matched to the glass. We use a mixture of 1:2 (Dimethyl sulfoxide)DMSO:(Benzyl alcohol)BA that has a refractive index of ~1.52, calculated by a weighted average of the individual components ($n_{\mathrm{DMSO}} = 1.479$ and $n_{\mathrm{BA}} = 1.539$). A droplet of liquid dye solution is sandwiched between two glass slides creating a dye layer with a thickness of the order $10\,\mu\mathrm{m}$, or alternatively, the dye solution is sealed inside a 1 mm thick Press-to-Seal silicone isolator chamber (Sigma-Aldrich). The silicon isolator is first pressed between two 1 mm thick glass slides forming an airtight chamber. After that, the dye solution is injected with a needle, from the side of the chamber, through the silicon. A second needle is used as a valve so that the air can come out when the solution is injected into the chamber, see Figure 4.2. Note that a 1 mm thick molecule layer is huge compared to the extension of the SLR electric fields in the perpendicular direction from the lattice plane. The active region of the dye lies within a few hundred nanometers from the lattice, as has been proven experimentally in Publications II-III.

The molecular concentration c_{dye} in the final PMMA layer is calculated from the

Figure 4.2. A photograph of the sample at the preparation stage where the dye solution is injected into the silicon chamber (orange circle) with the help of two needles. The diameter of the chamber is 20 mm. A matrix of multiple nanoparticle arrays is visible in light reflection at the center. A 1 mm thick layer of 80 mM solution of IR-792 is completely opaque.

ratio between dye molecules and PMMA in the solution, that is spin coated onto the sample, by taking into account the density of the solid PMMA. The dye concentration becomes

$$c_{dye} = \frac{m_{dye}}{A\left(1+\frac{A}{1-A}\right)M_{dye}V_{mix}}\frac{\rho_{pmma}}{\rho_{anisole}}, \tag{4.1}$$

where A is the weight-% of the PMMA in anisole, m is mass, M_{dye} is the molar mass, ρ is density and V_{mix} is the volume of PMMA-in-anisole solution. To obtain a desired concentration one needs to calculate the mass of dye molecule m_{dye}, that is typically in powder form, with respect to V_{mix}. In Publication I we use Rhodamine 6G chloride ($C_{28}H_{31}N_2O_3 \cdot Cl$; Sigma-Aldrich [203]) in PMMA matrix. For better dissolution, the Rhodamine 6G (R6G) is first dissolved in a small amount of ethanol and then further mixed with the PMMA in anisole.

The liquid dye molecule solution on top of the nanoparticle arrays is prepared by first DMSO:BA in 1:2 ratio. Then the chosen dye is dissolved to mixture in a desired concentration that can be calculated as

$$c_{dye} = \frac{m_{dye}}{M_{dye}V_{mix}}, \tag{4.2}$$

where V_{mix} is now the volume of DMSO–BA mixture. Many dyes dissolve in DMSO at higher concentration than in BA, so the dye can be dissolved first to DMSO before mixing with BA. In addition, heating the solvent at a hot plate, for example at 80 °C, accelerates the dissolution process and can assist higher concentrations to dissolve. In Publication II, we use R6G chloride and later on R6G perchlorate ($C_{28}H_{31}N_2O_3 \cdot ClO_4$; Sigma-Aldrich), as we learned that R6G chloride is highly corrosive to all metals except stainless steel [204], and it destroys our silver nanoparticle arrays. In Publication III, we use IR-140 perchlorate ($C_{39}H_{34}Cl_2N_3S_2 \cdot ClO_4$; Sigma-Aldrich) which has been used also by others [92, 94] as the gain medium in plasmonic

nanoparticle array lasers. In Publications IV-V we use another infrared laser dye, IR-792 perchlorate ($C_{42}H_{49}N_2S \cdot ClO_4$; Sigma-Aldrich), that has been chosen mainly because of its better solubility in DMSO:BA mixture, important for achieving high concentrations and thus strong coupling.

After working with Rhodamine 6G in the visible, we have chosen to work with near-infrared dyes because of two main reasons: 1) In the red side of the visible spectrum, plasmonic resonances have lower losses and the quality factor of LSPRs is higher. This also increases the Q factor of SLRs in the near-infrared. 2) Gold can replace silver as the nanoparticle material because in the near-infrared gold has almost as low losses as silver. Gold provides a major benefit: it does not suffer from oxidation. IR-792 was chosen after testing several different dye molecules that have their absorption and emission spectra around 750–900 nm. For IR-792, the absorption peak is around 800 nm and it emits around 855 nm. The advantages of IR-792 are that 1) it dissolves in DMSO:BA mixture at very high concentrations of over 200 mM, in contrast to IR-140, that dissolves up to 30 mM, for instance, and 2) IR-792 does not bleach as quickly and it provides higher gain than many other infrared dyes that were tested in lasing experiments. The tested dye molecules are listed in Table 4.1.

For all measured IR dyes, the highest photoluminescence efficiency (at a given pump fluence) is obtained at 1 mM concentration. However, we have never observed lasing with such a low concentration. Optimal concentrations of infrared dyes for lasing in the plasmonic lattice lasers are between 10–30 mM, but this has not been systematically studied. Concentrations of higher than 200 mM typically emit too poorly to obtain any lasing action, which is most probably due decreased quantum yield (QY) resulting from aggregation and self-quenching of the molecules.

The nanoparticle array geometry, dye molecule, concentration and other specific details of the samples used in each experiment are introduced within the corresponding section in Chapter 5.

Table 4.1. Dye molecules that have been investigated for lasing experiments. If the absorption and emission wavelengths are measured, the concentration (in the 1:2 DMSO:BA mixture) is given in parenthesis, otherwise a reference to the literature value is given. The fourth column, Max. c_{dye}, indicates the maximum concentration that has been successfully dissolved in the 1:2 DMSO:BA mixture. It may not be the highest possible value, but a note is given in the fifth column, if higher concentrations have been unsuccessfully tried. In addition, I have written down a mark how well the dye molecule has worked in the lasing experiments. I have compared the QY of the molecules at different concentrations, at a given pump fluence, and find that for IR-140, the QY at 25 mM drops to 34% of the QY at 1 mM (highest efficiency). For IR-792 the QY at 25 mM drops to 6%, for IR-783 to 4%, and for IR-806 to 1.4%. At 100 mM, for IR-792 the QY drops to 1.4%, for IR-783 to 0.7%, and for IR-806 to 0.4%. IR-783 seems like a good candidate for the lasing experiments as its emission spectrum does not shift (or broaden) much when the concentration is increased, its QY stays decent as a function of concentration (>25 mM), and it emits something even at 280 mM (0.16% of the QY at 1 mM). Unfortunately, it bleaches quickly under optical pumping. All FEW dyes [205], particularly FEW S0260, appear as good candidates. However, IR-792 was chosen for the studies in this dissertation as it was the first tested emitter that worked nicely in the lasing and BEC experiments at high concentrations.

	Abs. peak (nm)	Em. peak (nm)	Max. c_{dye}	Notes
Rhodamine 6G	530 [206]	552 [206]	100 mM	Good (at visible λ).
DCM	468 [203]	627 [207]	40 mM	Good (at visible λ).
IR-140 perchl.	835 (0.1 mM)	872 / 897 (1 / 25 mM)	25 mM	Good, insoluble at higher c_{dye}.
IR-792 perchl.	811 (150 mM)	845 / 858 (1 / 200 mM)	200 mM	Good.
IR-780 perchl.	780 [203]	834 / 844 (1 / 200 mM)	200 mM	Product discontinued.
IR-780 iodide	780 [203]	–	–	Dissolves very poorly.
IR-783	801 (0.1 mM)	829 / 840 (1 / 280 mM)	280 mM	Bad, bleaches quickly.
IR-806	827 (0.1 mM)	856 / 865 (1 / 100 mM)	100 mM	Bad, bleaches quickly.
IR-820	820 [203]	881 (100 mM)	100 mM	OK, not thoroughly tested.
FEW S0094	813 [205]	875 (100 mM)	100 mM	OK.
FEW S0260	816 [205]	867 / 877 (15 / 100 mM)	330 mM	Good.
FEW S0712	819 [205]	881 (100 mM)	200 mM	OK.
Styryl 9M	584 [203]	815 [207]	40 mM	OK, insoluble at higher c_{dye}.
Perylene Red	578 [208]	613 [208]	–	–

4.2 Experimental setup

We study the optical modes of the plasmonic lattices, and their photoluminescence properties when combined with dye molecules. We are interested in the spectrum of transmitted, reflected or emitted light and its angular distribution (2D k space), as well as the spatial intensity distribution on the sample (2D real space). A schematic of the experimental setup is depicted in Figure 4.3. Let us first focus on the basic principles of the image formation in the spectrometer CCD camera.

In the spectrometer camera, the x axis of the CCD pixel array is assigned to spectral information, λ_0, and the y axis to either angular information, θ_y, or spatial position on the sample, y. Photon energy can be calculated from the free space wavelength, λ_0,

$$E = hc/\lambda_0, \tag{4.3}$$

and the angle of collected light, θ_y, is related to the in-plane wave vector on the

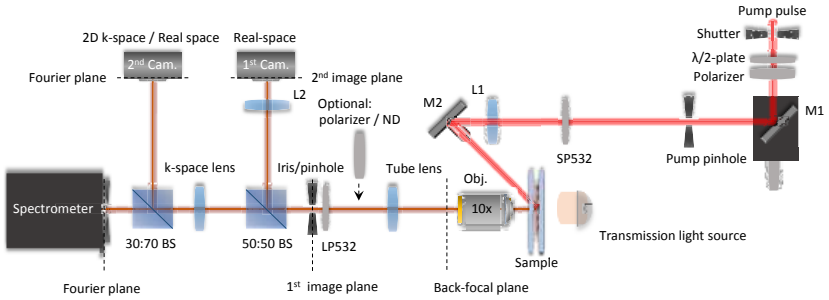

Figure 4.3. Experimental setup used in the experiments for Publication II. Transmission light source is a halogen lamp that covers a spectrum from the visible wavelengths to near infrared. The ratio of Reflection:Transmission in each beam splitter (BS) is marked as (R:T).

sample,

$$k_y = k_0 sin(\theta_y) = 2\pi/\lambda_0 sin(\theta_y). \tag{4.4}$$

It means that we can measure the angle-resolved (k-space) spectrum as a crosscut of the three-dimensional space of (k_x,k_y,E), by selecting a slice of it at $k_x = 0$ with the spectrometer slit. Alternatively, we can measure the spatially resolved (real space) spectrum along y axis of the sample. Crosscuts of the (k_x,k_y,E) space reveal the dispersion of optical modes in the sample (see discussion of the SLR modes in Section 3.2.

The spectrometer takes a 1:1 image of the entrance slit to the CCD array. In the case of real space spectrum, a real space image of the sample is focused onto the slit and the y position at the CCD array is directly proportional to the y position on the sample. However in the case of k-space spectrum, back-focal plane of the objective (Fourier plane) is focused on to the slit and the y position at the CCD array (pixel row number p) is mapped to the angle θ_y as

$$\theta_y(p) = \arctan\left(\frac{p - p_0}{p_r}\tan(\theta_{max})\right) - \theta_{tilt}, \tag{4.5}$$

where p_0 is the center and p_r is the half-height of the back-focal plane image at the CCD array. Yet, θ_{max} is the maximum collection angel of the objective

$$\theta_{max} = \arcsin\left(\frac{\mathrm{NA}}{n}\right), \tag{4.6}$$

where NA is the numerical aperture of the objective, and the refractive index $n = 1$, as the light is collected in air. Finally, θ_{tilt} is the sample tilt in vertical direction, with respect to the optical axis, and can be calculated from

$$\theta_{tilt} = \arctan\left(\frac{p_0' - p_0}{p_r}\tan(\theta_{max})\right), \tag{4.7}$$

where p_0' is the pixel row that corresponds to the sample normal (Γ-point).

Equation 4.5 assumes perfect optics without distortion meaning that p is linearly proportional to $\tan(\theta_y)$. This assumption gives a reasonable accuracy for a small NA and small magnification objective, for instance 0.3 NA 10x, that is used in the experiments in this dissertation. However, for a larger NA and magnification objective (e.g. 0.6 NA 40x), a calibration with a diffraction grating must be applied for accurate mapping of the CCD pixel rows to angle [101]. The calibration procedure is explained in detail in [209].

Next, we will go through the relevant setup configurations used in the experiments presented in this dissertation. The basic principles are the same for all configurations, particularly the detection path, except for the one in Publications I. There we measure only the transmittance of the samples. The transmitted light is collected with an objective, focused to an optical fiber, and guided through the fiber into the spectrometer that produces a singe spectrum at a time. The incident angle is restricted with an aperture to NA ≈ 0.04 at normal incidence, to effectively measure crosscuts of dispersion at $k_x = 0$. This configuration is trivial compared to those used in Publications II-V.

In Publication II, we employ the experimental setup presented in Figure 4.3. The detection path is built so that multiple images, with different information, can be collected simultaneously. For instance, one can acquire the 2D real space, 2D k-space and k-space spectrum (crosscut of 2D k-space), at the same time, which makes the measurement faster and more reliable. The most important component in the detection path is the microscope objective. The back-focal plane of the objective contains the angular information of the collected light. The objective and tube lens create an image of the sample to the first image plane, where we place an iris / pinhole that is used to restrict the area on the sample from which the light is collected. The first image plane is relayed to the CMOS camera, 1st Cam., and the k-space lens focuses the angular information (Fourier plane) to the spectrometer slit and to 2nd Cam. We employ a Princeton Instruments spectrometer Acton SP2500i with a PIXIS 400F CCD camera. The 1st and 2nd Cam. are identical CMOS cameras, Point Gray (nowadays FLIR) Grasshopper3.

In the photoluminescence measurements, the sample is optically excited with an external laser pulse. The excitation (or pump) pulse is generated by Coherent Astrella ultrafast Ti:Sapphire amplifier, which operates at 1 kHz repetition rate. The pulse has a center wavelength of 800 nm, and a duration of < 35 fs with a bandwidth of 30 nm, at the laser output. The pulse is inserted into an optical parametric amplifier (OPA), TOPAS prime by Light Conversion, and converted to a desired wavelength of $\lambda_{\text{pump}} = 500$ nm (we pump the dye Rhodamine 6G). The pump pulse is linearly polarized and the pump fluence (pulse energy) is adjusted with a combination of a $\lambda/2$-plate and a linear polarizer. A short-pass filter (Semrock SP532) in the excitation path is used in combination with a long-pass filter (Semrock LP532) in the detection path to filter out the pump pulse in the measured luminescence spectra. The pump pulse is spatially cropped with a pinhole which is imaged onto the sample with the lens L1 (see Fig. 4.3). The sample is pumped from the side of the objective at an angle of $\sim 45°$. Optionally, there is also a linear polarization filter in the detection path. We study the sample luminescence as a function of pump fluence, and the measurement

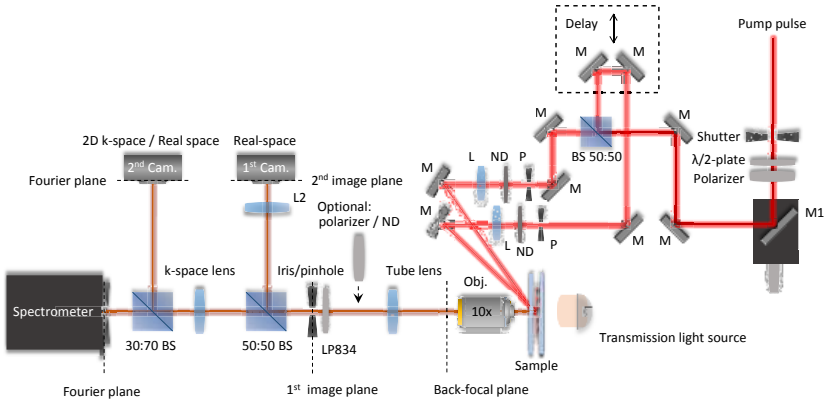

Figure 4.4. Experimental setup in the pump-probe experiments for Publication III.

is automatized with a home-built LabVIEW software that controls the pump pulse shutter, power adjustment and the acquisition of the images from the multiple cameras. The integration time of the spectrometer camera is automatically adjusted during the measurement to avoid saturation with increasing pump fluence.

In Publication III, we conduct pump-probe experiments with a setup configuration depicted in Figure 4.4. We apply so-called *double-pump spectroscopy* technique, that uses pump and probe pulses which are identical except the pulse energy. The double-pump technique utilizes the non-linearity of luminescence intensity at the lasing threshold. The measurement is similar to the one explained above but now the pump pulse is taken directly from Astrella ($\lambda_{\mathrm{pump}} = 800$ nm, dye IR-140), the pump pulse is split into two and the relative time delay of the two pulses is controlled with a motorized translation stage. The fluence of each pulse can be controlled separately with metal-coated continuously variable neutral-density (ND) filter wheels, after the pinholes (P), see Figure 4.4. We study the sample luminescence as a function of the time delay, with a chosen ratio of the pump and probe pulse fluences (typically $P_{\mathrm{probe}} = 0.05 P_{\mathrm{pump}}$). The pump pulse fluence, P_{pump}, is chosen to be just above the lasing threshold, so that the sample luminescence is at the non-linear regime. The double-pump technique is explained more in detail together with the results of Publication III, in Section 5.2.2. The same pump-probe setup is also utilized in Publication IV.

In Publications IV-V, the luminescence spectrum is studied as a function of y position of the lattice (real space spectrum). For this, an additional lens must be inserted before the k-space lens, see Figure 4.5. In Publication IV, the pumping geometry is still the same as presented in Figure 4.3, whereas in Publication V, the setup is the one depicted in Figure 4.5. Now the sample is pumped through the objective at normal incidence, which turns out to be crucial for the successful BEC experiments. The main reason for this is most probably the fact that when the pump pulse hits the sample at 45 degree angle, and lattice size is $100 \times 100\,\mu$m, there is a 230 fs difference in time when the pulse arrives in the opposite edges of the lattice.

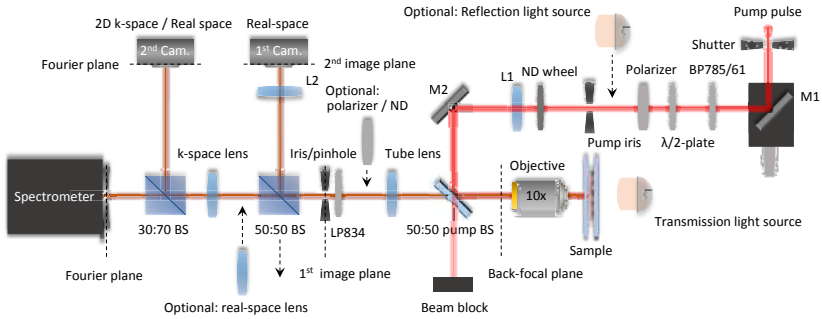

Figure 4.5. Experimental setup used in the experiments for Publication V. The essential difference here is the pumping through the objective at normal incidence. Also the power adjustment is done with an ND filter wheel instead of λ/2-plate – polarizer combination. Reflectance of the sample is measured by placing a white light source behind the pump iris.

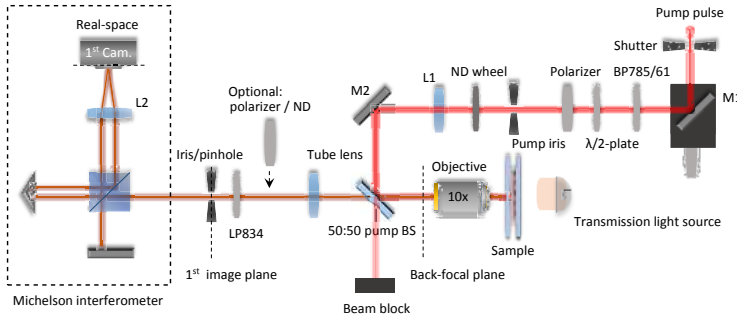

Figure 4.6. Michelson interferometer setup used in Publication V. A similar setup is used in Publication IV with the difference that the sample is pumped at an angle from the side of the objective.

As our pump pulse duration is of the order 100 fs, and the observed dynamics of the condensation phenomenon is in a similar timescale, it obviously makes a huge difference if the pump comes at an angle or at normal incidence. The inverted design and pumping at normal incidence is crucial for simultaneous excitation of the dye molecules over the whole nanoparticle array. It also prevents any asymmetry in the spatial distribution of the excited molecules around the nanoparticles, with respect to lattice plane. By imaging the pump iris onto sample we obtain a uniform flat intensity profile for the pump spot. In Publications IV we use a pump wavelength of $\lambda_{\mathrm{pump}} = 750$, converted by the OPA, and in Publication V we use $\lambda_{\mathrm{pump}} = 800$, taken directly from Astrella. The dye molecule is IR-792 in both cases.

Figure 4.6 shows the Michelson interferometer that is used for measuring the spatial coherence of light emitted from two different positions of the plasmonic lattice in Publications IV and V. In the Michelson interferometer, the real space image of the sample is split into two with a 50:50 beam splitter, the image in one of the arms is inverted with a hollow roof retro-reflector, and the two images are overlapped in

the camera pixel array. This way the spatial coherence between positions $-y$ and $+y$, or $-x$ and $+x$, can be measured, depending on the axis along which one of the images is inverted. The first-order correlation function describing the degree of spatial coherence is directly proportional to fringe contrast C, and is given by

$$g^{(1)}(-y,y) = \frac{\langle E^*(-y)E(y)\rangle}{\sqrt{\langle E(-y)^2\rangle\langle E(y)^2\rangle}} = C(y)\frac{I(-y)+I(y)}{2\sqrt{I(-y)I(y)}}, \tag{4.8}$$

where $E(y)$ is the electric field amplitude and $I(y)$ is the luminescence intensity at position y, respectively. The fringe contrast can be obtained simply by

$$C(y) = \frac{I_{max} - I_{min}}{I_{max} + I_{min}} \tag{4.9}$$

but if the image shows a lot of intensity variation that is not produced by the spatial coherence, the fringe contrast at a spatial frequency given by the Michelson interferometer geometry can be extracted with a Fourier analysis of the spatial frequencies. The Fourier method used in Publication V is explained in detail in the supplementary material of Publication V.

In Publication V, besides the pump fluence dependence, the luminescence is measured also as a function of pump pulse duration, which is adjusted by tuning the stretcher-compressor of Astrella ultrafast amplifier. The pulse duration is measured by removing the lens L1 and placing a similar lens in front of the objective (in the place of the transmission light source) so that the pump beam is again collimated after this lens. Then, the pump beam is guided into an autocorrelator (APE pulseCheck 50) and the pulse duration is measured with a Gaussian fit to the autocorrelation function.

In Publications IV-V, we estimate the photon number of condensate pulses. The measured luminescence intensity can be related to a photon number by doing an intensity calibration. We measure a strongly attenuated beam of Astrella, and the total counts given by the spectrometer CCD camera is compared to the average power measured by a power meter (Ophir Vega). The measured average power of 167 nW corresponds to $6.7 \cdot 10^8$ photons/pulse whereas the measured count number in the CCD camera is $8.4 \cdot 10^6$. This results in a conversion factor of ~80 photons/count. The collection optics, including the beam splitters (setup in Fig. 4.5), reduce the signal roughly by a factor of 2.5, at λ_{pump} = 800 nm. Finally, the nanoparticle array is assumed to radiate equally to both sides and the luminescence is collected only in one side. The photon number yields

$$n_{ph} \approx 80 \times 2.5 \times 2 \times \frac{A}{A_0} N_{\mathrm{spectr}} \tag{4.10}$$

where N_{spectr} is the total number of counts in the spectrum, A is the measured area of a luminous sample determined by the spectrometer slit width, and A_0 is total area of the luminous sample. In Publication V, we use a slit width of 500 µm that corresponds to 27 µm at the sample, so we collect luminescence from an area that is about $\frac{1}{4}$ of the 100 µm wide luminous nanoparticle array.

4.2.1 Alignment of the optical setup

The alignment of the optical setup is essential, especially for repeatability and precise control of the BEC formation in Publication V. The alignment is done with the help of a HeNe reference laser that is used to define the optical axis (z-axis). First, the reference beam is aligned to travel horizontally, and parallel to the optical rail (XT66SD by Thorlabs) on which the detection path optics is placed. The spectrometer is located such that the reference beam enters the spectrometer exactly through the center of the entrance slit. The reference beam now defines the coordinates of the optical axis in the spectrometer CCD camera. Then, the k-space lens is placed on the rail and adjusted so that the laser light focuses to the smallest possible spot in the CCD camera, at the optical axis. The position of the 2nd Cam. is adjusted accordingly. The tube lens is placed so that the laser light is again collimated after the k-space lens (checked far away by using an additional mirror), and then, the 1st Cam. is positioned so that the laser has its tightest focus in the image. After that the iris / pinhole is placed in the focus of the 1st Cam.

The angle of the objective is adjusted with the help of reflection from the front surface, and after that, the objective is aligned in the xy-plane to focus the reference beam to the optical axis in the CCD camera. The pump beam is brought to the same optical axis with the reference beam by adjusting the mirror M2 and the pump beam splitter (pump BS), see Figures 4.5-4.6. For this, the objective is removed. The alignment of the pump beam is confirmed by the reflection from the back surface of the objective, with the 1st Cam. Finally, the lens L1 is adjusted so that the reflection from the objective back surface goes to the same position in the 1st Cam.

5. Results

5.1 Strong coupling of lattice resonances and dye molecules

Plasmonics has enabled reaching strong coupling at room temperature and without microcavities on planar and nanostructured surfaces [22]. In Publication I, we show strong coupling between the absorption transition of an organic dye molecule Rhodamine 6G and both LSPR and SLR modes of the plasmonic lattice. We experimentally observe avoided crossing (Rabi splitting) of the modes which is the fingerprint of strong coupling. As mentioned in Section 3.5, the avoided crossing can be studied as a function of any system parameter that can be varied to scan one of the resonance across the other one. In all other experiments presented in this dissertation, the crossing of the modes is investigated as a function of in-plane wave vector, meaning the *true* dispersion relation of the modes, but in Publication I the crossing is investigated as a function of inverse lattice period that is proportional to the reciprocal lattice wave vector, $\mathbf{k} = 2\pi/p$, and determines the SLR energy. Additional experiments are done as a function of particle size, to scan the LSPR energy.

In Publication I, the samples consist of several nanoparticle arrays of $40\times40\,\mu\mathrm{m}^2$ in size. The nanoparticles are cylindrical in shape, made of silver, and arranged in a symmetrical square lattice, see Figure 5.1. Sample I consists of 21 arrays, where the measured mean particle diameter is 89 nm, and the lattice period is varied from 297 to 495 nm. Sample II consists of 23 arrays, with a mean particle diameter of 79 nm and lattice period between 279 and 496 nm. And Sample III consists of 23 arrays, with a mean particle diameter of 65 nm and lattice period between 275 and 491 nm. In all samples the nanoparticle height is 30 nm. A ~50 nm thick layer of R6G in PMMA is spin coated on top of the arrays with R6G concentrations of 200 mM (Sample II), and 25, 50 and 200 mM (Sample III). We measure transmittance of the arrays with white light at normal incidence, which reveals the modes at the Γ-point ($k_x, k_y = 0$). For this, we employ an optical microscope (Nikon Eclipse TE2000) and a fiber coupler to the spectrometer. The particle diameter and lattice period are measured with a scanning electron microscope, after coating the sample with 10 nm of gold. Statistical analysis of the particle diameter is performed with an image processing tool ImageJ.

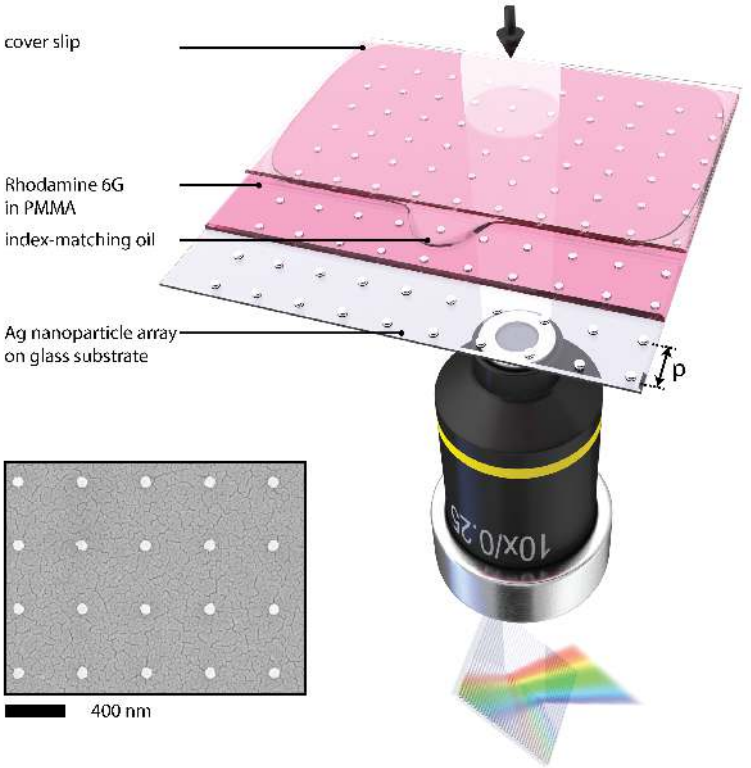

Figure 5.1. Samples and the experimental setup in Publication I. A sample consists of several nanoparticle arrays with different lattice periods, p, on a glass substrate. The arrays are composed of cylindrical silver nanoparticles that are arranged in a square lattice ($p_x = p_y$). Optionally, a layer of R6G dye molecule in PMMA is spin-coated on top. The sample is immersed in index-matching oil and covered by another glass slide. We measure the transmission of one array at a time to obtain the transmission spectra as a function of the reciprocal lattice vector, $k = 2\pi/p$. White light is mildly focused onto the array at normal incidence, and after passing through the sample, the light is collected with an objective and guided to a spectrometer. A zoomed-in SEM image of a fabricated nanoparticle array is shown as an inset. Figure reprinted with permission from Publication I (© 2014 American Chemical Society).

The experimental results are explained with finite-difference time-domain (FDTD) simulations, coupled-dipole approximation (CDA) calculations, and coupled-modes models. In the FDTD simulations, the molecule layer is included with an effective refractive index that is calculated from measured absorbance of Rhodamine 6G using the Kramers–Kronig relation [210]. The FDTD simulations are performed with a commercial software (Lumerical Solutions). In the CDA, every nanoparticle is considered to be a single dipole with a polarizability α. The polarization $P_i = \alpha E_i$ is calculated for each particle ($i = 1...N$), and E_i takes into account both the incident electric field and the field radiated by all other particles. At normal incidence, the extinction cross section can be obtained by calculating an effective polarizability, $\alpha_{\text{eff}} = 1/(\alpha^{-1} - S)$, where S is a retarded dipole sum [28]. More details of the applied CDA method can be found in the supplementary information of Publication I.

5.1.1 Characterization of optical resonances in bare lattices

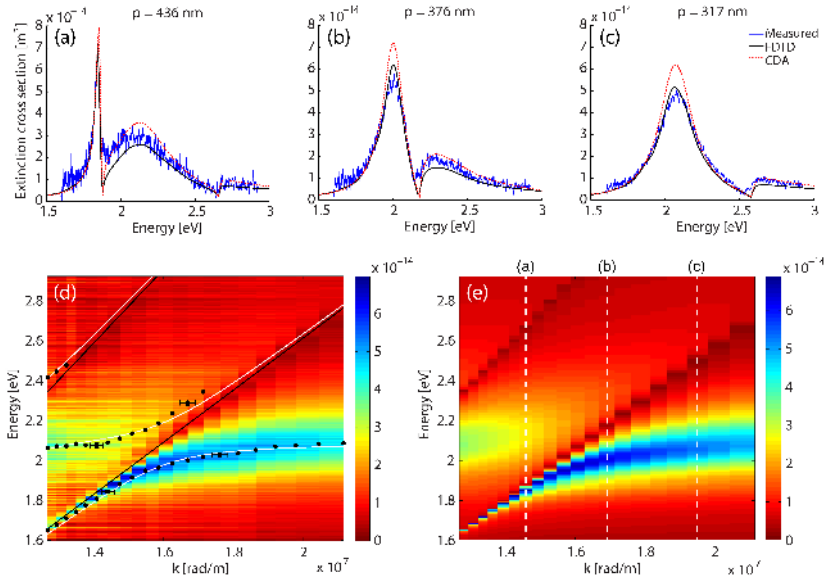

Figure 5.2. Measured and simulated extinction spectra of the nanoparticle arrays on Sample I, without dye molecules (bare arrays). (a-c) show the measurements, FDTD simulations, and CDA calculations for periods that result in having the SLR below, at, and above the LSPR frequency, respectively. The FDTD simulations and CDA calculations match to the measurements nearly perfectly. (d) Measured extinction spectra as a function of the reciprocal lattice vector, $k = 2\pi/p$. The diagonal black lines display the locations of uncoupled DOs, and the horizontal black line indicates the LSPR frequency. The extinction maxima are shown with black dots and the white lines are the fitted SLR modes (hybridized modes) given by a three-coupled-modes model. Typical error estimates in the measurement are indicated with error bars for a few selected data points. The vertical errorbars are based on the error in peak position fitting and spectrometer calibration, whereas horizontal error bars are based on SEM measurement accuracy (~1%) when defining the lattice period. (e) Extinction spectra obtained with FDTD simulations. The vertical dashed lines indicate the k-values that correspond to the spectra in (a-c). Figure reprinted with permission from Publication I (© 2014 American Chemical Society).

First, we characterize the optical modes in a bare plasmonic lattice, without molecules. In Figure 5.2, we plot the measured and calculated extinction spectra of Sample I. Figure 5.2a-c present three different cases where the lattice period p is chosen such that the SLR is below (a), at (b), and above (c) the LSPR in energy. The match of the spectra obtained with the FDTD simulation and CDA calculation is nearly perfect to the measured spectra. Extinction cross section of the nanoparticle lattice is defined for a single unit cell

$$\sigma_{\text{ext}} = (1-T)p^2 = (1-\frac{I_{\text{array}}}{I_{\text{ref}}})p^2, \tag{5.1}$$

and it describes the area per unit cell that should be opaque, so that to the fraction $1-T$ of incident light is blocked. Here, I_{array} is the intensity transmitted through the array, and I_{ref} is the intensity transmitted through an equal-sized area of the sample

outside the array (through substrate).

Figure 5.2d-e present the measured and simulated extinction spectra as a function of inverse lattice period. An avoided crossing of two SLR modes is observed when the first DO crosses the LSPR. This can be considered as normal mode splitting (Rabi splitting) and strong coupling of the DOs with the LSPR. A three-coupled modes model

$$\hat{H} = \begin{pmatrix} E_{\mathrm{LSPR}} & \hbar\Omega_{12} & \hbar\Omega_{13} \\ \hbar\Omega_{12} & E_{\mathrm{SLR},1}(k) & 0 \\ \hbar\Omega_{13} & 0 & E_{\mathrm{SLR},2}(k) \end{pmatrix}, \tag{5.2}$$

is fitted to the maxima of the extinction spectra, and yields coupling constants of $\hbar\Omega_{12} = 107 \pm 1$ meV between the LSPR and the first DO, and $\hbar\Omega_{13} = 142 \pm 49$ meV between the LSPR and the second (diagonal) DO, at higher energy. The coupling between the DOs is set to zero. The extinction maxima are found from the measured spectra by fitting a Gaussian to the local environments of each maximum. The error limits for coupling constants are obtained by doing the fitting for data points that have been moved within their error limits. The errors for individual data points are estimated based on the measurement accuracy of the lattice period, the accuracy of extinction peak fitting, and spectrometer calibration.

5.1.2 Adding the dye molecules

Figure 5.3 presents the extinction spectra of Sample II without and with a 200 mM R6G layer on top. When the dye is added, the initial modes shift and exhibit splittings at the multiple crossing points of the uncoupled modes. For example, we can observe a clear down shift of the LSPR. To characterize the coupling strength between different modes, the system is described with a five-coupled-modes model, including: LSPR, two DOs, R6G main absorption peak, and R6G absorption shoulder. In this model the dispersions of the hybrid modes (as a function of $k = 2\pi/p$) are given by the eigenenergies of the matrix:

$$\hat{H} = \begin{pmatrix} E_{\mathrm{LSPR}} & \hbar\Omega_{12} & \hbar\Omega_{13} & \hbar\Omega_{14} & \hbar\Omega_{15} \\ \hbar\Omega_{12} & E_{\mathrm{SLR},1}(k) & 0 & \hbar\Omega_{24} & \hbar\Omega_{25} \\ \hbar\Omega_{13} & 0 & E_{\mathrm{SLR},2}(k) & \hbar\Omega_{34} & \hbar\Omega_{35} \\ \hbar\Omega_{14} & \hbar\Omega_{24} & \hbar\Omega_{34} & E_{\mathrm{R6G},1} & 0 \\ \hbar\Omega_{15} & \hbar\Omega_{25} & \hbar\Omega_{35} & 0 & E_{\mathrm{R6G},2} \end{pmatrix}, \tag{5.3}$$

where the diagonal elements are the energies of uncoupled initial modes, and off-diagonal elements describe the couplings. The couplings between the R6G main peak and shoulder, as well as between the two DOs are set to zero. For Sample II, the coupling constants obtained from the three-coupled-modes model (Eq. 5.2) in the case without R6G are: $\hbar\Omega_{12} = 129 \pm 6$ meV and $\hbar\Omega_{13} = 106 \pm 34$ meV, between the LSPR and the first DO, and the LSPR and the second DO, respectively. In the case with 200 mM of R6G, the coupling constants obtained from Equation 5.3

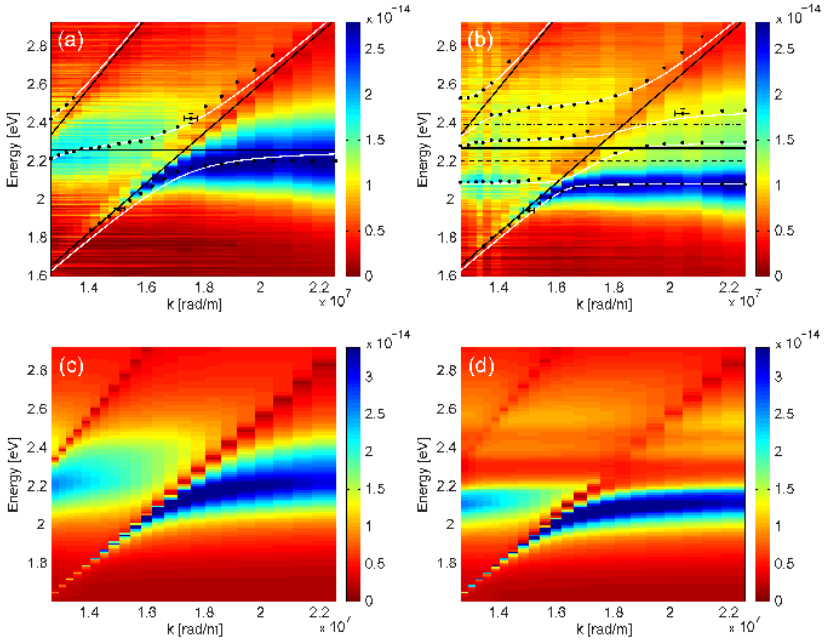

Figure 5.3. Measured and simulated extinction spectra of the nanoparticle arrays on Sample II. (a) Measurement without dye molecules, and (b) with 200 mM concentration of R6G. Again, the diagonal black lines indicate the DOs and the horizontal black line the LSPR. The dashed line is the measured R6G absorption peak position and dash-dotted line is the absorption shoulder. Fits to the extinction maxima (black dots) with a three-coupled-modes model (a), and a five-coupled-modes model (b), are shown with white lines. Typical error estimates are indicated with error bars for a few selected data points. (c-d) The corresponding FDTD simulations without (c) and with (d) dye molecules. The simulations match excellently to the measured data. Figure reprinted with permission from Publication I (© 2014 American Chemical Society).

yield: $\hbar\Omega_{12} = 116 \pm 16$ meV (LSPR and first DO), $\hbar\Omega_{13} = 66 \pm 13$ meV (LSPR and second DO), $\hbar\Omega_{14} = 132 \pm 9$ meV (LSPR and R6G main peak), $\hbar\Omega_{15} = 110 \pm 8$ meV (LSPR and R6G shoulder), $\hbar\Omega_{24} = 52 \pm 10$ meV (first DO and R6G main peak), $\hbar\Omega_{25} = 37 \pm 21$ meV (first DO and R6G shoulder), $\hbar\Omega_{34} = 45 \pm 17$ meV (second DO and R6G main peak), and $\hbar\Omega_{35} = 41 \pm 12$ meV (second DO and R6G shoulder).

The number of R6G molecules that reside within the mode volume of the lattice modes is difficult to estimate. Anyhow, there is a significant fraction of dye molecules that do not interact strongly, i.e., are not involved in the strong coupling, and do not contribute to the Rabi splitting. Intuitively one could expect that the molecules closer to the particles couple more strongly and exhibit a modified extinction spectrum (with Rabi splitting), whereas molecules further away exhibit an unmodified spectrum. A similar division to strongly coupled emitters and the rest has been used in [211]. To find the hybrid modes of coupled system in this case, we cannot calculate the extinction of the coupled system directly from the total transmittance of the system, which is a product of transmittance of the substrate, the array, and the R6G film.

The extinction cross section of the coupled system is obtained by

$$\begin{aligned}\sigma_{\text{ext,coupl. sys.}} &= \sigma_{\text{ext,total}} - \sigma_{\text{ext,R6G}} \\ &= (1 - T_{\text{total}})p^2 - (1 - T_{\text{R6G}})p^2 \\ &= (T_{\text{R6G}} - T_{\text{total}})p^2 = \left(\frac{I_{\text{R6G}}}{I_{\text{ref}}} - \frac{I_{\text{total}}}{I_{\text{ref}}}\right)p^2. \end{aligned} \tag{5.4}$$

where we subtract the extinction spectrum of the dye layer, $\sigma_{\text{ext,R6G}}$, from the total extinction spectrum, $\sigma_{\text{ext,total}}$. Here, $\sigma_{\text{ext,R6G}}$ is obtained through the R6G film on the substrate, and $\sigma_{\text{ext,total}}$ through the whole stack of the substrate, the array, and the R6G film. Reference intensity I_{ref} is again measured just through a clear area of the glass substrate. This subtraction procedure slightly overestimates the value of unmodified absorption of the uncoupled R6G molecules, due to the volume of nanoparticles and the volume of molecules that are strongly coupled. However, based on a careful analysis in the supplementary information of Publication I, a possible error in the energy locations of the obtained extinction maxima is small.

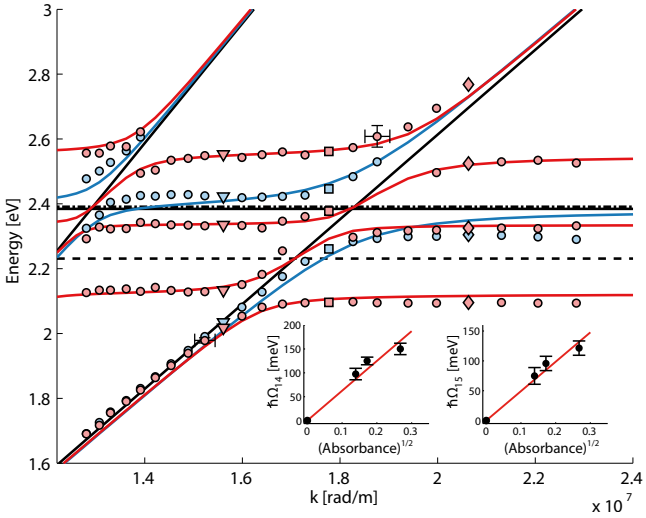

Figure 5.4. Dispersions of the measured extinction maxima of Sample III without R6G (blue dots) and with a 200 mM R6G film (red dots). The corresponding fits with coupled-modes models are displayed with blue and red lines. The insets show the coupling constant for the coupling between LSPR and R6G main absorption peak ($\hbar\Omega_{14}$), and between LSPR and R6G absorption shoulder ($\hbar\Omega_{15}$) for four different concentrations (0, 25, 50 and 200 mM). Both $\hbar\Omega_{14}$ and $\hbar\Omega_{15}$ follow the expected square-root dependence on the absorbance of the R6G film, absorbance being directly proportional to concentration (number of molecules per mode volume, N/V). Figure reprinted with permission from Publication I (© 2014 American Chemical Society).

Since the diagonal elements in Equation 5.3 are determined experimentally, the model has eight parameters that are determined by finding the best fit to the experimental data. This is a lot of fitting parameters, and based on our study the goodness of the fit depends mainly on only four parameters. We find that the parameters $\hbar\Omega_{24}$,

$\hbar\Omega_{25}$, $\hbar\Omega_{34}$, and $\hbar\Omega_{35}$, describing the direct coupling between the DOs and R6G are less important than the rest. Details of this analysis can be found in the supplementary information of Publication I.

The extinction spectra of Sample III is presented in Figure 5.4, again without and with a 200 mM layer of R6G, now overlaid onto the same axes. The two insets show how the coupling strengths between the R6G main absorption peak and the LSPR, and between the R6G absorption shoulder and the LSPR, scale linearly with the square root of R6G concentration. The coupling constants are now obtained with the truncated model of only four fitting parameters, explained above. The linear $\sqrt{\frac{N}{V}}$ – dependence confirms that the avoided crossings in the extinction spectra are due to strong coupling. Figure 5.5 shows how the maxima of the extinction spectra evolve as a function of concentration, for Sample III. The fitted coupling constants as a function R6G concentration are summarized in Table 5.1. Importantly, all parameters are roughly of the same magnitude. And even though the direct couplings between the molecule absorption transitions and the DOs are omitted, these modes actually *are* strongly coupled, and the coupling is mediated by the R6G coupling to the LSPR. Similar hybrids of three modes are formed in quantum mechanical Λ-systems [202].

We confirm that the molecules are strongly coupled mainly to the plasmonic part (LSPR) of the SLR, by studying the crossing of LSPR and the R6G absorption transitions far away from the DO location, see Figure 5.6a. Finally, we perform an FDTD simulation to estimate how many molecules actually participate in the strong coupling. The simulation is explained in Figure 5.6b. A single nanoparticle is enveloped by a 200 mM R6G disk, and the R6G disk size is increased until the extinction spectrum of the system saturates to a certain shape. At that point, the R6G disk volume corresponds to $3{\cdot}10^4$ molecules, which gives an estimate for the number of strongly coupled molecules *per particle*.

Table 5.1. The coupling constants for different R6G concentrations for Sample III.

	LSPR – first DO	LSPR – second DO	LSPR – R6G main	LSPR – R6G shoulder
No R6G	108 ± 11 meV	59 ± 8 meV	–	–
25 mM	76 ± 6 meV	87 ± 13 meV	98 ± 12 meV	75 ± 14 meV
50 mM	105 ± 9 meV	61 ± 6 meV	125 ± 8 meV	96 ± 12 meV
200mM	95 ± 6 meV	79 ± 7 meV	150 ± 12 meV	121 ± 12 meV

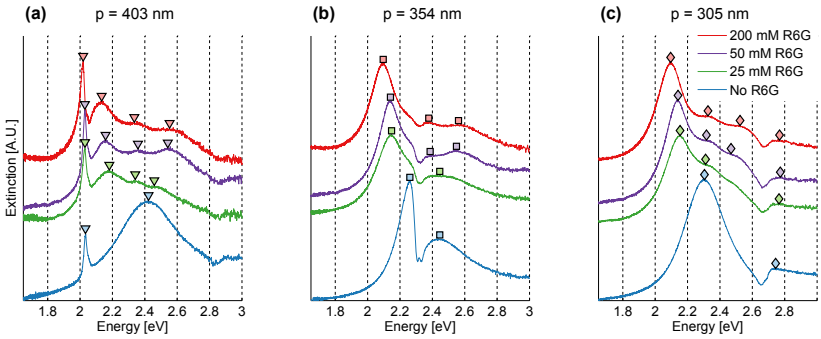

Figure 5.5. Examples of the measured extinction spectra of nanoparticle arrays on Sample III. (a) The SLR is at a lower energy compared to the LSPR and the R6G resonances. (b) The SLR is in between the R6G main absorption peak and the LSPR. (c) The SLR is at a higher energy compared to the LSPR and the R6G resonances. Peak positions in the spectra are indicated with triangles, squares and diamonds, and they correspond to the fitted extinction maxima. The same symbols with one-to-one correspondence are shown in Figure 5.4 for 0 and 200 mM concentration. The spectra exhibit a clear evolution as a function of concentration such that the extinction peaks of the strongly coupled hybrid modes become more prominent, as they emerge and separate further away from each other. Figure reprinted with permission from Publication I (© 2014 American Chemical Society).

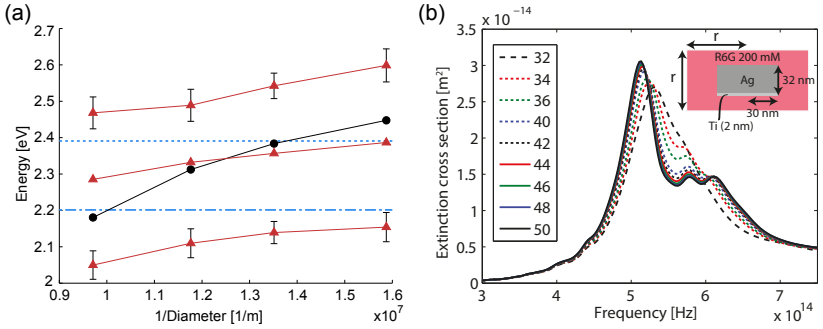

Figure 5.6. Strong coupling between the single particles (LSPR) and 200 mM R6G (absorption peak and shoulder). (a) The measured extinction maxima are plotted as a function of inverse particle diameter. Black dots show the measurement without and red triangles with the molecule layer. The blue dash-dotted line indicates the R6G absorption peak and the dotted line indicates the R6G absorption shoulder. (b) FDTD simulation of a silver disk enveloped by a PMMA disk doped with a 200 mM concentration of R6G molecules. The silver disk has a diameter of 60 nm and height of 30 nm, and it is placed on a 2 nm thick titanium adhesion layer. The radius of the PMMA disk is equal to its height, and is stepped from 32 to 50 nm. With the FDTD method, we calculate the extinction cross section of the two concentric disks and present the result as a function of frequency. At first the resonance of the particle splits and shifts relatively fast but the evolution saturates at larger PMMA disk size. Figure reprinted with permission from Publication I (© 2014 American Chemical Society).

5.2 Plasmonic nanoparticle array lasers

The SLR modes can provide feedback for laser operation by the backward and forward scattering modes resulting in a standing wave at the band-edges located at the Γ-point, or other crossing points of the DOs in the dispersion. For instance, we have also observed lasing at K-points of a plasmonic honeycomb lattice [101]. In Publication II, we demonstrate lasing in both the bright and the dark mode of a plasmonic lattice, in the visible wavelengths. In Publication III, we study the dynamics of ultrafast pulse generation in plasmonic lattice lasers with a single color pump-probe technique, called *double-pump spectroscopy*.

5.2.1 Lasing in both bright and dark modes

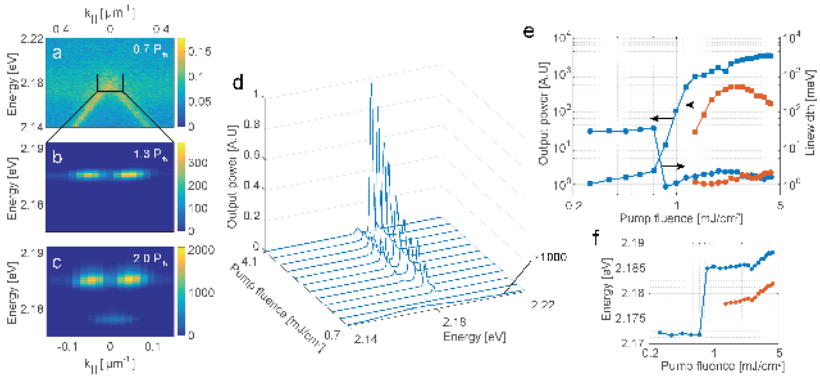

Figure 5.7. Measured luminescence of a $100\times100\,\mu m^2$ silver nanoparticle array (period $p_x = p_y = 375\,nm$ and particle diameter $d = 60\,nm$). Angle-resolved luminescence spectra for pump fluences (a) $P = 0.7P_{th}$, (b) $P = 1.3P_{th}$ and c) $P = 2.0P_{th}$. (d) Spectra integrated along $k_{||}$ as a function of pump fluence. (e) Output power of the lower energy (red squares) and higher energy (blue squares) mode as a function of pump fluence. Also shown are the linewidths for the lower and higher energy modes as red and blue dots, respectively. (f) The mode energies with increasing pump fluence. Above threshold, we obtain 10^3 increase in luminescence intensity, mode linewidth of 0.2 nm and a remarkably low beam divergence of $\Delta\theta_{FWHM} = 0.3°$. Figure adapted with permission from Publication II (© CC BY 4.0).

In Publication II, we study the photoluminescence of square arrays of $100\times100\,\mu m^2$ in size, the arrays are made of cylindrically shaped silver nanoparticles with a nominal diameter of 60 nm and height of 30 nm. Lasing at a wavelength range of $560-580$ nm is obtained with 30 mM Rhodamine 6G solution, with periodicities of $p = 370-390$ nm. Figure 5.7 presents the results for a sample with $p = 375$. Angle resolved spectra are shown in Figure 5.7a-c for different pump fluencies. Below threshold, only spontaneous emission is observed which is slightly enhanced at the dispersion of the SLR mode due to higher local density of states. At threshold, a very narrow and intense lasing peak occurs at 2.185 eV, and well above the threshold a second peak emerges at 2.178 eV. We associate the lower energy peak with a bright mode and the upper one with a dark mode of the lattice because for cylindrical particles the bright mode lies lower in energy (see Fig. 3.3). Interestingly, the upper energy mode exhibits

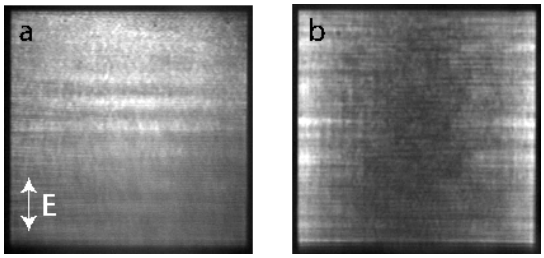

Figure 5.8. Real space images of two different nanoparticle arrays where a bright mode (a) and a dark mode (b) is lasing. (a) The bright mode has a nearly uniform intensity distribution over the array with a moderate maximum at the center. (b) Strikingly, the dark mode has the highest intensity at the edges of the array and a dark region at the center. Figure adapted with permission from Publication II (© CC BY 4.0).

an even beating pattern along $k_{||}$, with a minimum intensity at $k_{||} = 0$, whereas the lower energy mode has its maximum at $k_{||} = 0$.

Figure 5.7d shows the evolution of the emission peaks integrated over $k_{||}$ between -0.2 to $0.2\,\mu\mathrm{m}^{-1}$. In Figure 5.7e, the output power and linewidth are plotted for both peaks separately as a function of pump fluence. A very clear threshold is observed around $0.77\,\mathrm{mJ/cm}^2$ after which we obtain a thousand times increase in the output power (luminescence). The linewidth just after the threshold drops to only 0.2 nm and the beam divergence is 0.3° (half angle). Here, the output power is calculated by integrating the area under the peak over energy. Figure 5.7f shows the peak positions as a function of pump fluence. A clear blue shift can be observe above the threshold, which is typical for lasing, and can be for instance due to frequency pulling effect that drags the lasing frequency toward the highest gain.

Figure 5.8 shows real space images of laser emission by two nanoparticle arrays, the other one lasing in the bright and other one in the dark mode. We can observe a distinct difference between the two regarding their real space intensity distributions. The bright mode has maximum intensity in the center of the array and quite uniform distribution over the entire array. In contrast, the dark mode has a clear built-up of emission towards the two edges of the sample. The real space intensity distribution corresponds to the dipole moment distribution in the nanoparticles, because only oscillation with a non-zero dipole moment can radiate to the far field.

To intuitively understand the connection between the real space and the k-space intensity distribution (connected by the Fourier transform), let us use a double slit analogy. If a plane wave is incident on a slit, diffraction of the wave produces a sinusoidally varying intensity pattern onto a screen placed far away from the slit. The so-called diffraction pattern has its maximum at the optical axis. If a plane wave is incident on a double slit, the diffraction pattern in the far field again produces a maximum at the center. However, if the light passing through the two slits would be coherent but out of phase (phase shift of π), the diffraction pattern would produce a minimum at the center – an even beating pattern.

To explain the π-phase shift of radiation from the two opposite edges of the array, when lasing occurs in the dark mode, we need look at the polarization of the

nanoparticle in the cases of infinite and finite lattice. Figure 5.9 shows a calculation of two counter-propagating waves with a wavelength matching the lattice period. As discussed in Section 3.2, the bright mode has an anti-node and the dark mode has a node at each particle location, respectively. Therefore, in Figure 5.9, we place the node of the counter propagating waves at the nanoparticles. In the case of dark mode lasing, the finite size of the lattice triggers a dipole moment built-up with opposite phases towards the edges. This results from the fact that for a finite-sized array, the amplitude of counter propagating waves is not even over the whole array. For instance, particles at the right edge do not experience left-propagating wave (red) but only the right-propagating wave (blue). Note, that for an infinite lattice the dark mode would really be *dark* and would not radiate to the far-field. The finite size of the nanoparticle array breaks the translational symmetry and enables the out-coupling of the dark mode. The explanation is further elucidated in Figure 5.10.

The lasing experiment is repeated with different array sizes of 50–100 µm, in 10 µm steps, and as expected from the double slit analogy (for small angles), it is clearly observed that the separation of the two maxima at the dark mode energy scales as 1/(array size). This experiment supports the explanation above. The measured crosscuts and $\Delta k_{||}$ are presented in Figure 5.11. The coherent out-coupling from the opposite edges of the plasmonic lattice highlights the fact that the spatial coherence of the SLR mode that is lasing extends over the entire finite-sized array.

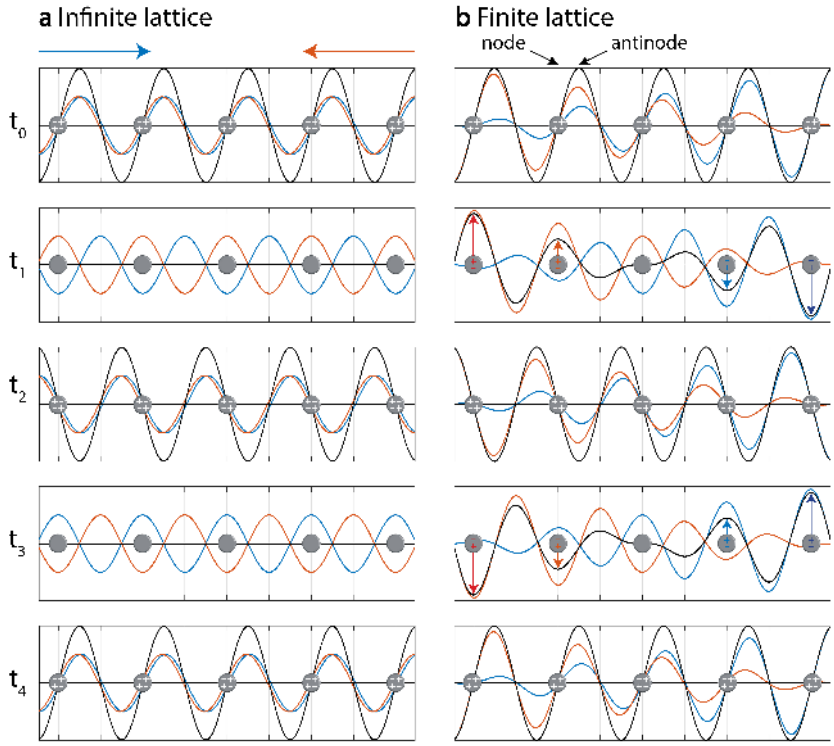

Figure 5.9. Comparison of the dark mode in infinite and finite lattices. The dark mode has a node at each nanoparticle (destructive interference at all times), which results in quadrupolar excitation at each nanoparticle with a zero dipole moment (a). However, unequal amplitudes of the right- and left-propagating waves result in a gradual built-up of a dipole moment toward the edges of the lattice, as shown in (b). The time step used for the simulation corresponds to a phase accumulation of $\pi/2$.

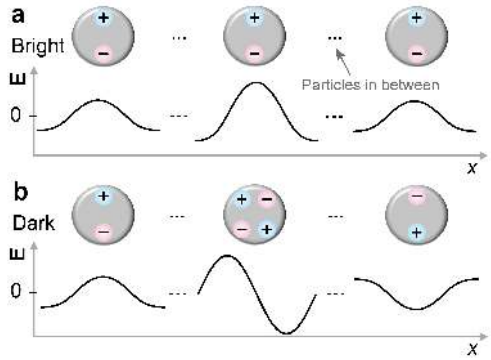

Figure 5.10. Evolution of the radiation fields in a finite-size array. (a) For the bright mode, dipoles across the array oscillate in phase due to constructive interference of the counter-propagating waves at each particle location. The amplitude at the edges, however, will be reduced as there are no particles and thus no radiation incident from the other side. Here we have assumed that the amplitude for both counter-propagating waves saturate to some value and does not built up across the entire array. Otherwise, there would be an equal amplitude for the standing wave at every particle location from edge to edge. (b) In contrast, for the dark mode, a quadrupole excitation is created at each nanoparticle (see Fig. 3.3). However, due to the finite size of the lattice, only the center particles of the array experience a perfect destructive interfere (at all times) because they are driven by left- and right-propagating waves of equal amplitudes. When moving away from the center, the destructive interference becomes gradually less complete because of unequal number of particles contributing to the left- and right-propagating waves. There is a gradual built up of a dipole moment in the charge oscillation at the particles. At the edge, the particles experience only radiation from the direction of the array center, which results in pure dipolar excitation. Moreover, the dipoles at the two edges are out of phase by π, leading to the observed even beating pattern in the far field. Figure reprinted with permission from Publication II (© CC BY 4.0).

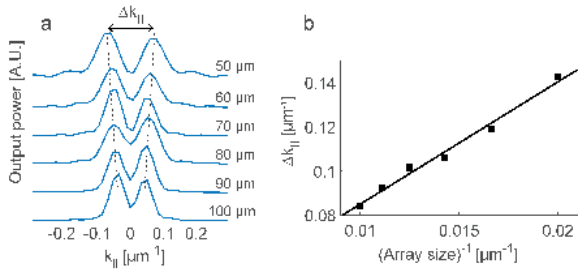

Figure 5.11. (a) Normalized constant energy cross sections of the dark mode lasing peak as a function of $k_{||}$ for different array sizes. (b) The separation of the peaks $\Delta k_{||}$ as a function of 1/(array size) showing a linear dependence that is expected from a double slit analogy. Figure adapted with permission from Publication II (© CC BY 4.0).

5.2.2 Ultrafast pulse generation

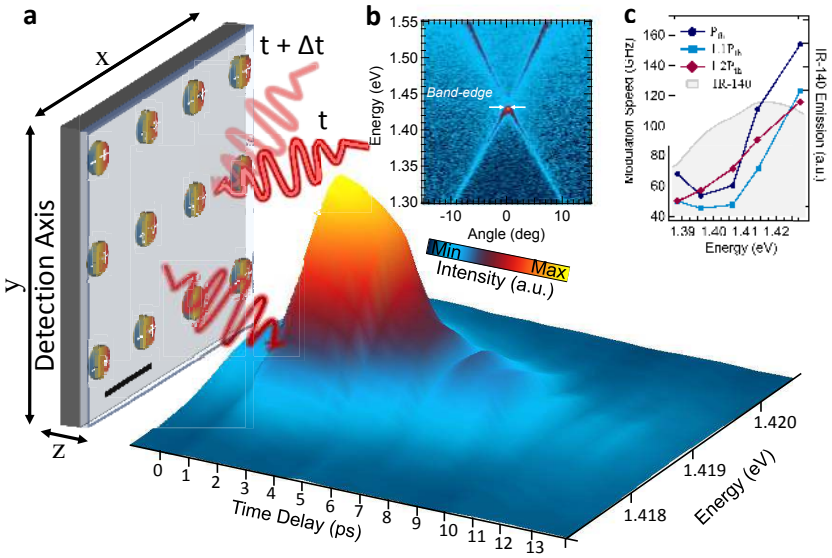

Figure 5.12. (a) Illustration of the double-pump spectroscopy technique. On the left is a schematic of the gold nanoparticle array pumped with a strong pulse and probed with a weak pulse, that is delayed by a time Δt. Both pulses are linearly polarized in x-direction and have the same center wavelength of 800 nm. The scale bar is 570 nm. On the right is a 3D contour plot of an experimentally acquired time-integrated luminescence spectrum as function time delay Δt. (b) Measured dispersion of the SLR mode (TE), the band-edge where lasing occurs is indicated by white arrows. (c) Output pulse modulation frequency (speed) as a function of the band-edge energy (array periods 565 – 585 nm). The modulation speed is calculated as a sum of the pulse built-up time and duration. We find that the modulation speed increases when tuning the band-edge towards the blue side of the IR-140 emission spectrum (shown as the gray area on the background). We reach more than 100 GHz modulation speeds. Figure reprinted with permission from Publication III (© CC BY 4.0).

In Publication III, we study the dynamics of ultrafast pulse generation of plasmonic lattice lasers with a double-pump spectroscopy technique that utilizes the non-linear increase of the photoluminescence around the lasing threshold [77]. The arrays consist of cylindrical gold nanoparticles in square lattice, with particle height of 50 nm and diameter varied between 80 – 120 nm. Infrared laser dye IR-140 in solution is used as the gain medium at 15 mM concentration. The system and experiment are illustrated in Figure 5.12.

The limit for time resolution of the double-pump technique is determined by the pulse duration. We can easily measure the pulse duration by scanning the time delay between the two pulses, Δt, from negative to positive side of $\Delta t = 0$ when both pulses hit the sample simultaneously. At zero time delay the pulses interfere and the interference pattern imprints to the real space distribution of dye emission, see Figure 5.13. The pulse duration can be extracted from the interference fringe visibility as a function of Δt, and by doing this we obtain a pulse FWHM of 70 fs.

Figure 5.14 shows the characteristics of the nanoparticle array laser studied in

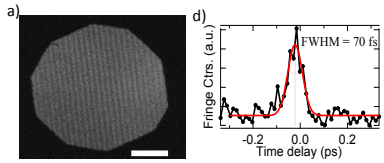

Figure 5.13. Photoluminescence of the dye solution when the pump and probe pulses hit the sample simultaneously causing interference fringes in the emission intensity. By scanning the time delay of the probe pulse, and extracting the fringe contrast in the image, we can measure the pulse duration on the sample and obtain a FWHM of 70 fs. Figure reprinted with permission from Publication III (© CC BY 4.0).

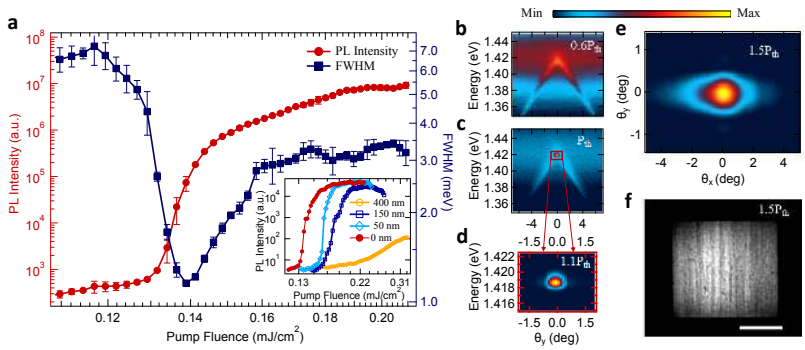

Figure 5.14. (a) A typical threshold curve of a gold nanoparticle array laser with a lattice periodicity of 570 nm and with 15 mM IR-140 gain solution. Red dots represent the band-edge photoluminescence intensity and blue dots the spectral linewidth. The inset shows the threshold curves when a 50, 150 and 400 nm thick PVA spacer layer is inserted between the nanoparticles and IR-140 molecules. Interestingly, the threshold pump fluence increases as a function of spacer thickness and with 400 nm PVA layer the lasing threshold is not any more reached. This highlights the importance of the plasmonic near-fields in the lasing action. (b-d) Angle-resolved luminescence spectra below (b) and above (c-d) threshold. (e) Angular distribution (2D k-space) image of the luminescence above threshold. Luminescence is more confined in y-direction ($\Delta\theta_y < 1°$) than in x-direction ($\Delta\theta_y \approx 3°$), which can be attributed to the x-polarized pump laser and therefore x-polarized nanoparticles. We have commonly observed that the momentum-space confinement is higher in the direction of the feedback. (f) Real-space image of laser emission at $1.5P_{th}$. The scale bar is 50 µm. Figure reprinted with permission from Publication III (© CC BY 4.0).

Publication III. Importantly, we performed a control experiment where the dye solution is separated from the array with a dielectric (PVA) spacer. By varying the spacer thickness, we find that the laser threshold cannot be reached with a 400 nm spacer layer. In indicates that the dye molecules within 400 nm layer on top of the array provide most of the gain for lasing. It implies that plasmonic near fields are important for the lasing action in nanoparticle arrays.

The operational principle of the double-pump spectroscopy is explained in Figure 5.15a-b. We measured the change in time-integrated luminescence intensity (of lasing at the band edge) as a function of time delay between the pulses. At negative time delays, Δt<0, the weak (probe) pulse arrives first, which alone cannot create a sufficient population inversion to trigger lasing. The excited state population decays slowly through spontaneous radiative and non-radiative decay channels until

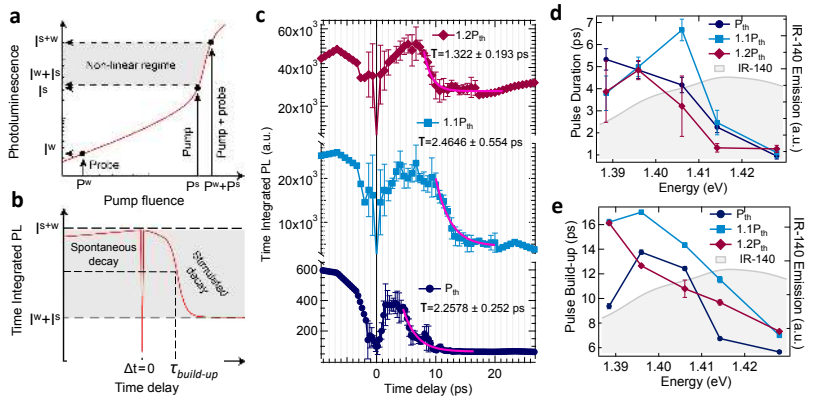

Figure 5.15. Ultrafast lasing dynamics. (a-b) Operational principle of the double-pump spectroscopy. Time-integrated photoluminescence as a function of pump fluence (a) is used to map the spontaneous emission intensity I^w, produced by the weak (probe) pulse with fluence P^w, and the stimulated emission intensities I^s, produced by the strong (pump) pulse with fluence P^s. When the pump and probe pulses excite the sample at the same time ($P^w + P^s$), the luminescence intensity takes its maximum value of I^{w+s}. When P^w and P^s are far separated in time, the intensity becomes $I^w + I^s$. (b) By displacing the probe pulse in time with respect to the pump pulse, the spontaneous and stimulated emission (lasing) lifetimes can be measured. At zero delay, $\Delta_t = 0$, a dip in the photoluminescence is observed, that is caused by less efficient pumping due to interference fringes that occur when the two pulses overlap on the sample simultaneously (see Fig. 5.13). (c) Typical time-integrated photoluminescence for P_{th}, $1.1P_{th}$ and $1.2P_{th}$ as a function of time delay of the probe pulse. Here, the nanoparticle array has a period of 570 nm and 100 nm diameter particles polarised along the x-axis. The probe fluence is kept at $0.05P_{th}$. The output pulse duration is estimated by fitting a decaying exponential function (magenta line, τ) to the tail at the positive time delays. Error bars represent the standard deviations from the average value obtained from three different measurement sets, and they underline the stability of the system. (d) Pulse duration and (e) pulse build-up time dependence on the band-edge energy location. We find shortening of both time values when the band-edge is tuned at the blue side of the IR-140 emission (shown in the background of (d-e)). The modulation speed is defined as the inverse of the summed pulse build-up and the pulse duration times. The array periods here are 565, 570, 575, 580 and 585 nm. Figure reprinted with permission from Publication III (© CC BY 4.0).

the strong pulse arrives. The strong (pump) pulse is able to increases the population inversion above the threshold value and trigger the lasing action. The slow decay of the time-integrated intensity in negative delays can be used for measuring the spontaneous decay time of the molecule, in our case 180 ps. At positive time delays, Δt >0, the strong pulse creates a population inversion that exceeds the threshold value and a lasing pulse is triggered. The weak pulse can contribute to lasing only if it arrives before the generated output pulse ends. If the weak pulse arrives too late, the molecules it excites decay through the spontaneous channels and add only a small contribution to the time-integrate luminescence signal.

Figure 5.15c-e show the main results of the dynamics study, the time-integrated laser emission at the band-edge as function of time delay. For small negative time delays (Δt<0), we see high value of time-integrated luminescence, as expected when the pump and probe powers are summed up to produce I^{s+w}. An interference-caused dip is observed at Δt=0. For positive time delays (Δt>0), the time-integrated luminescence

reaches again I^{s+w}, which is then followed by a rapid decay to $I^s + I^w$. Interestingly, the system exhibits a strong dependence of the dynamics on the band-edge location. Figure 5.15c shows the time-integrated luminescence for an array with a band-edge at 1.414 eV. As we tune the band-edge onto the blue side of the IR-140 emission, the modulation speed increases. The pulse built-up time is defined as the delay time when the integrated luminescence has dropped to half of its maximum value (in the positive side), and the pulse duration is estimated with a exponential fit to the decaying intensity. The obtained pulse build-up and pulse duration times are presented against the dye emission spectrum as the gray background in Figure 5.15d-e. Interestingly, both time constants become smaller as a function of band-edge energy (decreasing lattice period), when the lasing mode energy shifts toward the blue side of IR-140 emission spectrum.

We explain the experimental results by comparing to rate equation simulations performed with the model introduced in Section 3.3. The rate equation simulations are further explained in Figure 5.16, which shows also the results of FDTD simulations with a gain medium. An FDTD simulation of the electric field distribution in a single unit cell, showing plasmonic hot spots, is presented in Figure 5.17.

In the rate equation simulations, we take values for IR-140 lifetimes found in [212]: the radiative decay time $\tau_{21} = 5.1$ ns, the vibrational relaxation times $\tau_{32} = 0.7$ ps and $\tau_{10} = 4$ ps, and the non-radiative decay time $\tau_{20} = 240$ ps (see Fig. 5.16). We use τ_{10} and τ_{20} directly as they are because there is no particular reason why they would change in our setting. In contrast, τ_{32} may vary depending on the band-edge location that determines the lasing frequency. If the band edge shifts upward in energy, the excited electron needs to loose less energy coming down the vibrational manifold, before emitting a photon. Thus, τ_{32} could effectively become shorter. The radiative decay time is calculated based on the measured spontaneous decay time that includes the contributions of both radiative and non-radiative decay channels. The spontaneous decay time, τ_{sp}, is defined as

$$\frac{1}{\tau_{\mathrm{sp}}} = \frac{1}{\tau_{\mathrm{r}}} + \frac{1}{\tau_{\mathrm{nr}}} \Leftrightarrow \tau_{\mathrm{r}} = \frac{\tau_{\mathrm{nr}}\tau_{\mathrm{sp}}}{\tau_{\mathrm{nr}} - \tau_{\mathrm{sp}}}, \tag{5.5}$$

where $\tau_{\mathrm{r}} = \tau_{21}$ and $\tau_{\mathrm{nr}} = \tau_{20}$ are the radiative and non-radiative decay times, respectively. By assuming that the Purcell effect enhances only the radiative decay, we can take the literature value for the non-radiative decay time, $\tau_{\mathrm{nr}} = 240$ ps. With the measured spontaneous decay time, $\tau_{\mathrm{sp}} = 180$ ps, the radiative decay time now becomes $\tau_{\mathrm{r}} = 720$ ps. By comparing this to the literature value of 5.1 ns, we obtain an enhancement factor of $F = 7$. This Purcell factor can be calculated also directly:

$$\frac{1}{\tau_{\mathrm{sp}}} = \frac{F}{\tau'_{\mathrm{r}}} + \frac{1}{\tau_{\mathrm{nr}}} \Leftrightarrow F = \tau'_{\mathrm{r}}\left(\frac{1}{\tau_{\mathrm{sp}}} - \frac{1}{\tau_{\mathrm{nr}}}\right), \tag{5.6}$$

where τ'_{r} is now the intrinsic radiative lifetime.

We ignore the enhancement of non-radiative decay because Purcell effect is a resonant process [213] and we assume that the non-radiative decay process (containing one or more steps) is not in resonance with the lasing mode. In addition, fluorescence

quenching is high only very close (a few nanometers) to the metal particles [1, 20], so the fraction of quenched molecules within the total lasing mode volume is minute.

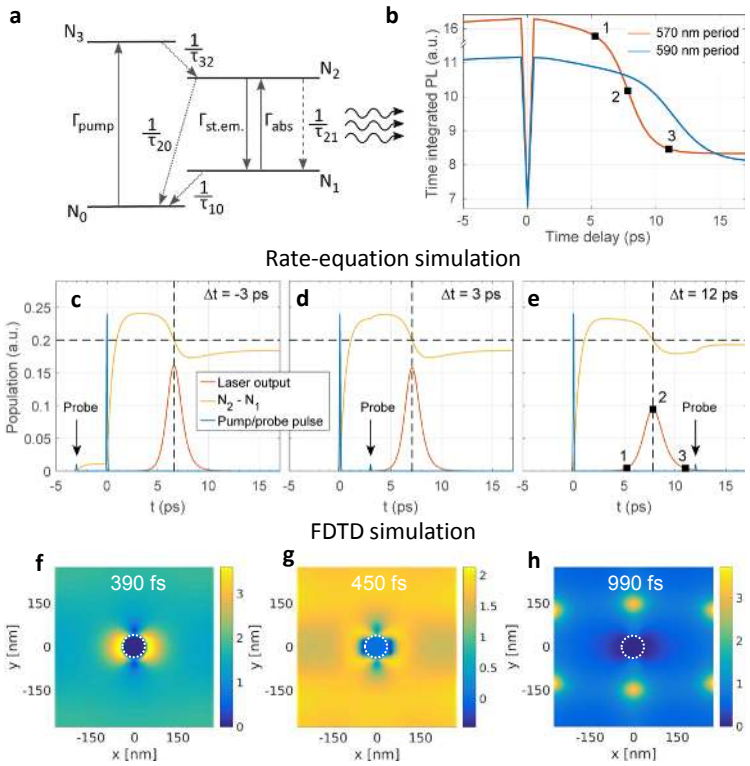

Figure 5.16. (a) Energy level diagram of the four-level gain medium (the same as introduced in Fig. 3.7). (b-e) Rate-equation simulation with two pulses (pump and probe). (b) Typical time-integrated photon population in the lasing mode, which is directly proportional to laser output that corresponds to the observed photoluminescence in the experiments. Here, the simulation is done for $1.2P_{th}$ with two different parameter choices corresponding to lattice periods of 570 and 590 nm. The dip at zero time delay is artificial and represents the dip in the experiments caused by the interference fringes. The three black squares correspond to the temporal locations marked in (e). Laser output peaks at half-maximum of the time-integrated signal, which we define as the pulse built-up time (square 2). (c-e) Population trajectories obtained by solving the rated equations with parameters corresponding to 570 nm lattice period: input pulses (blue), population inversion $N_2 - N_1$ (yellow) and the output laser pulse (red). Horizontal dashed line indicates the threshold population inversion and the dashed vertical line marks the peak in the laser output. (f-h) FDTD simulations of the population inversion over the unit cell in xy-plane for an x-polarized nanoparticle for three time frames: (f) before lasing is triggered but after the pump pulse, (g) when lasing starts, and (h) after the generate output pulse. The color scale is in units of concentration (mM). The FDTD simulation are performed with a single pump pulse. The location of the nanoparticle is marked with white circles. The difference in time scales between the rate-equation simulation and the FDTD comes mainly from a difference in the pumping level. In the FDTD simulations, the pump fluence was set to a value much higher than the threshold so that the lasing is triggered in a feasible time frame. Also the rate-equation model shows considerable acceleration of dynamics if the pump rate is increased multiple times the threshold value. The main purpose of the FDTD simulation is to map the spatial dependence of the population inversion and how it relates to the field hot-spots (see Fig. 5.17). Figure reprinted with permission from Publication III (© CC BY 4.0).

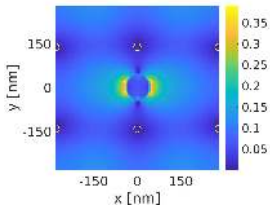

Figure 5.17. FDTD simulation of the electric field magnitude in the xy-plane of the plasmonic lattice. In the FDTD simulations for lasing dynamics, we apply a semi-classical model [37,214] where Maxwell's equations are coupled to the polarisation densities at the dye absorption and emission transition, and polarization densities are further coupled to rate equations for the four-level molecule. Here, the color scale is normalized to a field magnitude at which the system enters the strong coupling regime and the approximations behind the rate-equation model fail (see detailed definition in the supplementary material of Publication III). Values of close to 0.4 are reached at the hot spots, approaching the strong coupling condition (for a single molecule). This simulation is done with a single pump pulse and without molecules. White circles indicate the locations of the field minima that correspond to the gain maxima in Figure 5.16. Figure reprinted with permission from Publication III (© CC BY 4.0).

For the cavity lifetime, τ_{cav}, we use a measured SLR mode lifetime. Measured extinction spectra are presented in Figure 5.18, which shows that the spectral linewidth of the SLR broadens when moving toward higher energies. This is due to an increase of the plasmonic component in the SLR mode. The Q factor of the SLR mode for 590 nm and 570 nm lattice periods give $Q = 254$ and $Q = 182$, respectively. With Equation 3.2 these convert to lifetimes of $\tau_{cav} = 121$ fs and $\tau_{cav} = 84$ fs. The lasing dynamics in the rate-equation model is very sensitive to τ_{cav}, and the shorter lifetime with a shorter period (band-edge in higher energy) leads to faster built-up time and a shorter pulse duration. Smaller period may also result in smaller τ_{32} as discussed above, also accelerating the modulation speed. We simulate the lasing action with two different sets of parameters: 1) $\tau_{cav} = 121$ fs, $\tau_{32} = 700$ fs and 2) $\tau_{cav} = 84$ fs, $\tau_{32} = 577$ fs. The first set corresponds to a 590 nm period with band-edge at 1.39 eV, and the second set to 570 period with band-edge at 1.43 eV. The change of τ_{32} is proportional to the energy difference between the pump (1.55 eV) and the band edge. Faster modulation speed is obtained for the second parameter set as can be seen in Figure 5.16b.

We have performed a sensitivity analysis of different parameters in the rate-equation model and how they affect to modulation speed. The pulse duration and build-up times in the simulations depend on the interplay of mainly four parameters: β-factor, molecular lifetimes τ_{21} and τ_{32}, and cavity lifetime τ_{cav}. In Figure 5.19, we present a systematic study of the effect of these four parameters on the modulation speed. The parameter ranges are chosen as follows. Based on the typical threshold curves of our nanoparticle lasers, β is on the order of 10^{-3}, given by the non-linear jump at threshold between the two linear regimes (see Fig. 5.14). Based on the extinction spectra, the cavity lifetime varies between 80 – 120 fs. Moreover, the change of the band-edge energy (where lasing occurs), with respect to the vibrational manifold of the molecule's excited state, is estimated to change τ_{32} within 400 to 700 fs. Radiative decay τ_{21} is attributed to Purcell effect that is extracted from the decay of the time-integrated signal

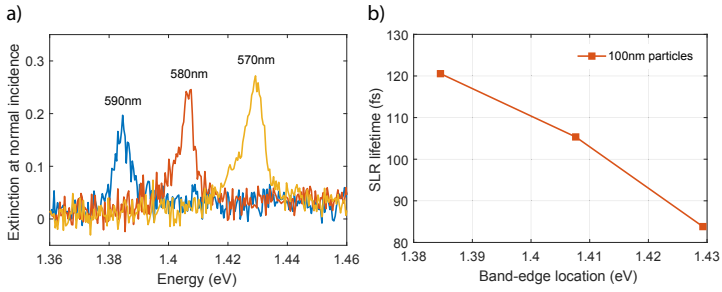

Figure 5.18. (a) Extinction spectra at normal incidence that reveal the SLR mode at the Γ-point (band-edge). The linewidths are 7.9, 6.2 and 5.5 meV, for periods 570 nm, 580 nm and 590 nm, respectively. The measured linewidth of the mode translates to the mode lifetime plotted in (b), see Equation 3.2. These lifetimes are used in the rate equation simulations as the cavity lifetime. Figure reprinted with permission from Publication III (© CC BY 4.0).

in the negative time delays. In plasmonic systems, Purcell enhancement is highly spatially dependent so τ_{21} has rather large uncertainty. However, the obtained value should be the average decay time of the molecules that participate in the lasing action. In the double-pump experiment, only the molecules located in the mode volume of the lasing mode can contribute to the time-integrated lasing signal. In other words, the emission of the molecules outside the lasing mode volume contribute to a constant background, that is not varying as a function of time delay. Finally, with the obtained value of $\tau_{21} = 720$ ps, the time-integrated photon population in the rate-equation model matches excellently to the time-integrated luminescence in the experiments.

The sensitivity analysis helps us to find out the origin of the accelerated dynamics when tuning the band-edge to the blue side of the dye emission. Based on this analysis we may conclude that the change in cavity (SLR mode) lifetime is the dominant factor, and a change of τ_{32} has a moderate contribution.

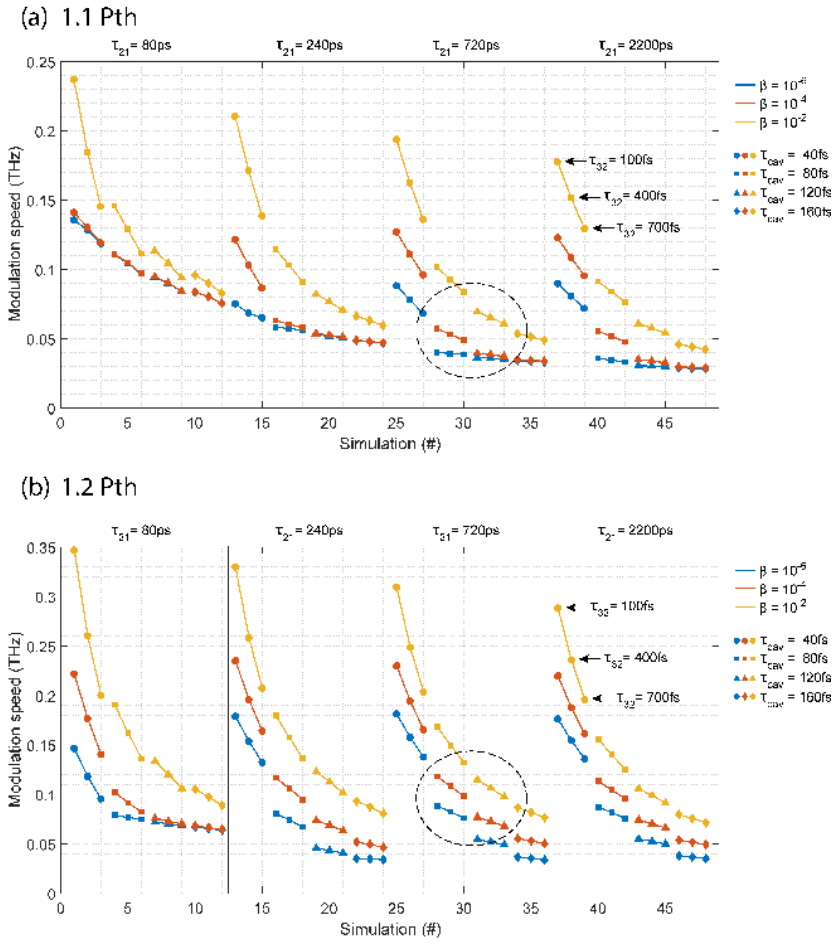

Figure 5.19. Sensitivity analysis of the simulated modulation speed with respect to the relevant simulation parameters which are: spontaneous-emission coupling factor β, and the lifetimes τ_{21}, τ_{32} and τ_{cav} (see the four-level diagram in Fig. 5.16). The simulations are performed with 144 different parameter choices, for two pump powers (a-b). The colors and symbols given on the right side specify the parameter choices. We conclude that τ_{cav} is the dominant and τ_{32} is the second-dominant parameter in determining the modulation speed, in realistic ranges of the four parameters. Based on the measured extinction data in Publication III, the cavity lifetime varies between 80 to 120 fs. The change of band-edge energy with respect to the vibrational manifold of the molecule is estimated to change τ_{32} within 400 to 700 fs. Based on the the non-linear rise at threshold in typical pump-fluence dependence curves (see Fig. 5.14), β is on the order of 10^{-3} and does not considerably vary as a function of the lattice period. Purcell effect, and thus τ_{21}, is the most difficult parameter to analyse because it has strong spatial dependence in plasmonic systems. Here, we have estimated the Purcell factor from the negative time delays of the double-pump experiment, which yields to a radiative lifetime of τ_{21} = 720 ps. We do not expect τ_{21} to considerably vary as a function of the lattice period, either. The dashed circles indicate the most relevant parts in the plot. Figure reprinted with permission from Publication III (© CC BY 4.0).

5.3 Bose-Einstein condensation in a plasmonic lattice

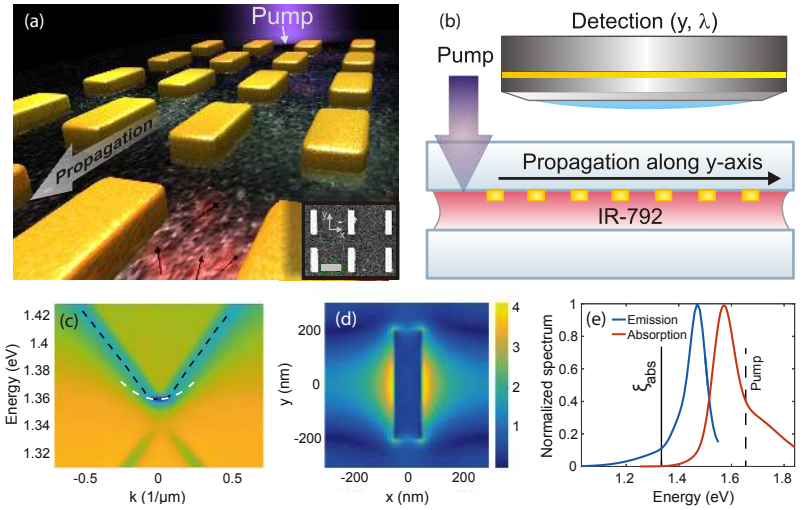

Figure 5.20. Schematic illustration of the sample, experimental configuration, and characteristics of the system. (a-b) The system consists of an array of gold nanorods overlaid with IR-792 dye molecule in solution. Scale bar in the SEM image inset is 300 nm. The size of the array is $100\times300\,\mu m^2$. (c) Dispersion $E(k_y)$ of the SLR mode in TE mode crosscut (particles are polarized along x-axis), obtained with the transmission measurement without dye molecules. Blue dashed line indicates the measured extinction maxima, the white dashed line indicates a parabola fitted to maxima around the band bottom where the SLR excitations condense. The fitted parabola is used for extracting the effective mass of the bosonic quasiparticles. (d) Absolute value of the electric field over one unit cell in the lattice plane, relative to the maximum value of the pump pulse, $|E|/|E_0$, obtained by an FDTD simulation. (e) Absorption and emission spectra for the molecule IR-792. The solid line indicates the "absorption edge", ξ_{abs}, meaning the point where absorption goes effectively to zero (absorption rate is very small compared to losses in the system). The dashed line indicates the pump photon energy. Figure reproduced with permission from Publication IV (© 2018 Springer Nature).

The SLR excitation are bosonic quasiparticles that consist of a photonic part and a plasmonic part, that is, electron plasma oscillation in individual nanoparticles. We have studied the possibility of Bose-Einstein condensation of these *lattice plasmons*, and in Publication IV we demonstrate that indeed under certain conditions, the lattice plasmons can form a condensate at room temperature. One of the most interesting aspects of the condensation experiments is the thermalization process. How can the SLR excitations thermalize and how can they thermalize fast enough compared to the SLR lifetime that is on the order of 100 fs? The key experiment that enables us to reliable observe the condensation is to monitor the spatial evolution of the luminescence spectrum along the array, while the SLR excitation propagate.

In Publication IV, we study elongated nanoparticle arrays of $100\times300\,\mu m^2$, made of gold nanorods with length of 65% of the lattice period, width of 100 nm and height of 50 nm. The arrays are overlaid with 50 mM concentration of IR-792 molecules in solution. We excite the molecules only at one end of the array and follow

the luminescence spectrum of the propagating SLR excitations along y-axis, see schematics in Figure 5.20a-b. The dispersion of the bare array is shown in Figure 5.20c where we have fitted a parabola to the band-bottom that provides the energy ground state for the excitation to condense. The fit yields a very small effective mass of about 10^{-7} electron masses (see Eq. 3.22). Figure 5.20d displays the electric field profile in one unit cell of the plasmonic lattice, without molecules, and Figure 5.20e shows the absorption and emission spectra of IR-792, with a definition of an *absorption edge*, ξ_{abs}.

5.3.1 Spatial evolution of the luminescence spectrum

We investigate three samples that are otherwise identical except that the lattice period is varied from $580-610\,\mathrm{nm}$. This way we tune the band-edge energy of the SLR dispersion above, below and matching ξ_{abs}. The luminescence spectra as a function y-axis of the lattice are presented in Figure 5.21, for three distinct cases: 1) thermalization but no condensation (Fig. 5.21a), 2) lasing (Fig. 5.21b), and 3) BEC (Fig. 5.21c). The photonic part of the excited SLR modes continuously leak out through radiative loss, and thus the observed luminescence intensity is directly proportional to the population of SLR excitations. In this experiment, we did not use the 1 mm thick dye solution chamber but rather sandwiched the solution between two glass slide, creating around $10-15\,\mu\mathrm{m}$ dye layer. We have noticed that the propagation of SLR excitation outside the pump spot, that we observe, does not occur with a very thick dye solution layer, implying that the propagation might be assisted with coupling to waveguide modes provided by the thin dye layer.

We observe a red shift along the propagation, which is attributed to a thermalizing population. By carefully tuning the band-edge energy to match ξ_{abs}, a macroscopic population accumulates at the band-edge, see Figure 5.21c,g. The BEC case is compared to a rate-equation simulation done in the time domain, which describes the interaction between optical modes and the molecules with their measured absorption and emission spectra. The simulations show that recurrent absorption and emission cycles in the molecules lead to thermalization of the photon or SLR populations. The molecules act as a *thermal bath* for photon or SLR excitations. A similar thermalization mechanism is used to explain photon condensates [157]. The rate-equation model is based on the approach in [170, 171], and elaborated in detail in the supplementary information of Publication IV. The connection from the time domain in the simulations to the spatially resolved luminescence spectra is made via the group velocity at which the SLR excitations propagate along the linear part of the dispersion. The simulation results are presented in Figure 5.21d,h.

Figure 5.22 shows the spatially resolved luminescence spectra also for intermediate lattice periods. It beautifully demonstrates how a gradual transition happens from thermalization to BEC, and to lasing, with increasing lattice period.

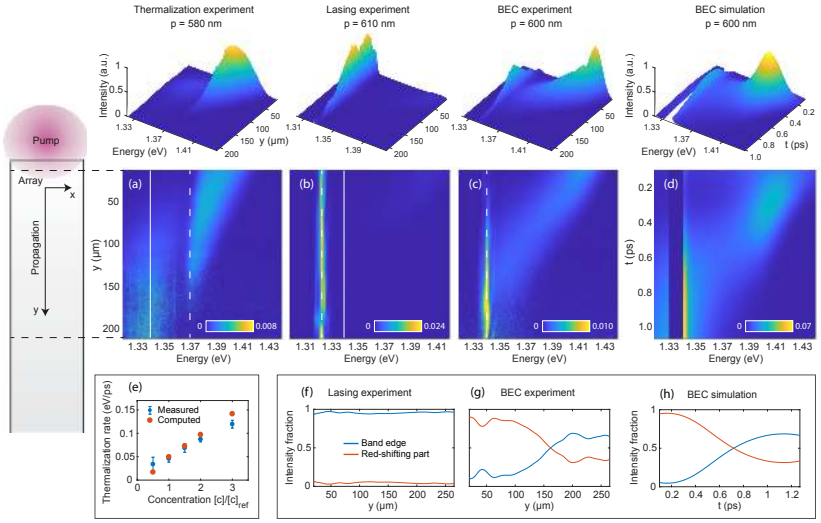

Figure 5.21. Spatially-resolved luminescence spectra showing the crossover between thermalization, lasing and condensation. (a-c) present the luminescence spectra as a function of y-axis for nanoparticle arrays having a lattice period of 580, 600, and 610 nm. The color scale corresponds to the intensity that is normalized for each row by the summed total intensity at that row. The insets on top of (a-c) show pseudo-3D plots of the same spectra as raw intensity data. The white dashed lines indicate the band-edge energy and the solid lines indicate ξ_{abs}. In (c), the two energies are overlapping so only a dashed line is drawn in the plot. (f-g) show the evolution of the population at the band edge compared to the population at the higher energies, in the lasing and BEC cases, respectively. For calculating the relative population, the intensities of the band edge (1.32–1.33 eV and 1.34–1.35 eV) and the red-shifting part (1.33–1.41 eV and 1.35–1.43 eV) are normalized by the summed total intensity between the energies of 1.32–1.41 eV and 1.34–1.43 eV, respectively. (d,h) present the rate-equation simulation results in the time domain, for parameters corresponding to the BEC case. (e) Measured and simulated thermalization rate as a function of molecule concentration. Measured data is averaged from several measurements for each concentration ($[c]_{\mathrm{ref}}$ = 50 mM), error bars show the standard deviation. For the simulation, the $[c]_{\mathrm{ref}}$ corresponds to the number of molecules used for calculating the results in (d,h). The color scales in (a-c) is saturated for better visibility of relevant features; the maximum intensity values are (a) 0.0096, (b) 0.0286, and (c) 0.0175. Figure reproduced with permission from Publication IV (© 2018 Springer Nature).

5.3.2 Macroscopic population in the ground state

We study also the angular distribution of the sample luminescence and examine the SLR population distribution as a function of pump fluence. Figure 5.23 shows the k-space spectra measured from two parts of the array, as well as the population distribution with threshold behaviour, and 2D k-space images of the condensate.

The k-space spectrum in the beginning part of the array, displayed in Figure 5.23a, shows that the thermalizing population follows one of the TE mode branches. This is due to asymmetry created by pumping only at one edge of the lattice. The propagation of SLR excitation is triggered to the $+y$ direction, away from the pump, and this direction dominates the luminescence signal. The reason why the molecules do not emit to the SLR mode propagating in the $-y$ direction may be the different electric

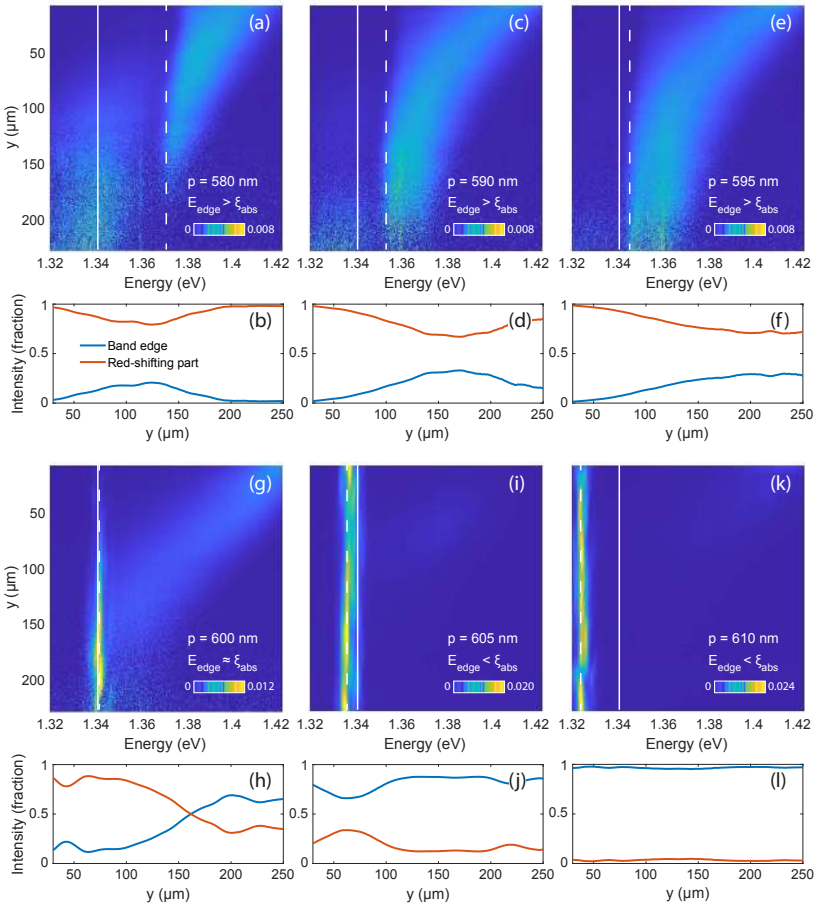

Figure 5.22. (a-l) Spatially-resolved luminescence spectra as well as the normalized populations at the band edge and at other energies (red-shifting part). The results are shown for lattice periods of 580−610 nm, including three additional intermediate cases (c.f. Fig. 5.21). We can observe a gradual evolution from the thermalization only, to BEC and to lasing, with increasing lattice period. Formation of the BEC is extremely sensitive to the periodicity, which can observed by comparing the cases $p = 595$ nm (e-f), $p = 600$ nm (g-h), and $p = 605$ nm (i-j). Only for $p = 600$ nm the band-edge population crosses the red-shifting population (macroscopic population at the band-edge emerges due to thermalizing population). For $p \geq 605$ nm the intensity at the band edge is higher already in the beginning part of the array. This is explained by lasing action that gets triggered at the edge of the array (under the pump spot) when the band-edge energy is tuned below ξ_{abs}, which effectively increases the available gain (no absorption). The excited population is stimulated directly to the band edge, without thermalization through recurrent absorption and emission cycles in the molecules, and the lasing in the SLR mode then spread over the whole array. Figure reproduced with permission from Publication IV (© 2018 Springer Nature).

field distribution around the nanoparticles for the counter propagating modes. The thermalization may also involve stimulated processes.

The k-space spectrum, recorded at y-position where the BEC occurs, is displayed in Figure 5.23b. The k-space spectrum is measured as a function of pump fluence, and the population distribution integrated over the in-plane wave vector k are shown in

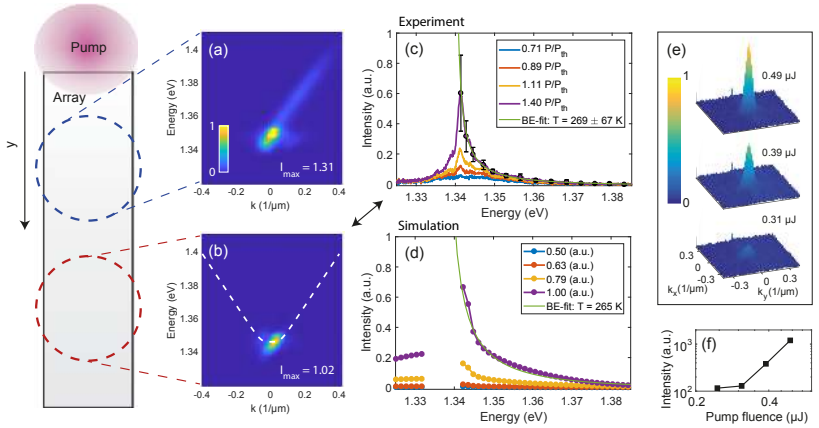

Figure 5.23. Angle-resolved (k-)space spectra at different locations of the array, and an accumulation of macroscopic population to the band-edge. (a-b) k-space spectrum recorded from the location indicated by the blue circle (a) and red circle (b). The dashed line in (b) depicts the fit to the SLR dispersion without the dye molecules (Fig. 5.20c). We observe that the thermalizing population indeed follows the SLR dispersion in (a), and further away from the pump spot, the population has condensed to the band edge (b). Note that the asymmetry in the spectra is because we pump the array only at one end, and the propagation of SLR excitations is therefore triggered only in one direction (away from the pump). (c) The population distribution as a function of energy for different pump fluences, obtained by integrating the intensity over k in the spectra recorded at the red circle. (d) computed distributions at the time when the thermalization is completed. Bose–Einstein distribution fits are shown with green lines. The ratios between the consecutive pump fluencies in the simulation are the same as in the experiments. The experimental data fits well to the Bose–Einstein distribution close to room temperature, $T = 269 \pm 67$ K (95 % confidence bounds). The error bars display the standard deviation for ten measurements. (e) 2D k-space images that correspond to the three highest pump fluences in (c), showing emergence of the condensate and its confinement in both k_x and k_y. f) Luminescence intensity at the band edge as a function of pump fluence that displays a threshold behaviour. Figure reproduced with permission from Publication IV (© 2018 Springer Nature).

Figure 5.23c. The population at the band edge greatly dominates the luminescence intensity but a thermal tail can be observed at higher energies. Bose-Einstein distribution function is fitted to the measured distribution, above the threshold, and the fit gives a temperature of 269 ± 67 K. Also the rate equation simulation shows similar threshold behaviour with Bose-Einstein distribution above the threshold pump fluence, see Figure 5.23d. The BEC is confined in both directions in the 2D k space, see Figure 5.23e, implying 2D nature of the condensate. In two-dimensional systems, Bose-Einstein condensation is possible only in a finite-sized system [215]. Our system is clearly finite-sized, as spatial coherence can easily extend over a 100 μm sized array, as has been observed in the lasing studies in Publications II-III.

5.3.3 Spatial coherence

The spatial coherence in the BEC and lasing cases are measured with a Michelson interferometer by selecting only the energies near the band edge by a spectral band-pass filter. Figure 5.24a-e presents a comparison of these two cases, the images are

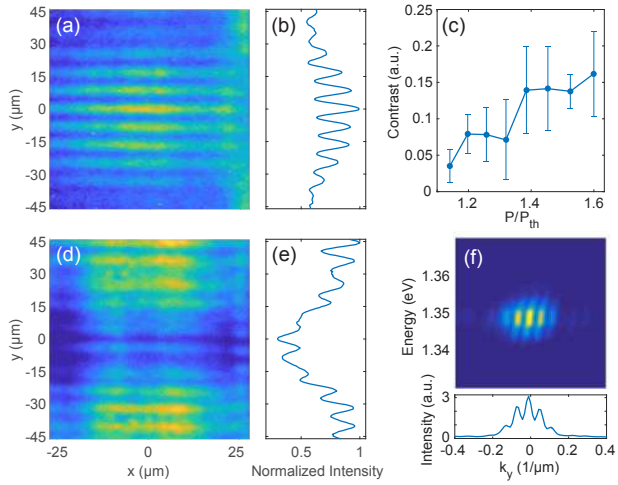

Figure 5.24. Spatial coherence measurements in the BEC and lasing cases. Michelson interferometer images are obtained by overlapping two real space images, one inverted with respect to $y = 0$, at the camera pixel array. (a) shows the interfered image for the BEC case taken at the location where the condensate occurs. (b) shows the intensity profile integrated along the x-direction in (a). The interference fringes evidence that the condensate is spatially coherent over a distance of at least 90 μm. (c) Contrast of the interference fringes as a function of pump fluence. The error bars show standard deviation for two sets of measurements. (d-e) show the interfered image and the intensity profile for the lasing case, for comparison. Also in the lasing case the spatial coherence clearly extends over 90 μm but the intensity profile, particularly the envelope of the interference pattern, looks very different compared to the BEC case. For the BEC, the coherent population originates from the thermalization upon propagation. The center ($y = 0$) of the Michelson interferometer image is set to the array location where the coherent population maximizes, producing a maximum of the envelope to the center (b). In contrast, for lasing the intensity maximizes at the edge of the array (under the pump spot) and decays as a function of distance from the edge. As the center of the Michelson interferometer image is set to the same array location as in the BEC case, inverting $-y$ and $+y$ positions of one of the images produces a minimum of the intensity envelope to the center (e). Finally, (f) presents a complementary measurement of the spatial coherence in the BEC case. A double slit with a distance of 90 μm is inserted to the first image plane of the sample and then we measure the k-space spectrum (this corresponds to Fig. 5.23b). A strong interference pattern is visible indicating spatial coherence between light going through the two slits. The experiment confirms that the spatial coherence extends to at least 90 μm distance. Figure adapted with permission from Publication IV (© 2018 Springer Nature).

recorded at the y position where the BEC occurs. We can conclude that in both cases the spatial coherence extends to at least 90 μm. However, there is a distinct difference between the two. In the BEC case, the intensity and also the fringe contrast clearly maximize at the center, whereas in the lasing case, the intensity minimizes but the fringe contrast stays more or less constant over the image. It indicates that the spatial coherence really emerges at the location where the BEC occurs, whereas the lasing is coherent over the whole array but its intensity is exponentially decaying as a function of distance from the pump spot. Figure 5.24f shows a complementary measurement of the spatial coherence by replacing the iris in the first image plane with a double slit and recording the k-space spectrum. The double-slit experiment confirms that the spatial coherence extends to at least 90 μm.

5.4 Bose-Einstein condensation of strongly coupled lattice plasmons

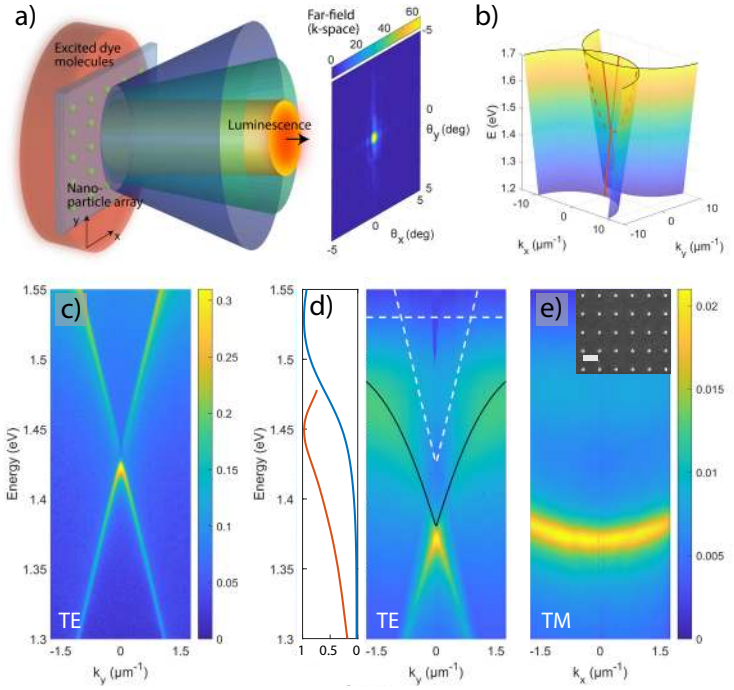

Figure 5.25. (a) Artistic illustration of the experimental configuration. (b) Light cones for the diffracted orders (0,-1) and (0,+1) that emerge from radiative coupling of x-polarized nanoparticles. Crosscut along k_y, at $k_x = 0$, is the TE mode (red solid lines) and along k_x, at $k_y = 0$, the TM mode (red dashed line). The SLR dispersions in the TE and TM mode directions are experimentally obtained by (c) the transmission measurement without dye molecules or (d-e) the reflection measurement with 80 mM solution of IR-792. In (d), the SLR dispersion exhibits a clear red-shift with respect to its original position, and an avoided crossing with the absorption line of the molecule. The absorption line and original position of the uncoupled SLR mode are depicted with white dashed lines and the lower-polariton branch given by a two-coupled-modes-model fit is indicated with a black solid line. Measured absorption and emission spectra of IR-792 are shown in the left panel with the blue and red curves, respectively. A zoomed-in SEM image of the nanoparticle array is shown as an inset in (e), the scale bar is 500 nm.

In Publication V, we study square nanoparticle arrays of different sizes. In contrast to samples in Publication IV, here the arrays consist of cylindrical gold nanoparticles with a measured diameter of 100 nm and height of 50 nm. The arrays are overlaid with IR-792 molecules in 80 mM solution inside the 1 mm thick chamber. The optimal lattice periods for condensation experiment are p_y = 570 and p_x = 620 nm, and the optimal lattice size is $100\times100\,\mu m^2$. In reference measurements, p_y is varied between 520 and 590 nm and the lattice size between 40×40 and $200\times200\,\mu m^2$. An asymmetric lattice periodicity separates the diffracted orders in the energy spectrum for the two orthogonal polarizations (e_x and e_y), and the SLR dispersions are separated accordingly simplifying the measured spectra. For x-polarized nanoparticles (as in

this experiment), the TE and TM modes correspond to combinations of ($\mathbf{e}_x, k_y$) and $\mathbf{e}_x, k_x$), respectively. Under optical excitation, the SLR mode that is mainly excited can be determined by the pump polarization because the molecules are excited more efficiently via the LSPR hot-spots of each nanoparticle [98]. In the experiment with different lattice periods, p_x is kept always 50 nm larger than p_y. In the experiment of different lattice sizes, however, the period in x and y directions is the same ($p_x = p_y = 570$ nm). We find that asymmetric periodicity plays no crucial role in the occurrence of the Bose-Einstein condensation but it only simplifies the data analysis of the experimental results.

Figure 5.25 presents a schematic of the experiment and characterization of the SLR modes without and with the dye molecules on top. The molecules are excited with a pump spot larger than the array, so there are excited molecules (and gain) at every point of the lattice. Again we follow the spatial evolution of the photoluminescence spectrum and observe a predominant red-shift of the population from the edges toward the center of the array. In contrast to the experiments in Publication IV, the spatially-resolved spectra cannot be mapped to time evolution directly as the molecules can start to emit at every point of the lattice.

The SLR dispersion in the bare plasmonic lattice is obtained with a similar transmittance experiment as before, see Equation 5.1.1. However, as the molecule layer is now so thick (1 mm), the transmission experiment cannot be used with the molecules due to ~100% absorption of the layer. The dispersions with a molecule layer are measured in reflection, where the resonant modes show up as reflectance maxima due to enhanced scattering. The reflectance is obtained by

$$R = \frac{I_{\text{array}} - I_{\text{glass}}}{I_{\text{ref}} - I_{\text{glass}}} \tag{5.7}$$

where I_{array} is a reflection from the array, I_{glass} that from the glass substrate out side the array, and I_{ref} is a reflection from a 50 nm gold film deposited onto the substrate for this purpose.

The measured dispersions show that in the presence of the dye molecules the SLR dispersion shifts downward in energy, with respect to the initial SLR position and the uncoupled diffracted orders, see Figure 5.25c-e. Moreover, the TE mode begins to bend when approaching the IR-792 absorption line at 1.53 eV. These observations indicate strong coupling between the SLR mode and molecular excitations. A coupled modes fit to the reflection maxima in Figure 5.25d gives a Rabi splitting of 164 meV, which is larger than the average linewidth of the molecule absorption spectrum (150 meV) and the SLR (10 meV). From the fit, we obtain a molecular exciton part of 23% at $k = 0$. In the following, the strongly-coupled hybrids of SLR mode excitations and molecular excitons are simply referred to as polaritons.

The sample is excited with x-polarized laser pulses having a measured pulse duration of 50 fs. Excited polariton modes continuously leak out from the system through radiative loss, and thus the observed luminescence intensity is directly proportional to the polariton population. The spectral response of the measurement setup has been calibrated with a halogen lamp with a known relative spectrum. We use a spectrometer

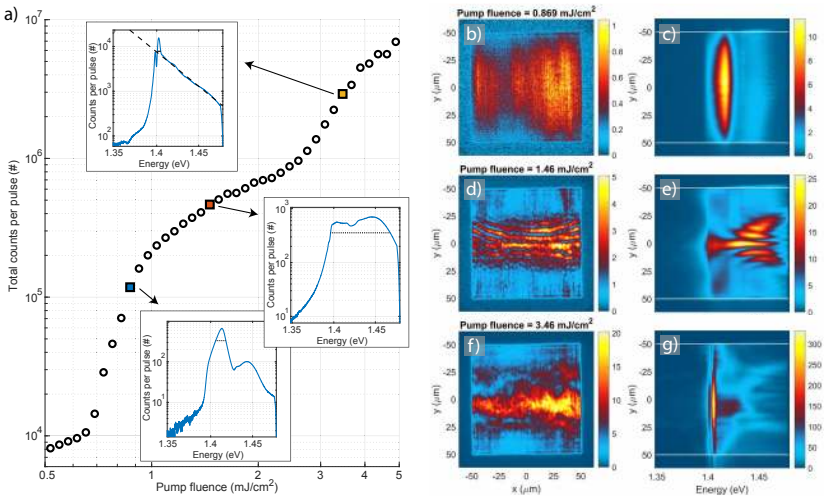

Figure 5.26. Luminescence intensity, real space images and spectra as a function of pump fluence. (a) Pump fluence dependence of the total luminescence intensity showing an intriguing double-threshold behaviour. Insets present the line spectra obtained by integrating over the y-direction in the real space spectra (between white lines). FWHM of the spectral peaks is marked in the insets with dotted black lines, and they are 12 meV, 72 meV and 4.0 meV with increasing pump fluence. The dashed line in the top inset is a fit to the Maxwell–Boltzmann distribution that gives a temperature of 333±12 K (95% confidence bounds). (b-g) Left column: Real space images of the plasmonic lattice. Right column: Spatially-resolved luminescence spectra as a function of y-position on the array. The pump fluences are (b-c) 0.87 mJ/cm^2, (d-e) 1.5 mJ/cm^2, (f-g) 3.5 mJ/cm^2. The wavy interference pattern in (d-e) arise from standing waves related to the momentum of the counter-propagating modes. The real space images are recorded for single pump pulses but the corresponding spectra are summed over 500 (c,e) and 70 pulses (g).

slit width of 500 µm, which corresponds to ±1.3° around $\theta_x = 0$, or to ±0.16 µm^{-1} around $k_x = 0$ at $E = 1.4$ eV. Respectively in the real space, it corresponds to 27 µm slice of the array at $x = 0$. Given by the excess of dye molecules and natural circulation of the fluid, there are always fresh molecules available for each excitation pulse (at 1 kHz repetition rate), which makes the samples extremely robust.

The luminescence intensity of the plasmonic lattice is plotted as a function of pump fluence in Figure 5.26a, which reveals two non-linear thresholds and a linear intermediate regime in between. Figure 5.26b-g shows the 2D real space images and spatially resolved resolved spectra with the pump fluences indicated in Figure 5.26a. The line spectra are obtained by integrating the real space spectra along the y-axis, which represent the polariton population as a function of energy. Figure 5.27 shows the 2D k-space images and k-space spectra both along k_x (TM mode) and along k_y (TM mode), for the same pump fluences as in Figure 5.26. The intensity distributions in the real and k-space and the corresponding spectra reveal three distinct regimes with increasing pump fluence: 1) one dimensional lasing, 2) intermediate regime with incomplete thermalization, and 3) Bose-Einstein condensation. Strikingly, a thermalized population is visible in the time-integrated signal meaning that most of the excitations have undergone complete thermalization process before they leak out

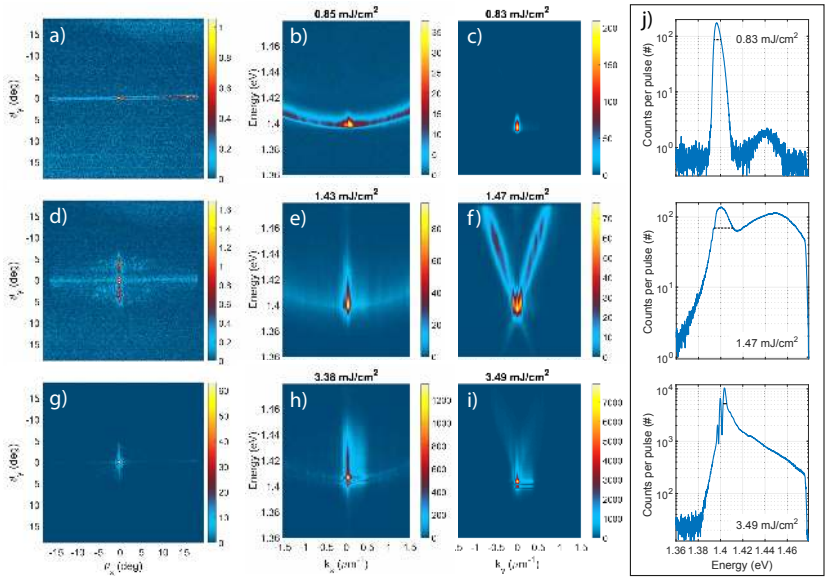

Figure 5.27. Momentum (k-)space images and spectra as a function of pump fluence. First column: 2D k-space images. Second and third column: k-space spectrum in the TM and TE mode crosscuts, horizontal and vertical slices of the 2D k-space spectrum, respectively. The pump fluences correspond to the ones in Figure 5.26. The horizontal stretching of the luminescence peaks in (h-i) is CCD blooming artifact due to intensity near the saturation limit. (j) Population distribution in the TE mode crosscuts, integrated from (c,f,i) along k_y. FWHMs are indicated with dotted black lines, and are 6.3 meV, 17 meV and 3.3 meV with increasing pump fluence.

from the system. This implies that thermalization occurs in a timescale of the SLR mode lifetime, which is on the order of 100 fs.

Let us discuss the observations with the help of Figures 5.26 and 5.27:

1) At the first threshold, $P \approx 0.85$ mJ/cm^2, we can observe one-dimensional lasing that spreads in the TM mode to large angles (Fig. 5.27a-c), in the real space the luminescence is relatively uniform with characteristic vertical stripes for lasing (Fig. 5.26b-c).

2) Increasing the pump fluence beyond the first threshold, $P \approx 1.5$ mJ/cm^2, the luminescence occurs mostly in the TE mode (Fig. 5.27d-f), and the center part of the array becomes brighter compared to the top and bottom parts (Fig. 5.26d-e). Moreover luminescence shows a red shift from the edges toward the center of the array, which we interpret as a signature of thermalizing population of polaritons that propagate along the array in $+y$ and $-y$ directions. The curious wavy pattern in the center part arises from interference of counter propagating polariton modes. From the real-space spectrum (Fig. 5.26e), one can observe that the period of the intensity oscillation actually changes as a function of energy. We find out that the wavelength of the oscillations can be mapped to the in-plane wave-vector k_y of the TE mode at the corresponding energy (Fig. 5.27f). The wavelength in real space follows a relation $\lambda_{RS}(E) = \pi/k(E)$.

3) At the second threshold, $P \approx 3.5$ mJ/cm^2, a BEC emerges. We observe 2D confinement in the k-space (Fig. 5.27g-i), in contrast to the lasing regime where confinement is observed only in k_y. The real space image shows uniform luminescence in the central part of the array (Fig. 5.26f), and the line spectrum (Fig. 5.26a, top inset) displays a narrow peak at the band edge energy and a long thermalized tail at higher energies. We fit the tail to the Maxwell–Boltzmann distribution (dashed line) and obtain a temperature of 333±12 K. Intriguingly, we see multiple modes highly occupied around the band edge, which are better visible in the k-space spectrum at $k_y = 0$ (Fig. 5.27i-j). We have checked that they do not arise from a trivial Fabry–Pérot interference as their spacing in energy is not constant. The spacing also does not depend on the lattice period or size. Based on a T-matrix simulation, these peaks are attributed to actual lattice modes that can become non-degenerate due to the finite size of the nanoparticles (details of the T-matrix simulation can be found in the supplementary material of Publication V). The FWHM of the highest peak is 3.3 meV, significantly narrower than the 10 meV linewidth of the bare SLR mode in this sample.

The lasing and condensation occur at energies 1.397 and 1.403 eV, respectively. These are lower than the band edge energy of the plasmonic lattice without molecules, 1.423 eV, but blue-shifted from the lower polariton energy 1.373 eV (band edge in reflection) or 1.382 eV (fitted lower polariton branch; see Fig. 5.25d). Since the entire dispersion gradually blue shifts as a function of pump fluence, it may be attributed to degradation of strong coupling instead of polariton-polariton interactions, for instance. Based on the band-edge locations (1.423 – 1.403) eV / (1.423 – 1.373) eV, the coupling in the condensation regime has decreased to ~40% of the coupling in the case without pumping. It must be noted that the observed double-threshold behaviour is different from semiconductor microcavities, where the polariton condensation has a lower threshold than photonic lasing associated with loss of strong coupling [132, 216].

Figure 5.26a shows the total spectrometer counts per output pulse emitted by the system. For the BEC pulse at the second threshold, we obtain $3 \cdot 10^6$ total counts which correspond to a photon number of $\sim 10^9$, see Equation 4.10. This is roughly 10^5 times more than obtained for the BEC in Publication IV. Such an upgrade is essential for future fundamental studies and possible applications of this type of condensate.

5.4.1 Spatial coherence

We measure the spatial coherence of the sample as a function of pump fluence, with the same Michelson interferometer setup employed in Publication IV. However, now the spatial coherence is measured along both x and y axis of the lattice, with two separate measurements. The setup always inverts one of the images in vertical direction, with respect to $y = 0$ in the laboratory reference frame. To obtain the coherence between position $-x$ and $+x$, the image needs to be inverted with respect to $x = 0$. For this, instead of rotating the setup, we rotate the sample (the lattice) and pump polarization by 90°, so that the pumping condition stays the same with respect to the sample. The fringe contrast in the interfered images, and reference images, is show in Figure 5.28. A reference image is a normal real space image, summed with the same image that is

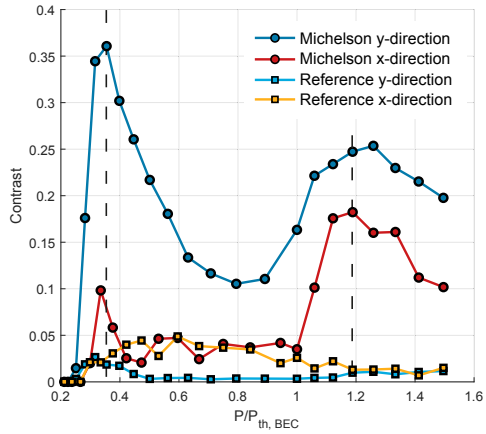

Figure 5.28. Measured spatial coherence along y and x directions of the plasmonic lattice. Fringe contrast in the region of interest (see white boxes in Fig. 5.29) as a function of pump fluence. For reference, we extract the contrast also from the incoherently summed real space images.

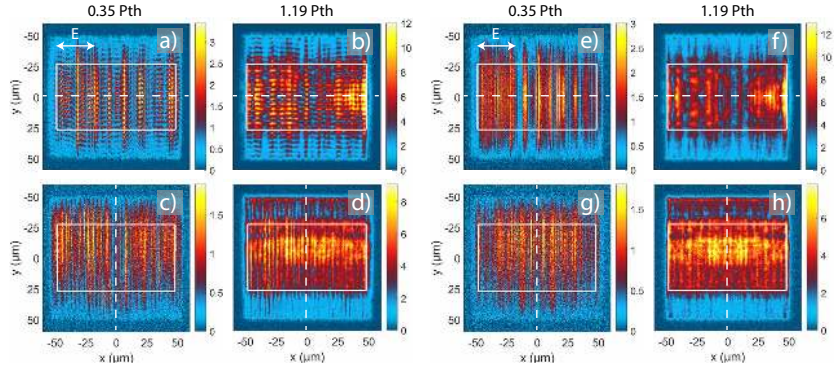

Figure 5.29. Real space images recorded with the Michelson interferometer, and incoherently summed reference images. (a-d) Interfered real space images. To obtain the spatial coherence between $-y$ and $+y$ positions (a-b) or $-x$ and $+x$ positions (c-d), one of the images is inverted with respect to the white dashed line in the Michelson interferometer. The images are shown for pump fluences that correspond to the lasing and condensation regimes (see dashed lines in Fig. 5.28). (e-h) Reference images that are obtained by inverting a real space image from one Michelson interferometer arms, in the post processing, and summing it with the original non-inverted image. This makes the average intensity similar as in the interfered images but as the images are not summed coherently in the measurement setup, no fringes due to spatial coherence arise. We observe a clear difference between the interfered and incoherently summed images when the images are flipped in the y-direction (a,b,e,f) but not so clear difference when the images are flipped in the x-direction (c,d,g,h). For the latter, Fourier analysis of spatial frequencies is a powerful tool for extracting the fringe contrast caused by the spatial coherence of the electric fields on the sample. As in Figure 5.28, P_{th} refers to the threshold pump fluence for the BEC, **E** indicates the pump polarization. All real space images are recorded for single pump pulses.

inverted in post processing stage. Figure 5.29 presents examples of the interfered and references images.

The three distinct regimes are observed also in the measured spatial coherence. High

spatial coherence occurs in both the lasing and condensation regimes, along the y-axis of the lattice. At the intermediate regime, the spatial coherence decreases, as the thermalizing population dominates the photoluminescence signal. Along the x-axis, spatial coherence is lower than along the y-axis, over the whole pump range. However, the BEC clearly exhibits high spatial coherence also along the x-axis, contrary to lasing. This measurement is consistent with the observations from the 2D k-space images (Fig. 5.27), where 1) lasing exhibits confined luminescence along k_y (the direction of feedback) but spreads along k_x, 3) condensation shows 2D k-space confinement.

5.4.2 Stimulated thermalization

At the intermediate regime, we observe red shift of photoluminescence as a function of distance along y-axis (Fig. 5.26f). The traces of the red shift start from the IR-792 emission maximum (~1.46 eV), at a certain distance from the array edges, and reach the band edge energy (~1.40 eV) at the center of the $100\times100\,\mu m^2$ array. To study the red shift, we acquire real space images and spectra for different lattice sizes at an intermediate pump fluence that is sufficient to trigger the thermalization process, see Figure 5.30a-f. On the large $150\times150\,\mu m^2$ array (Fig. 5.30e-f), we observe the traces of the red shift toward the center of the array, similarly to those in the $100\times100\,\mu m^2$ array (Fig. 5.26e). However, the red-shifting populations do not merge at the center of the array. On the small $40\times40\,\mu m^2$ array (Fig. 5.30a-b), the situation looks different as the red shift seems to occur from the center toward the edges. However, a careful comparison of the distance between the array edge and the location where the red shift starts reveals that, for the given pump fluence, the distance is the same for all arrays ($\sim 25\,\mu m$). The compared distance is indicated in Figure 5.30a,c,e.

Why the red-shift starts at a certain distance from the array edges? We explain this by a stimulated emission pulse build-up time in a gain-switched system. A four-level rate-equation simulation is performed to study the pulse built-up time as a function of pump fluence with realistic system parameters. We use transition lifetimes of $\tau_{32} = \tau_{10} = 50$ fs and $\tau_{21} = \tau_{20} = 500$ ps for the dye molecule. The β–factor is set to 0.001, the cavity lifetime to $\tau_{cav} = 100$ fs, and the system is excited with a 50 fs pump pulse. The pulse-built up time is defined here as the time between the maximum of population inversion and the maximum of the output pulse, indicated in Figure 5.30g. In the experiments, the pump pulse excites the molecules, and when the first spontaneous photons populate the modes, the polaritons begin to propagate along the lattice with a finite momentum given by the dispersion. The polariton modes gather gain while they propagate, and their intensity peaks after travelling a certain distance along the array, after which the intensity starts to decay. This distance is seen as *dark zones* at the edges of the array, and it relates to the pulse build-up time. By summing up such spatial intensity profiles starting at every point along the lattice, see Figure 5.30h, we can reconstruct the real space intensity distributions (insets in Fig. 5.30a,c,e). The dark zones appear because of the finite lattice size. The edges do not receive propagating excitations from outside the array, so the intensity at the edges is approximately half of the intensity at the central part. On the small $40\times40\,\mu m^2$ array, intensity at the edges is

similar to that of the larger arrays but in the center it is only half of that. Moreover, one can observe that the wavy interference patterns at the central part indeed only appear for arrays larger than $40\times40\,\mu m^2$, as there must be counter-propagating modes with high enough polariton population to see the interference. The propagating modes can be thought as amplified spontaneous emission pulses that red-shift (thermalize) along the propagation. They dominate the luminescence signal at the intermediate regime, and they are less coherent than the modes in the lasing or condensation regimes, which is observed in the spatial coherence measurement.

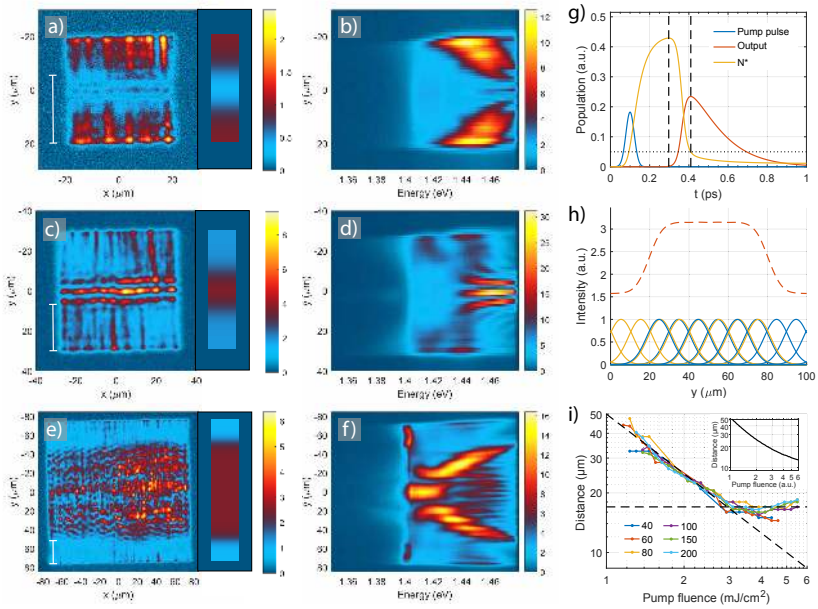

Figure 5.30. Observation of stimulated emission pulse build-up along the y-axis of the finite-sized lattices. a)-f) Real space images (left) and spectra (middle) at an intermediate pump fluence of 2.2 mJ/cm^2 for lattice sizes (a-b) $40\times40\,\mu m^2$, (c-d) $60\times60\,\mu m^2$, (e-f) $150\times150\,\mu m^2$. (g) Rate-equation simulation of the stimulated emission pulse built-up in the four-level model. The pulse build-up time is defined here as the interval between the peaks of the population inversion N^* and the output pulse (marked by vertical dashed lines). Horizontal dotted line indicates the threshold value for N^* in the simulation. (h) An illustrative plot of the sum (red dashed line) of Gaussian intensity profiles that represent the thermalizing stimulated emission pulses starting everywhere along the y-axis of the lattice and propagating in $+y$ (blue) and $-y$ (yellow) directions. Insets in (a,c,e) show the results of such sum for the corresponding lattice sizes, with the same false color as the real space images. (i) Measured distance between the array edge and the location where the red-shift starts (indicated by white lines in (a,c,e)) as a function of pump fluence for six different lattice sizes (40×40, 60×60, 80×80, 100×100, 150×150, $200\times200\,\mu m^2$). The diagonal dashed line is the inverse pump fluence ($50/P$), and the horizontal dashed line indicates the value to which the distance or the width of the dark zones saturate (~18 μm). The inset shows the simulated pulse build-up time that is converted to distance by multiplying with the group velocity of the SLR mode.

We find that the width of the dark zones depends on the pump fluence as predicted by the rate-equation simulation and the theory of Q-switched (or gain-switched) lasers [37], namely the build-up time is inversely proportional to the pump fluence. Figure 5.30i shows that the dark-zone width follows the inverse of the pump fluence,

until it saturates to a value below 20 µm (~100 fs) at around 3 mJ/cm^2. The inset in Figure 5.30i shows the pulse build-up time extracted from the rate-equation simulation, and beautifully, it displays a similar ~1/P dependence as the experiments. We attribute the red shift to a stimulated thermalization process which, at the intermediate pump fluences, does not result in a thermal distribution because the population decays too quickly. For higher fluences, when there is enough gain in the system, a non-equilibrium Bose-Einstein condensate can emerge.

5.4.3 Dependence on pump pulse duration

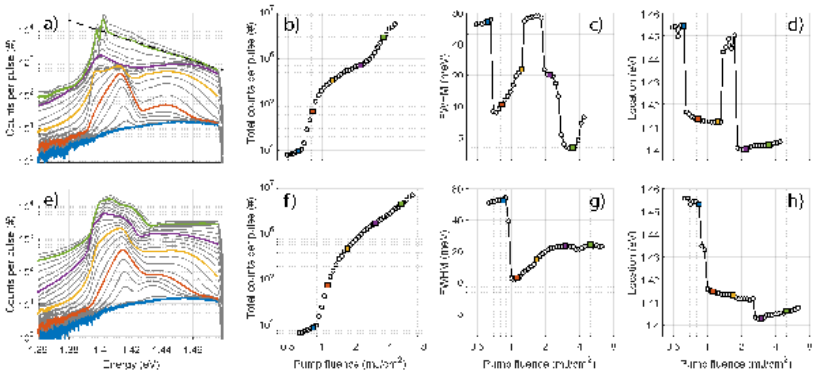

Figure 5.31. Photoluminescence as a function of pump fluence for 50 fs (a-d) and 500 fs (e-h) pump pulse durations. First column: Distribution of the polariton population as a function of energy, at different pump fluences, obtained from real space spectra. Second column: Pump fluence dependence of the total luminescence, that is, the summed counts under the curves in (a,e). Third and fourth columns: The FWHM and the energy position of the spectral maximum. Pump fluences indicated by the coloured markers in (b-d,f-h) correspond to the coloured lines in (a,e). A 50 fs pump pulse produces the double threshold behaviour with distinct regimes of lasing, incomplete thermalization, and BEC. Before the onset of lasing (blue), the distribution reflects the spontaneous emission profile of IR-792. When the lasing threshold is reached (red), a peak appears at the band edge energy. After the lasing threshold (yellow and purple), population at a broad range of higher energies is increased because of the incomplete thermalization (intermediate regime). Condensation takes place at the second threshold (green) where multiple narrow peaks emerge around the band edge. A prominent thermalized tail is observed at the higher energies, and a fit to the Maxwell–Boltzmann distribution (dashed line in (a)) gives the temperature of 333±12 K. Outstandingly, the BEC occurs only with the 50 fs pump pulse, and no second threshold is observed with the 500 fs pump pulse.

Besides the spatial measurements, that give an indirect access to look into the dynamics of the system, we perform the photoluminescence measurements as a function of pump pulse duration. The pump fluence is kept constant when changing the pulse duration so that the system is given the same total amount of energy per pulse. The pulse duration is adjusted by tuning the stretcher-compressor of Astrella. And the pulse duration is measured at the location where the sample is placed in the optical setup. Figure 5.31 shows a comparison with a pulse duration of 50 fs and 500 fs. A 50 fs pump pulse results in the double threshold behaviour that is imprinted also in the curves of FWHM and location of the spectral maximum. Remarkably, a 500 fs pulse results in only one (lasing) threshold. The system does not exhibit condensation even

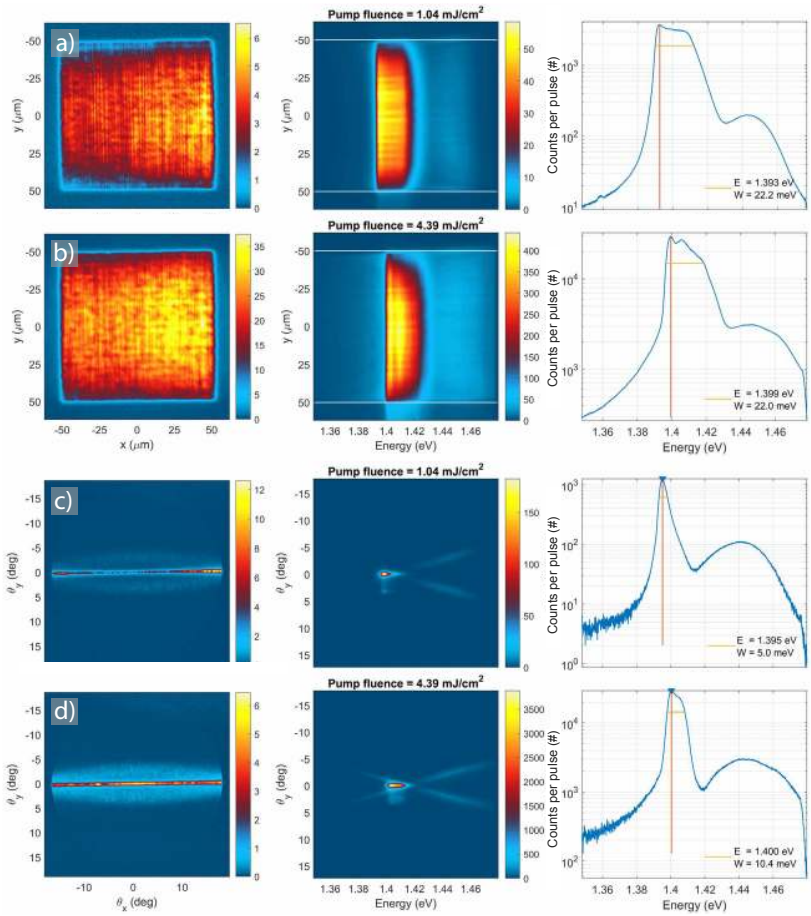

Figure 5.32. Real space and k-space measurement with a 500 fs pump pulse for a low (a,c) and a high (b,d) pump fluence. (a-b) Real space images and spectra. The line spectra are integrated over the y-axis between the white lines in the real space spectra. (c-d) 2D k-space images, and k-space spectra along the TE mode direction. The line spectra are integrated over the full range of θ_y in the TE mode spectra. With the 500 fs pump pulse, we can observe only the lasing regime where a relatively narrow peak occurs at the band edge with some luminescence in the TE mode also at lower and higher energies. The intensity distribution in the real space is uniform with narrow vertical stripes characteristic for 1D lasing. Moreover, the luminescence is spread broadly in the TM mode, which is visible in the 2D k-space images. The intensity distributions and spectra remain very similar from low to high pump fluences. There is no sign of thermalizing population nor condensation.

at higher pump fluences. Figure 5.32 presents the real space and k-space intensity distributions and spectra for the 500 fs pulse. They remain strikingly unchanged from low to high pump fluence. The intensity distributions and spectra resemble the lasing regime that occurs for the 50 fs pulse at the low pump fluence (Fig. 5.26b-c). The intermediate and condensation regimes are absent. Besides the luminescence intensity, the different threshold behaviour is clearly visible in the FWHM curves, see Figure 5.31c,g. The FWHM is significantly decreased for both pulse durations at the

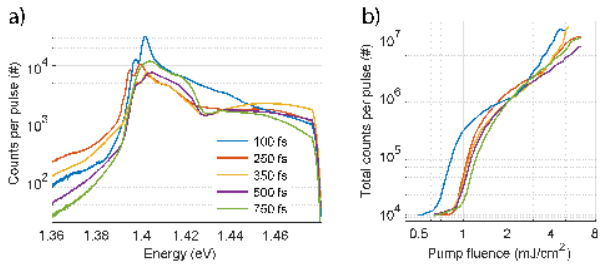

Figure 5.33. Population distribution, and total luminescence intensity as a function of pump fluence, for different pump pulse durations. (a) Polariton population as a function of energy at a pump fluence of 3.5 mJ/cm^2 (BEC threshold). Thermalized distribution with prominent peaks around the band edge energy occur only with the 100 fs pump pulse, and not with longer pulses. The line spectrum for the 100 fs pulse (blue solid line) is similar to the one measured with the 50 fs pulse. (b) Total luminescence intensity as a function of pump fluence. The lasing threshold slightly increases with increasing pump pulse duration, whereas the condensation threshold is clearly visible only with the 100 fs pulse.

first (lasing) threshold, but the FWHM is decreased even further, only with the 50 fs pulse, at the second (condensation) threshold.

Figure 5.33 shows the population distributions (at the BEC threshold), and the pump fluence dependence, for several intermediate pulse durations. We conclude that the critical pulse duration for condensate formation is around 100−250 fs. For a 250 fs pulse duration, some peak narrowing occurs at the band edge but the thermalization in the time-integrated signal remains incomplete (too much population in the higher energy states). Interestingly, the critical pulse duration is similar or smaller than the time it takes for the polaritons to propagate from the edges to the center of a $100\times100\,\mu m^2$ array. The propagation time is of the order 250 fs. Therefore, if the pump pulse is longer that that, molecules may be brought to the excited state also during the thermalization process, which can distort the process. It seems that with the longest excitation pulses (>350 fs) the instantaneous population inversion does not reach a high enough value to even start the stimulated thermalization (c.f. Fig. 5.32), as it competes from the gain with the lasing that is already triggered at the first threshold. The competition of two stimulated processes is elaborated with a rate-equation simulation that includes two optical modes, discussed below.

To gain qualitative understanding on the double-threshold behaviour and on the pulse duration dependence, I have performed a rate-equation simulation with a four-level gain medium introduced in Section 3.3. Here I include a second optical mode to the model to study competition of two modes. Also the second mode is resonant with the laser transition between level 2 and 1. As the measured time-integrated luminescence intensity increases at the second threshold, the total efficiency of the system must increase. Long pump pulses do not produce a second threshold so if the population inversion is created too slowly, the gain is not enough to reach the second threshold. This can happen because the stimulated thermalization does not compete with the spontaneous decay of excited molecules but rather with another stimulated process (that has a lower threshold!). In the rate equation model, the described situation can be imitated with two optical modes that have different balance of the radiative and

non-radiative lifetimes. In the following, the mode with lower threshold is called Mode 1 and the mode with higher threshold is called Mode 2. The extended model is defined with the following equations:

$$\frac{dn_1}{dt} = \beta n_1 \frac{(N_2 - N_1)}{\tau_{21}} + \beta \frac{N_2}{\tau_{21}} - \frac{n_1}{\tau_{\mathrm{r},1}} - \frac{n_1}{\tau_{\mathrm{nr},1}} \tag{5.8}$$

$$\frac{dn_2}{dt} = \beta n_2 \frac{(N_2 - N_1)}{\tau_{21}} + \beta \frac{N_2}{\tau_{21}} - \frac{n_2}{\tau_{\mathrm{r},2}} - \frac{n_2}{\tau_{\mathrm{nr},2}} \tag{5.9}$$

$$\frac{dN_0}{dt} = -rN_0 + \frac{N_2}{\tau_{20}} + \frac{N_1}{\tau_{10}} \tag{5.10}$$

$$\frac{dN_3}{dt} = rN_0 - \frac{N_3}{\tau_{32}} \tag{5.11}$$

$$\frac{dN_2}{dt} = -\beta n_1 \frac{(N_2 - N_1)}{\tau_{21}} - \beta n_2 \frac{(N_2 - N_1)}{\tau_{21}} - \frac{N_2}{\tau_{21}} - \frac{N_2}{\tau_{20}} + \frac{N_3}{\tau_{32}} \tag{5.12}$$

$$\frac{dN_1}{dt} = \beta n_1 \frac{(N_2 - N_1)}{\tau_{21}} + \beta n_2 \frac{(N_2 - N_1)}{\tau_{21}} + \frac{N_2}{\tau_{21}} - \frac{N_1}{\tau_{10}}, \tag{5.13}$$

where the population of each level are denoted with N_j and transition lifetimes with τ_j as shown previously. Here, n_i is the photon number in the corresponding mode $[i = 1,2]$, β is the same for both mode, and $\tau_{\mathrm{r,i}}$ and $\tau_{\mathrm{nr,i}}$, are the radiative and non-radiative lifetimes. The total lifetimes of the optical modes are called here cavity lifetimes, and they yield

$$\tau_{cav,i} = \frac{\tau_{\mathrm{r,i}} \tau_{\mathrm{nr,i}}}{\tau_{\mathrm{r,i}} + \tau_{\mathrm{nr,i}}}. \tag{5.14}$$

The threshold value for population inversion is

$$N^*_{th,i} = \frac{\tau_{21}}{\beta \tau_{cav,i}}, \tag{5.15}$$

that is the threshold value in the absence of the other mode. To have a smaller threshold value for Mode 1, the cavity lifetime of Mode 1 must be longer than that of Mode 2. To have considerable non-linear increase of output fluence at the second threshold, the ratio between the radiative and non-radiative lifetime for Mode 2 must be smaller than for Mode 1. This restricts the choice of lifetimes such that $\tau_{\mathrm{r},1} + \tau_{\mathrm{nr},1} > \tau_{\mathrm{r},2} + \tau_{\mathrm{nr},2}$ and $\tau_{\mathrm{r},1}/\tau_{\mathrm{nr},1} > \tau_{\mathrm{r},2}/\tau_{\mathrm{nr},2}$.

The simulation results are presented for two pump fluences and three different pulse durations in Figure 5.34, where I have used the following parameters: $\tau_{\mathrm{r},2} = \tau_{\mathrm{nr},2} = \tau_{\mathrm{nr},1} = 100$ fs and $\tau_{\mathrm{r},1} = 100\,\tau_{\mathrm{r},2} = 10$ ps. These values yield in cavity lifetime of $\tau_{cav,1} = 99$ fs and $\tau_{cav,2} = 50$ fs, respectively. It means that the threshold for Mode 1 is 50% lower than that for Mode 2, in case there would be only one optical mode

available. However, only 1% of the photons going into Mode 1 contribute to the output, in contrast to 50% of the photons in Mode 2. The β-factor is set to 10^{-3} for both modes and the transition lifetimes for the four-level gain medium are: $\tau_{32} = \tau_{10}$ = 50 fs and $\tau_{21} = \tau_{20}$ = 500 ps.

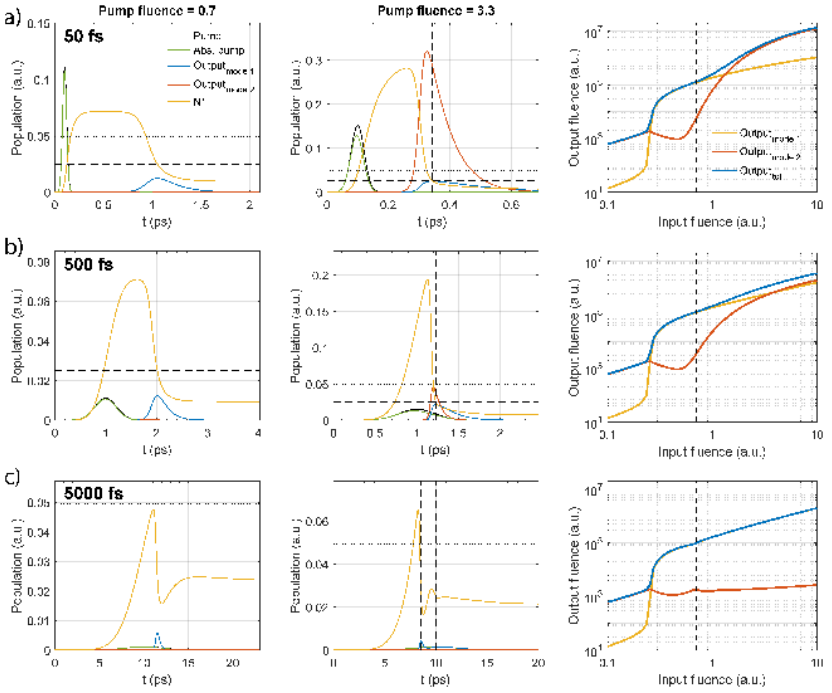

Figure 5.34. Rate equation simulation with two competing photonic modes, for three different pump pulse durations: (a) 50 fs, (b) 500 fs and (c) 5000 fs. The dashed and dotted horizontal lines indicate the theoretical inversion-threshold-values for Mode 1 and Mode 2, respectively. The qualitative behaviour of the input-output fluence curves is the same as for the experiments, where the double-threshold behaviour only occurs for a very short pump pulse. Moreover, for the 5000 fs pulse duration, the effective threshold for Mode 2 is not reached even at very high pump fluences.

In the simulation with 50 fs pump pulse, two thresholds are clearly reproduced in the time-integrated signal of summed Mode 1 and Mode 2. In the case of 500 fs pump pulse, the threshold for Mode 2 is still reached but the total output fluence does not show a significant non-linear increase. This case can be seen as the intermediate case. With a 5 ps pulse, the threshold for Mode 2 is not any more reached because Mode 1 starts to stimulate the population down already before the pump pulse reaches its maximum. Thus the population inversion never rises high enough for Mode 2 to start accumulating population.

As a disclaimer, the model here is just a toy model although it gives some intuition how the pump pulse duration can affect the dynamics of the system when two competing stimulated processes are involved. Here, the effective threshold for the Mode 2 (whatever stimulated process it is) is either reached or not reached depending on the pump pulse duration. In the experiments, the thermalization process competes from

the same gain with lasing. The simulations imply that if the population inversion is raised rapidly enough, the instantaneous inversion can reach a high enough value so that a process with a higher threshold can be triggered first. In this case, the higher-threshold process could extract more gain than the low-threshold process, as after the stimulated process is triggered, the population in the mode grows exponentially.

To fulfil the condition of $N^*_{th,2} > N^*_{th,1}$ but to obtain a non-linear increase of the total output fluence above the second threshold, we had to set $\tau_{r,1} \gg \tau_{r,2}$, and there is no particular reason why this would be the case in the experiment. On the other hand, it seems intuitive that the BEC needs more gain / has higher threshold because the thermalization process along propagation may involve higher losses than the distributed-feedback type lasing action. The actual thermalization mechanism and dynamics of the system cannot be modelled with this simple toy model. However, the simulation results suggest that a competition of two stimulated processes may be the reason why the condensation does not occur with longer pump pulse.

Sensitivity to the pump pulse duration endorses the ultrafast nature of plasmonic systems and highlights the sub-picosecond dynamics of the observed thermalization process. Besides the critical pump pulse duration, there is an optimal balance between the dye concentration, lattice size, and periodicity: the propagation time in which the polaritons reach the center of the array should match that time in which they red-shift to the band-edge energy. This maximises the population density that helps the BEC to emerge.

6. Conclusion and outlook

In this dissertation, I have studied diffractive plasmonic nanoparticle arrays that provide a fascinating platform to study quantum physics of light-matter interaction. I presented results of strong coupling between the optical modes supported by the plasmonic lattice and quantum emitters, namely fluorescent dye molecule Rhodamine 6G (Publication I). Rabi splittings of the order 100 meV were obtained with a 200 mM concentration of the molecule. As the strong coupling is a coherent quantum phenomenon, which produces Rabi oscillation of population between the coupled states, our results imply coherent coupling of distant dye molecules located within the mode volume of the delocalized SLR mode. The high field enhancement of plasmonic structures can enable reaching strong coupling even at a single emitter limit [217, 218]. Strong coupling also plays a role in ultrafast energy transfer and it can change chemical reactions [219]. Recent experiments and prospects related to strong coupling in chemistry have been comprehensively reviewed in [220–223].

The SLR mode can start lasing when the dye molecules, placed on top of the nanoparticle array, are optically excited. The lasing occurs in the band-edge of the SLR dispersion, where two-counter propagating SLR modes can couple and form a standing wave with zero group velocity. This condition provides feedback that is necessary for lasing action. Lasing in both bright and dark modes of the plasmonic lattice was achieved in Publication II in the visible wavelength range (with R6G). The out-coupling mechanism of the dark mode was based on the finite size of the plasmonic lattice, which caused a gradual built up of dipole moment toward the edges of the nanoparticle array. This novel out-coupling mechanism opens prospects of utilizing the dark modes that are expected to have comparably high quality factors due reduced radiative loss [33].

The plasmonic component makes the decay of the SLR modes ultrafast (about 100 fs) even if the lifetime is increased compared to localized plasmon resonances in single nanoparticles. Therefore the dynamics of any phenomenon involving these modes should be ultrafast. In Publication III, we studied the dynamics of pulse generation in the nanoparticle array laser with a double-pump spectroscopy, which utilizes the non-linear increase of luminescence intensity around the lasing threshold. We found that that the modulation speed, calculated from the inverse of the summed pulse built-up time and duration, can reach values of more than 100 GHz. Interestingly, the

modulation speed depended on the respective energy location of the SLR band edge and the dye emission maximum. When the band edge was tuned toward the blue side of the dye emission spectrum, the pulse generation became faster. Here, we used an infrared dye IR-140 that emits around $\lambda = 875$ nm.

Bose-Einstein condensation has gained growing interest in non- and quasi-equilibrium systems due to possibilities of studying non-equilibrium quantum physics [150, 165, 172, 178–180, 224, 225]. In Publication IV, we demonstrated for the first time a BEC in a plasmonic system, in an array of nanorods overlaid with a 50 mM solution of IR-792 molecule, at room temperature. We could directly show the macroscopic occupation of the ground state built up by red-shifting (thermalizing) population. We employed a rate-equation model of recurrent absorption and emission processes in the weak coupling regime to explain the experimental results. The simulations were performed in time domain, that could be compared to the experiments by mapping the propagation of condensing SLR excitations to time via the group velocity. The key experiment here was to monitor the spectral evolution of the luminescence as a function of position along the plasmonic lattice.

The Bose-Einstein condensation in the plasmonic lattice was further studied in Publication V, where the molecular concentration was increased so that we entered the strong coupling regime (IR-792 at 80 mM). The experimental setup was different compared to Publication IV, where we pumped the dye molecules at one end of the nanoparticle array and followed the propagation of SLR excitations away from the pump spot. In Publication V, we excited the molecules over the whole array with a pump spot larger than the array. In addition, the pump was directed to the sample through the microscope objective at normal incidence, which was crucial for simultaneous excitation of the molecules at every position of the lattice. Multimode condensation occurred at the lowest energies, and at the higher energies a thermalized distribution followed the Maxwell-Boltzmann distribution at a temperature of 333 K. Strikingly, the thermalized distribution was observed in the time-integrated signal. Together with the measured critical (maximum) pump pulse duration of about 250 fs, this indicates that the thermalization must occur at a 200 fs timescale. We explained this outstanding speed with strong coupling and stimulated processes. The sub-picosecond thermalization dynamics we observed is at a similar timescale as suggested for the fastest polariton condensates in organic semiconductor microcavities [226, 227], but it had not been directly measured before.

The research of this dissertation mainly contributes to the fundamental scientific knowledge of light-matter interaction in plasmonic systems and of room temperature non-equilibrium Bose-Einstein condensates. The condensation phenomenon I have studied may eventually find applications in optical data processing and in some areas of emerging quantum technologies. For example, it has already been shown that polariton condensates in optical microcavities can work as optical switches [228–230].

6.1 Prospects for future research

I make a final remark by giving suggestions for future research and experiments of the condensation phenomenon in the plasmonic lattice. First of all, being able to measure photon statistics (second order correlation function $g^{(2)}(\tau) = \langle g^{(2)}(t_1, t_2)\rangle_{t_2-t_1=\tau}$) of the BEC shows up as the holy grail. It would enable to definitively differentiate the BEC from lasing action, as $g^{(2)}(0) = 1$ is expected for lasing and $g^{(2)}(0) = 2$ for the BEC in a grand canonical ensemble, which probably describes our system at least for the highest molecular concentrations used. In the grand canonical number statistics, both the total energy and total number of the condensing particles can fluctuate, and it has been shown to apply for photon condensates [155, 169] where dye molecules act as both the thermal bath and particle reservoir, similar to our system. In Ref. [155] Schmitt et al. performed a beautiful experiment where they tuned the system from the canonical to the grand canonical ensemble ($g^{(2)}(0) : 1 \rightarrow 2$) by increasing the molecular concentration (size of the reservoir). However, measuring $g^{(2)}(\tau)$ at ultrafast timescales with a less than 100 fs resolution is a great challenge. It has been shown that photon statistics can be measured at these timescales by two-photon absorption in semiconductor material [231], which appears as a promising technique to measuring $g^{(2)}(\tau)$ also in our system. There are also some emerging technologies that extend the capabilities of streak cameras [232], which seem interesting to our studies.

Second, one relatively easy experiment would be to look at the sample luminescence truly at a singe pulse level. This can be very interesting for studying spontaneous symmetry breaking of the phase and / or polarization of the condensate. It is possible to reduce the repetition rate of the laser by adjusting the Pockels cells inside Astrella or just using an external chopper with a certain ratio of clear and blocked area. Third, a double-pump experiment, similar to the one performed in Publication III, could be also done for the BEC when pumping through the objective at normal incidence. Fourth, since the condensation is very sensitive to any asymmetry in the pumping geometry, breaking the geometry (e.g. pumping at a small angle) in a controlled manner could lead to interesting results. Fifth, the thermalization temperature could be studied with different emitters and by changing the external temperature. This would be feasible for the current system as the thermal tail has a lot of intensity and it stays linear (in logarithmic scale) over a large energy range. Sixth, it would be interesting to study the condensation with shorter excitation wavelengths to obtain even longer thermal tail, and also to investigate whether the condensation somehow depends on the excitation wavelength. Seventh, temporal coherence of the system, and the output (lasing and BEC) pulse durations could be measured also by implementing a delay line to one of the Michelson interferometer arms, and monitoring the fringe contrast as a function of time delay (optical path difference). Finally, one could try different particle shapes and sizes. Lasing threshold and linewidths, as well as sample robustness (photobleaching), could be studied also with much longer pump pulse durations. A small improvement would be a better control of the pulse duration, for instance with an external prism dispersion system.

Some fundamental open questions remain. What is the origin of the multiple con-

densate peaks around the band-edge energy? Why does the lasing action, which starts at a lower threshold, not always "beat" the thermalization process and the resulting BEC? Is there a relation between stimulated thermalization and superradiance? To answer these question, we need more experiments but also extensive theoretical work that goes beyond the current state-of-the-art theory [181, 182, 233, 234] of describing quantum dynamics of strongly interacting non-equilibrium systems, which involve a large number of molecules with vibrational states and multiple photonic modes with many excitations.

References

[1] L. Novotny and B. Hecht, *Principles of Nano-Optics*. Cambridge University Press, 2nd ed., 2012.

[2] W. L. Barnes, A. Dereux, and T. W. Ebbesen, "Surface plasmon subwavelength optics," *Nature*, vol. 424, pp. 824–830, Aug. 2003.

[3] M. S. Tame, K. R. McEnery, Ş. K. Özdemir, J. Lee, S. A. Maier, and M. S. Kim, "Quantum plasmonics," *Nature Physics*, vol. 9, pp. 329–340, June 2013.

[4] S. I. Bozhevolnyi, L. Martin-Moreno, and F. Garcia-Vidal, *Quantum Plasmonics*. Springer Series in Solid-State Sciences, Cham: Springer International Publishing, 2017.

[5] S. A. Maier and H. A. Atwater, "Plasmonics: Localization and guiding of electromagnetic energy in metal/dielectric structures," *Journal of Applied Physics*, vol. 98, p. 011101, July 2005.

[6] E. Ozbay, "Plasmonics: Merging Photonics and Electronics at Nanoscale Dimensions," *Science*, vol. 311, pp. 189–193, Jan. 2006.

[7] R. Zia, J. A. Schuller, A. Chandran, and M. L. Brongersma, "Plasmonics: The next chip-scale technology," *Materials Today*, vol. 9, pp. 20–27, July 2006.

[8] D. K. Gramotnev and S. I. Bozhevolnyi, "Plasmonics beyond the diffraction limit," *Nature Photonics*, vol. 4, pp. 83–91, Feb. 2010.

[9] J. A. Schuller, E. S. Barnard, W. Cai, Y. C. Jun, J. S. White, and M. L. Brongersma, "Plasmonics for extreme light concentration and manipulation," *Nature Materials*, vol. 9, pp. 193–204, Mar. 2010.

[10] H. Raether, *Surface Plasmons on Smooth and Rough Surfaces and on Gratings*. Berlin Heidelberg: Springer-Verlag, 1988.

[11] A. V. Zayats, I. I. Smolyaninov, and A. A. Maradudin, "Nano-optics of surface plasmon polaritons," *Physics Reports*, vol. 408, pp. 131–314, Mar. 2005.

[12] P. Mühlschlegel, H.-J. Eisler, O. J. F. Martin, B. Hecht, and D. W. Pohl, "Resonant Optical Antennas," *Science*, vol. 308, pp. 1607–1609, June 2005.

[13] R. de Waele, A. F. Koenderink, and A. Polman, "Tunable Nanoscale Localization of Energy on Plasmon Particle Arrays," *Nano Letters*, vol. 7, pp. 2004–2008, July 2007.

[14] P. Bharadwaj, B. Deutsch, and L. Novotny, "Optical Antennas," *Advances in Optics and Photonics*, vol. 1, pp. 438–483, Nov. 2009.

[15] L. Novotny and N. van Hulst, "Antennas for light," *Nature Photonics*, vol. 5, pp. 83–90, Feb. 2011.

[16] P. Biagioni, J.-S. Huang, and B. Hecht, "Nanoantennas for visible and infrared radiation," *Reports on Progress in Physics*, vol. 75, p. 024402, Jan. 2012.

[17] M. Kauranen and A. V. Zayats, "Nonlinear plasmonics," *Nature Photonics*, vol. 6, pp. 737–748, Nov. 2012.

[18] P. L. Stiles, J. A. Dieringer, N. C. Shah, and R. P. Van Duyne, "Surface-Enhanced Raman Spectroscopy," *Annual Review of Analytical Chemistry*, vol. 1, no. 1, pp. 601–626, 2008.

[19] B. Sharma, R. R. Frontiera, A.-I. Henry, E. Ringe, and R. P. Van Duyne, "SERS: Materials, applications, and the future," *Materials Today*, vol. 15, pp. 16–25, Jan. 2012.

[20] P. Anger, P. Bharadwaj, and L. Novotny, "Enhancement and Quenching of Single-Molecule Fluorescence," *Physical Review Letters*, vol. 96, p. 113002, Mar. 2006.

[21] G. Sun, J. B. Khurgin, and R. A. Soref, "Practical enhancement of photoluminescence by metal nanoparticles," *Applied Physics Letters*, vol. 94, p. 101103, Mar. 2009.

[22] P. Törmä and W. L. Barnes, "Strong coupling between surface plasmon polaritons and emitters: A review," *Reports on Progress in Physics*, vol. 78, no. 1, p. 013901, 2015.

[23] C. F. Bohren and D. R. Huffman, *Absorption and Scattering of Light by Small Particles*. Wiley-VCH, 1998.

[24] P. R. West, S. Ishii, G. V. Naik, N. K. Emani, V. M. Shalaev, and A. Boltasseva, "Searching for better plasmonic materials," *Laser & Photonics Reviews*, vol. 4, pp. 795–808, Nov. 2010.

[25] H. U. Yang, J. D'Archangel, M. L. Sundheimer, E. Tucker, G. D. Boreman, and M. B. Raschke, "Optical dielectric function of silver," *Physical Review B*, vol. 91, June 2015.

[26] R. L. Olmon, B. Slovick, T. W. Johnson, D. Shelton, S.-H. Oh, G. D. Boreman, and M. B. Raschke, "Optical dielectric function of gold," *Physical Review B*, vol. 86, Dec. 2012.

[27] V. A. Markel, "Coupled-dipole Approach to Scattering of Light from a One-dimensional Periodic Dipole Structure," *Journal of Modern Optics*, vol. 40, pp. 2281–2291, Nov. 1993.

[28] S. Zou, N. Janel, and G. C. Schatz, "Silver nanoparticle array structures that produce remarkably narrow plasmon lineshapes," *The Journal of Chemical Physics*, vol. 120, pp. 10871–10875, June 2004.

[29] F. J. García de Abajo, "Colloquium: Light scattering by particle and hole arrays," *Reviews of Modern Physics*, vol. 79, pp. 1267–1290, Oct. 2007.

[30] V. G. Kravets, F. Schedin, and A. N. Grigorenko, "Extremely Narrow Plasmon Resonances Based on Diffraction Coupling of Localized Plasmons in Arrays of Metallic Nanoparticles," *Physical Review Letters*, vol. 101, p. 087403, Aug. 2008.

[31] B. Auguié and W. L. Barnes, "Collective Resonances in Gold Nanoparticle Arrays," *Physical Review Letters*, vol. 101, p. 143902, Sept. 2008.

[32] Y. Chu, E. Schonbrun, T. Yang, and K. B. Crozier, "Experimental observation of narrow surface plasmon resonances in gold nanoparticle arrays," *Applied Physics Letters*, vol. 93, p. 181108, Nov. 2008.

[33] S. R. K. Rodriguez, A. Abass, B. Maes, O. T. A. Janssen, G. Vecchi, and J. Gómez Rivas, "Coupling Bright and Dark Plasmonic Lattice Resonances," *Physical Review X*, vol. 1, p. 021019, Dec. 2011.

[34] W. Wang, M. Ramezani, A. I. Väkeväinen, P. Törmä, J. G. Rivas, and T. W. Odom, "The rich photonic world of plasmonic nanoparticle arrays," *Materials Today*, vol. 21, pp. 303–314, Apr. 2018.

[35] V. G. Kravets, A. V. Kabashin, W. L. Barnes, and A. N. Grigorenko, "Plasmonic Surface Lattice Resonances: A Review of Properties and Applications," *Chemical Reviews*, vol. 118, pp. 5912–5951, June 2018.

[36] A. Einstein, "On the quantum theory of radiation," *Physikalische Zeitschrift*, vol. 18, p. 121, 1917.

[37] A. E. Siegman, *Lasers*. Mill Valley, CA: University Science Books, 1986.

[38] S. Hooker and C. Webb, *Laser Physics*. Oxford Master Series in Atomic, Optical, and Laser Physics, Oxford University Press, 2010.

[39] P. J. Winzer, D. T. Neilson, and A. R. Chraplyvy, "Fiber-optic transmission and networking: The previous 20 and the next 20 years [Invited]," *Optics Express*, vol. 26, pp. 24190–24239, Sept. 2018.

[40] K. J. Vahala, "Optical microcavities," *Nature*, vol. 424, pp. 839–846, Aug. 2003.

[41] S. Noda, "Seeking the Ultimate Nanolaser," *Science*, vol. 314, pp. 260–261, Oct. 2006.

[42] M. T. Hill and M. C. Gather, "Advances in small lasers," *Nature Photonics*, vol. 8, pp. 908–918, Dec. 2014.

[43] R.-M. Ma, X. Yin, R. F. Oulton, V. J. Sorger, and X. Zhang, "Multiplexed and Electrically Modulated Plasmon Laser Circuit," *Nano Letters*, vol. 12, pp. 5396–5402, Oct. 2012.

[44] E. Bermúdez-Ureña, G. Tutuncuoglu, J. Cuerda, C. L. C. Smith, J. Bravo-Abad, S. I. Bozhevolnyi, A. Fontcuberta i Morral, F. J. García-Vidal, and R. Quidant, "Plasmonic Waveguide-Integrated Nanowire Laser," *Nano Letters*, vol. 17, pp. 747–754, Feb. 2017.

[45] A. Yang, D. Wang, W. Wang, and T. W. Odom, "Coherent Light Sources at the Nanoscale," *Annual Review of Physical Chemistry*, vol. 68, no. 1, pp. 83–99, 2017.

[46] Y.-L. Ho, J. K. Clark, A. S. A. Kamal, and J.-J. Delaunay, "On-Chip Monolithically Fabricated Plasmonic-Waveguide Nanolaser," *Nano Letters*, vol. 18, pp. 7769–7776, Dec. 2018.

[47] E. I. Galanzha, R. Weingold, D. A. Nedosekin, M. Sarimollaoglu, J. Nolan, W. Harrington, A. S. Kuchyanov, R. G. Parkhomenko, F. Watanabe, Z. Nima, A. S. Biris, A. I. Plekhanov, M. I. Stockman, and V. P. Zharov, "Spaser as a biological probe," *Nature Communications*, vol. 8, p. 15528, June 2017.

[48] N. P. Proukakis, D. W. Snoke, and P. B. Littlewood, *Universal Themes of Bose-Einstein Condensation*. Cambridge University Press, May 2017.

[49] D. J. Griffiths, *Introduction to Quantum Mechanics*. Pearson, Prentice Hall, 2nd ed., 2005.

[50] Wikipedia, "Particle physics." https://en.wikipedia.org/wiki/Particle_physics. Accessed 28/5/2019.

[51] O. Penrose and L. Onsager, "Bose-Einstein Condensation and Liquid Helium," *Physical Review*, vol. 104, pp. 576–584, Nov. 1956.

[52] G. E. Volovik, *The Universe in a Helium Droplet*. Oxford University Press, Feb. 2009.

[53] J. Bardeen, L. N. Cooper, and J. R. Schrieffer, "Theory of Superconductivity," *Physical Review*, vol. 108, pp. 1175–1204, Dec. 1957.

[54] P. A. Lee, N. Nagaosa, and X.-G. Wen, "Doping a Mott insulator: Physics of high-temperature superconductivity," *Reviews of Modern Physics*, vol. 78, pp. 17–85, Jan. 2006.

[55] W. Zwerger, ed., *The BCS-BEC Crossover and the Unitary Fermi Gas*. Lecture Notes in Physics, Berlin: Springer-Verlag, 2012.

[56] D. G. Baranov, M. Wersäll, J. Cuadra, T. J. Antosiewicz, and T. Shegai, "Novel Nanostructures and Materials for Strong Light–Matter Interactions," *ACS Photonics*, vol. 5, pp. 24–42, Jan. 2018.

[57] J. P. Gordon, H. J. Zeiger, and C. H. Townes, "The Maser – New Type of Microwave Amplifier, Frequency Standard, and Spectrometer," *Physical Review*, vol. 99, pp. 1264–1274, Aug. 1955.

[58] A. L. Schawlow and C. H. Townes, "Infrared and Optical Masers," *Physical Review*, vol. 112, pp. 1940–1949, Dec. 1958.

[59] T. H. Maiman, R. H. Hoskins, I. J. D'Haenens, C. K. Asawa, and V. Evtuhov, "Stimulated Optical Emission in Fluorescent Solids. II. Spectroscopy and Stimulated Emission in Ruby," *Physical Review*, vol. 123, pp. 1151–1157, Aug. 1961.

[60] R.-M. Ma, R. F. Oulton, V. J. Sorger, and X. Zhang, "Plasmon lasers: Coherent light source at molecular scales," *Laser & Photonics Reviews*, vol. 7, pp. 1–21, Jan. 2013.

[61] D. Wang, W. Wang, M. P. Knudson, G. C. Schatz, and T. W. Odom, "Structural Engineering in Plasmon Nanolasers," *Chemical Reviews*, vol. 118, no. 6, pp. 2865–2881, 2018.

[62] H. Wu, Y. Gao, P. Xu, X. Guo, P. Wang, D. Dai, and L. Tong, "Plasmonic Nanolasers: Pursuing Extreme Lasing Conditions on Nanoscale," *Advanced Optical Materials*, p. 1900334, Apr. 2019.

[63] C. Sirtori, C. Gmachl, F. Capasso, J. Faist, D. L. Sivco, A. L. Hutchinson, and A. Y. Cho, "Long-wavelength ($\lambda \approx 8$–11.5μm) semiconductor lasers with waveguides based on surface plasmons," *Optics Letters*, vol. 23, pp. 1366–1368, Sept. 1998.

[64] D. J. Bergman and M. I. Stockman, "Surface Plasmon Amplification by Stimulated Emission of Radiation: Quantum Generation of Coherent Surface Plasmons in Nanosystems," *Physical Review Letters*, vol. 90, p. 027402, Jan. 2003.

[65] M. I. Stockman, "Spasers explained," *Nature Photonics*, vol. 2, pp. 327–329, June 2008.

[66] M. I. Stockman, "The spaser as a nanoscale quantum generator and ultrafast amplifier," *Journal of Optics*, vol. 12, p. 024004, Jan. 2010.

[67] M. A. Noginov, G. Zhu, A. M. Belgrave, R. Bakker, V. M. Shalaev, E. E. Narimanov, S. Stout, E. Herz, T. Suteewong, and U. Wiesner, "Demonstration of a spaser-based nanolaser," *Nature*, vol. 460, pp. 1110–1112, Aug. 2009.

[68] X. Meng, A. V. Kildishev, K. Fujita, K. Tanaka, and V. M. Shalaev, "Wavelength-Tunable Spasing in the Visible," *Nano Letters*, vol. 13, pp. 4106–4112, Sept. 2013.

[69] J. Ziegler, C. Wörister, C. Vidal, C. Hrelescu, and T. A. Klar, "Plasmonic Nanostars as Efficient Broadband Scatterers for Random Lasing," *ACS Photonics*, vol. 3, pp. 919–923, June 2016.

[70] Z. Wang, X. Meng, A. V. Kildishev, A. Boltasseva, and V. M. Shalaev, "Nanolasers Enabled by Metallic Nanoparticles: From Spasers to Random Lasers," *Laser & Photonics Reviews*, vol. 11, no. 6, p. 1700212, 2017.

[71] S. J. P. Kress, J. Cui, P. Rohner, D. K. Kim, F. V. Antolinez, K.-A. Zaininger, S. V. Jayanti, P. Richner, K. M. McPeak, D. Poulikakos, and D. J. Norris, "A customizable class of colloidal-quantum-dot spasers and plasmonic amplifiers," *Science Advances*, vol. 3, p. e1700688, Sept. 2017.

[72] E. W. de Vos, M. J. A. de Dood, and M. P. van Exter, "Surface plasmon laser with two hole arrays as cavity mirrors," *Optica*, vol. 6, pp. 92–95, Jan. 2019.

[73] R. F. Oulton, V. J. Sorger, T. Zentgraf, R.-M. Ma, C. Gladden, L. Dai, G. Bartal, and X. Zhang, "Plasmon lasers at deep subwavelength scale," *Nature*, vol. 461, pp. 629–632, Oct. 2009.

[74] Y.-J. Lu, J. Kim, H.-Y. Chen, C. Wu, N. Dabidian, C. E. Sanders, C.-Y. Wang, M.-Y. Lu, B.-H. Li, X. Qiu, W.-H. Chang, L.-J. Chen, G. Shvets, C.-K. Shih, and S. Gwo, "Plasmonic Nanolaser Using Epitaxially Grown Silver Film," *Science*, vol. 337, pp. 450–453, July 2012.

[75] Y.-J. Lu, C.-Y. Wang, J. Kim, H.-Y. Chen, M.-Y. Lu, Y.-C. Chen, W.-H. Chang, L.-J. Chen, M. I. Stockman, C.-K. Shih, and S. Gwo, "All-Color Plasmonic Nanolasers with Ultralow Thresholds: Autotuning Mechanism for Single-Mode Lasing," *Nano Letters*, vol. 14, pp. 4381–4388, Aug. 2014.

[76] Q. Zhang, G. Li, X. Liu, F. Qian, Y. Li, T. C. Sum, C. M. Lieber, and Q. Xiong, "A room temperature low-threshold ultraviolet plasmonic nanolaser," *Nature Communications*, vol. 5, p. 4953, Sept. 2014.

[77] T. P. H. Sidiropoulos, R. Röder, S. Geburt, O. Hess, S. A. Maier, C. Ronning, and R. F. Oulton, "Ultrafast plasmonic nanowire lasers near the surface plasmon frequency," *Nature Physics*, vol. 10, pp. 870–876, Nov. 2014.

[78] R. Röder, T. P. H. Sidiropoulos, C. Tessarek, S. Christiansen, R. F. Oulton, and C. Ronning, "Ultrafast Dynamics of Lasing Semiconductor Nanowires," *Nano Letters*, vol. 15, pp. 4637–4643, July 2015.

[79] C.-J. Lee, H. Yeh, F. Cheng, P.-H. Su, T.-H. Her, Y.-C. Chen, C.-Y. Wang, S. Gwo, S. R. Bank, C.-K. Shih, and W.-H. Chang, "Low-Threshold Plasmonic Lasers on a Single-Crystalline Epitaxial Silver Platform at Telecom Wavelength," *ACS Photonics*, vol. 4, pp. 1431–1439, June 2017.

[80] S.-H. Kwon, J.-H. Kang, C. Seassal, S.-K. Kim, P. Regreny, Y.-H. Lee, C. M. Lieber, and H.-G. Park, "Subwavelength Plasmonic Lasing from a Semiconductor Nanodisk with Silver Nanopan Cavity," *Nano Letters*, vol. 10, pp. 3679–3683, Sept. 2010.

[81] R.-M. Ma, R. F. Oulton, V. J. Sorger, G. Bartal, and X. Zhang, "Room-temperature sub-diffraction-limited plasmon laser by total internal reflection," *Nature Materials*, vol. 10, pp. 110–113, Feb. 2011.

[82] S. Wang, X.-Y. Wang, B. Li, H.-Z. Chen, Y.-L. Wang, L. Dai, R. F. Oulton, and R.-M. Ma, "Unusual scaling laws for plasmonic nanolasers beyond the diffraction limit," *Nature Communications*, vol. 8, Dec. 2017.

[83] X. Wu, Y. Xiao, C. Meng, X. Zhang, S. Yu, Y. Wang, C. Yang, X. Guo, C. Z. Ning, and L. Tong, "Hybrid Photon-Plasmon Nanowire Lasers," *Nano Letters*, vol. 13, pp. 5654–5659, Nov. 2013.

[84] Y. J. Li, Y. Lv, C.-L. Zou, W. Zhang, J. Yao, and Y. S. Zhao, "Output Coupling of Perovskite Lasers from Embedded Nanoscale Plasmonic Waveguides," *Journal of the American Chemical Society*, vol. 138, pp. 2122–2125, Feb. 2016.

[85] M. Khajavikhan, A. Simic, M. Katz, J. H. Lee, B. Slutsky, A. Mizrahi, V. Lomakin, and Y. Fainman, "Thresholdless nanoscale coaxial lasers," *Nature*, vol. 482, pp. 204–207, Feb. 2012.

[86] M. T. Hill, Y.-S. Oei, B. Smalbrugge, Y. Zhu, T. de Vries, P. J. van Veldhoven, F. W. M. van Otten, T. J. Eijkemans, J. P. Turkiewicz, H. de Waardt, E. J. Geluk, S.-H. Kwon, Y.-H. Lee, R. Nötzel, and M. K. Smit, "Lasing in metallic-coated nanocavities," *Nature Photonics*, vol. 1, pp. 589–594, Oct. 2007.

[87] M. T. Hill, M. Marell, E. S. P. Leong, B. Smalbrugge, Y. Zhu, M. Sun, P. J. van Veldhoven, E. J. Geluk, F. Karouta, Y.-S. Oei, R. Nötzel, C.-Z. Ning, and M. K. Smit, "Lasing in metal-insulator-metal sub-wavelength plasmonic waveguides," *Optics Express*, vol. 17, pp. 11107–11112, June 2009.

[88] K. Ding, Z. C. Liu, L. J. Yin, M. T. Hill, M. J. H. Marell, P. J. van Veldhoven, R. Nöetzel, and C. Z. Ning, "Room-temperature continuous wave lasing in deep-subwavelength metallic cavities under electrical injection," *Physical Review B*, vol. 85, p. 041301, Jan. 2012.

[89] K. Ding, M. T. Hill, Z. C. Liu, L. J. Yin, P. J. van Veldhoven, and C. Z. Ning, "Record performance of electrical injection sub-wavelength metallic-cavity semiconductor lasers at room temperature," *Optics Express*, vol. 21, pp. 4728–4733, Feb. 2013.

[90] S. Gwo and C.-K. Shih, "Semiconductor plasmonic nanolasers: Current status and perspectives," *Reports on Progress in Physics*, vol. 79, no. 8, p. 086501, 2016.

[91] J. Y. Suh, C. H. Kim, W. Zhou, M. D. Huntington, D. T. Co, M. R. Wasielewski, and T. W. Odom, "Plasmonic Bowtie Nanolaser Arrays," *Nano Letters*, vol. 12, pp. 5769–5774, Nov. 2012.

[92] W. Zhou, M. Dridi, J. Y. Suh, C. H. Kim, D. T. Co, M. R. Wasielewski, G. C. Schatz, and T. W. Odom, "Lasing action in strongly coupled plasmonic nanocavity arrays," *Nature Nanotechnology*, vol. 8, pp. 506–511, July 2013.

[93] A. H. Schokker and A. F. Koenderink, "Lasing at the band edges of plasmonic lattices," *Physical Review B*, vol. 90, p. 155452, Oct. 2014.

[94] A. Yang, T. B. Hoang, M. Dridi, C. Deeb, M. H. Mikkelsen, G. C. Schatz, and T. W. Odom, "Real-time tunable lasing from plasmonic nanocavity arrays," *Nature Communications*, vol. 6, p. 6939, Apr. 2015.

[95] A. H. Schokker and A. F. Koenderink, "Statistics of Randomized Plasmonic Lattice Lasers," *ACS Photonics*, vol. 2, pp. 1289–1297, Sept. 2015.

[96] A. Yang, Z. Li, M. P. Knudson, A. J. Hryn, W. Wang, K. Aydin, and T. W. Odom, "Unidirectional Lasing from Template-Stripped Two-Dimensional Plasmonic Crystals," *ACS Nano*, vol. 9, pp. 11582–11588, Dec. 2015.

[97] A. H. Schokker and A. F. Koenderink, "Lasing in quasi-periodic and aperiodic plasmon lattices," *Optica*, vol. 3, p. 686, July 2016.

[98] D. Wang, A. Yang, W. Wang, Y. Hua, R. D. Schaller, G. C. Schatz, and T. W. Odom, "Band-edge engineering for controlled multi-modal nanolasing in plasmonic superlattices," *Nature Nanotechnology*, vol. 12, pp. 889–894, Sept. 2017.

[99] C. Deeb, Z. Guo, A. Yang, L. Huang, and T. W. Odom, "Correlating Nanoscopic Energy Transfer and Far-Field Emission to Unravel Lasing Dynamics in Plasmonic Nanocavity Arrays," *Nano Letters*, vol. 18, pp. 1454–1459, Feb. 2018.

[100] K. Guo and A. F. Koenderink, "Spatial Intensity Distribution in Plasmonic Particle Array Lasers," *Physical Review Applied*, vol. 11, p. 024025, Feb. 2019.

[101] R. Guo, M. Nečada, T. K. Hakala, A. I. Väkeväinen, and P. Törmä, "Lasing at *K* Points of a Honeycomb Plasmonic Lattice," *Physical Review Letters*, vol. 122, p. 013901, Jan. 2019.

[102] H. T. Rekola, T. K. Hakala, and P. Törmä, "One-Dimensional Plasmonic Nanoparticle Chain Lasers," *ACS Photonics*, vol. 5, pp. 1822–1826, May 2018.

[103] S. Pourjamal, T. K. Hakala, M. Nečada, F. Freire-Fernández, M. Kataja, H. Rekola, J.-P. Martikainen, P. Törmä, and S. van Dijken, "Lasing in Ni Nanodisk Arrays," *ACS Nano*, vol. 13, pp. 5686–5692, Apr. 2019.

[104] S. T. Ha, Y. H. Fu, N. K. Emani, Z. Pan, R. M. Bakker, R. Paniagua-Domínguez, and A. I. Kuznetsov, "Directional lasing in resonant semiconductor nanoantenna arrays," *Nature Nanotechnology*, vol. 13, p. 1042, Nov. 2018.

[105] F. van Beijnum, P. J. van Veldhoven, E. J. Geluk, M. J. A. de Dood, G. W. 't Hooft, and M. P. van Exter, "Surface Plasmon Lasing Observed in Metal Hole Arrays," *Physical Review Letters*, vol. 110, p. 206802, May 2013.

[106] M. P. van Exter, V. T. Tenner, F. van Beijnum, M. J. A. de Dood, P. J. van Veldhoven, E. J. Geluk, and G. W. 't Hooft, "Surface plasmon dispersion in metal hole array lasers," *Optics Express*, vol. 21, pp. 27422–27437, Nov. 2013.

[107] V. T. Tenner, A. N. van Delft, M. J. A. de Dood, and M. P. van Exter, "Loss and scattering of surface plasmon polaritons on optically-pumped hole arrays," *Journal of Optics*, vol. 16, p. 114019, Nov. 2014.

[108] V. T. Tenner, M. J. A. de Dood, and M. P. van Exter, "Two-mode surface plasmon lasing in hexagonal arrays," *Optics Letters*, vol. 43, pp. 166–169, Jan. 2018.

[109] X. Meng, J. Liu, A. V. Kildishev, and V. M. Shalaev, "Highly directional spaser array for the red wavelength region," *Laser & Photonics Reviews*, vol. 8, no. 6, pp. 896–903, 2014.

[110] S. N. Bose, "Planck's Law and Light Quantum Hypothesis," *Zeitschrift für Physik*, vol. 26, pp. 178–181, Dec. 1924.

[111] A. Einstein, "Quantum theory of the monoatomic ideal gas, Part I," in *Sitzungsberichte Der Preussischen Akademie Der Wissenschaften*, vol. 22, pp. 261–267, July 1924.

[112] A. Einstein, "Quantum theory of the monoatomic ideal gas, Part II," in *Sitzungsberichte Der Preussischen Akademie Der Wissenschaften*, vol. 1, pp. 3–14, Jan. 1925.

[113] P. Kapitza, "Viscosity of Liquid Helium below the λ-Point," *Nature*, vol. 141, p. 74, Jan. 1938.

[114] J. F. Allen and A. D. Misener, "Flow of Liquid Helium II," *Nature*, vol. 141, p. 75, Jan. 1938.

[115] F. London, "The λ-Phenomenon of Liquid Helium and the Bose-Einstein Degeneracy," *Nature*, vol. 141, p. 643, Apr. 1938.

[116] F. London, "On the Bose-Einstein Condensation," *Physical Review*, vol. 54, pp. 947–954, Dec. 1938.

[117] M. H. Anderson, J. R. Ensher, M. R. Matthews, C. E. Wieman, and E. A. Cornell, "Observation of Bose-Einstein Condensation in a Dilute Atomic Vapor," *Science*, vol. 269, pp. 198–201, July 1995.

[118] K. B. Davis, M. O. Mewes, M. R. Andrews, N. J. van Druten, D. S. Durfee, D. M. Kurn, and W. Ketterle, "Bose-Einstein Condensation in a Gas of Sodium Atoms," *Physical Review Letters*, vol. 75, pp. 3969–3973, Nov. 1995.

[119] C. C. Bradley, C. A. Sackett, J. J. Tollett, and R. G. Hulet, "Evidence of Bose-Einstein Condensation in an Atomic Gas with Attractive Interactions," *Physical Review Letters*, vol. 75, pp. 1687–1690, Aug. 1995.

[120] D. G. Fried, T. C. Killian, L. Willmann, D. Landhuis, S. C. Moss, D. Kleppner, and T. J. Greytak, "Bose-Einstein Condensation of Atomic Hydrogen," *Physical Review Letters*, vol. 81, pp. 3811–3814, Nov. 1998.

[121] A. I. Safonov, S. A. Vasilyev, I. S. Yasnikov, I. I. Lukashevich, and S. Jaakkola, "Observation of Quasicondensate in Two-Dimensional Atomic Hydrogen," *Physical Review Letters*, vol. 81, pp. 4545–4548, Nov. 1998.

[122] T. Nikuni, M. Oshikawa, A. Oosawa, and H. Tanaka, "Bose-Einstein Condensation of Dilute Magnons in $TlCuCl_3$," *Physical Review Letters*, vol. 84, pp. 5868–5871, June 2000.

[123] R. Coldea, D. A. Tennant, K. Habicht, P. Smeibidl, C. Wolters, and Z. Tylczynski, "Direct Measurement of the Spin Hamiltonian and Observation of Condensation of Magnons in the 2D Frustrated Quantum Magnet Cs_2CuCl_4," *Physical Review Letters*, vol. 88, p. 137203, Mar. 2002.

[124] C. Rüegg, N. Cavadini, A. Furrer, H.-U. Güdel, K. Krämer, H. Mutka, A. Wildes, K. Habicht, and P. Vorderwisch, "Bose-Einstein condensation of the triplet states in the magnetic insulator $TlCuCl_3$," *Nature*, vol. 423, p. 62, May 2003.

[125] M. Jaime, V. F. Correa, N. Harrison, C. D. Batista, N. Kawashima, Y. Kazuma, G. A. Jorge, R. Stern, I. Heinmaa, S. A. Zvyagin, Y. Sasago, and K. Uchinokura, "Magnetic-Field-Induced Condensation of Triplons in Han Purple Pigment $BaCuSi_2O_6$," *Physical Review Letters*, vol. 93, p. 087203, Aug. 2004.

[126] T. Radu, H. Wilhelm, V. Yushankhai, D. Kovrizhin, R. Coldea, Z. Tylczynski, T. Lühmann, and F. Steglich, "Bose-Einstein Condensation of Magnons in Cs_2CuCl_4," *Physical Review Letters*, vol. 95, p. 127202, Sept. 2005.

[127] T. Giamarchi, C. Rüegg, and O. Tchernyshyov, "Bose-Einstein condensation in magnetic insulators," *Nature Physics*, vol. 4, pp. 198–204, Mar. 2008.

[128] H. Deng, G. Weihs, C. Santori, J. Bloch, and Y. Yamamoto, "Condensation of Semiconductor Microcavity Exciton Polaritons," *Science*, vol. 298, pp. 199–202, Oct. 2002.

[129] J. Kasprzak, M. Richard, S. Kundermann, A. Baas, P. Jeambrun, J. M. J. Keeling, F. M. Marchetti, M. H. Szymańska, R. André, J. L. Staehli, V. Savona, P. B. Littlewood, B. Deveaud, and L. S. Dang, "Bose–Einstein condensation of exciton polaritons," *Nature*, vol. 443, pp. 409–414, Sept. 2006.

[130] R. Balili, V. Hartwell, D. Snoke, L. Pfeiffer, and K. West, "Bose-Einstein Condensation of Microcavity Polaritons in a Trap," *Science*, vol. 316, pp. 1007–1010, May 2007.

[131] H. Deng, H. Haug, and Y. Yamamoto, "Exciton-polariton Bose-Einstein condensation," *Reviews of Modern Physics*, vol. 82, pp. 1489–1537, May 2010.

[132] T. Byrnes, N. Y. Kim, and Y. Yamamoto, "Exciton-polariton condensates," *Nature Physics*, vol. 10, pp. 803–813, Nov. 2014.

[133] O. Vainio, J. Ahokas, J. Järvinen, L. Lehtonen, S. Novotny, S. Sheludiakov, K.-A. Suominen, S. Vasiliev, D. Zvezdov, V. V. Khmelenko, and D. M. Lee, "Bose-Einstein Condensation of Magnons in Atomic Hydrogen Gas," *Physical Review Letters*, vol. 114, p. 125304, Mar. 2015.

[134] S. O. Demokritov, V. E. Demidov, O. Dzyapko, G. A. Melkov, A. A. Serga, B. Hillebrands, and A. N. Slavin, "Bose-Einstein condensation of quasi-equilibrium magnons at room temperature under pumping," *Nature*, vol. 443, p. 430, Sept. 2006.

[135] J. J. Baumberg, A. V. Kavokin, S. Christopoulos, A. J. D. Grundy, R. Butté, G. Christmann, D. D. Solnyshkov, G. Malpuech, G. Baldassarri Höger von Högersthal, E. Feltin, J.-F. Carlin, and N. Grandjean, "Spontaneous Polarization Buildup in a Room-Temperature Polariton Laser," *Physical Review Letters*, vol. 101, p. 136409, Sept. 2008.

[136] S. Kéna-Cohen and S. R. Forrest, "Room-temperature polariton lasing in an organic single-crystal microcavity," *Nature Photonics*, vol. 4, pp. 371–375, June 2010.

[137] K. S. Daskalakis, S. A. Maier, R. Murray, and S. Kéna-Cohen, "Nonlinear interactions in an organic polariton condensate," *Nature Materials*, vol. 13, pp. 271–278, Mar. 2014.

[138] J. D. Plumhof, T. Stöferle, L. Mai, U. Scherf, and R. F. Mahrt, "Room-temperature Bose–Einstein condensation of cavity exciton–polaritons in a polymer," *Nature Materials*, vol. 13, pp. 247–252, Mar. 2014.

[139] K. S. Daskalakis, S. A. Maier, and S. Kéna-Cohen, "Spatial Coherence and Stability in a Disordered Organic Polariton Condensate," *Physical Review Letters*, vol. 115, p. 035301, July 2015.

[140] T. Guillet and C. Brimont, "Polariton condensates at room temperature," *Comptes Rendus Physique*, vol. 17, pp. 946–956, Oct. 2016.

[141] R. Su, C. Diederichs, J. Wang, T. C. H. Liew, J. Zhao, S. Liu, W. Xu, Z. Chen, and Q. Xiong, "Room-Temperature Polariton Lasing in All-Inorganic Perovskite Nanoplatelets," *Nano Letters*, vol. 17, pp. 3982–3988, June 2017.

[142] F. Scafirimuto, D. Urbonas, U. Scherf, R. F. Mahrt, and T. Stöferle, "Room-Temperature Exciton-Polariton Condensation in a Tunable Zero-Dimensional Microcavity," *ACS Photonics*, vol. 5, pp. 85–89, Jan. 2018.

[143] N. Bobrovska, M. Matuszewski, K. S. Daskalakis, S. A. Maier, and S. Kéna-Cohen, "Dynamical Instability of a Nonequilibrium Exciton-Polariton Condensate," *ACS Photonics*, vol. 5, pp. 111–118, Jan. 2018.

[144] S. K. Rajendran, M. Wei, H. Ohadi, A. Ruseckas, G. A. Turnbull, and I. D. W. Samuel, "Low Threshold Polariton Lasing from a Solution-Processed Organic Semiconductor in a Planar Microcavity," *Advanced Optical Materials*, vol. 0, no. 0, p. 1801791, 2019.

[145] C. P. Dietrich, A. Steude, L. Tropf, M. Schubert, N. M. Kronenberg, K. Ostermann, S. Höfling, and M. C. Gather, "An exciton-polariton laser based on biologically produced fluorescent protein," *Science Advances*, vol. 2, p. e1600666, Aug. 2016.

[146] J. Klaers, J. Schmitt, F. Vewinger, and M. Weitz, "Bose-Einstein condensation of photons in an optical microcavity," *Nature*, vol. 468, pp. 545–548, Nov. 2010.

[147] K. G. Lagoudakis, M. Wouters, M. Richard, A. Baas, I. Carusotto, R. André, L. S. Dang, and B. Deveaud-Plédran, "Quantized vortices in an exciton–polariton condensate," *Nature Physics*, vol. 4, pp. 706–710, Sept. 2008.

[148] A. Amo, J. Lefrère, S. Pigeon, C. Adrados, C. Ciuti, I. Carusotto, R. Houdré, E. Giacobino, and A. Bramati, "Superfluidity of polaritons in semiconductor microcavities," *Nature Physics*, vol. 5, pp. 805–810, Nov. 2009.

[149] A. Amo, D. Sanvitto, F. P. Laussy, D. Ballarini, E. del Valle, M. D. Martin, A. Lemaître, J. Bloch, D. N. Krizhanovskii, M. S. Skolnick, C. Tejedor, and L. Viña, "Collective fluid dynamics of a polariton condensate in a semiconductor microcavity," *Nature*, vol. 457, pp. 291–295, Jan. 2009.

[150] J. Keeling, L. M. Sieberer, E. Altman, L. Chen, S. Diehl, and J. Toner, "Superfluidity and Phase Correlations of Driven Dissipative Condensates," in *Universal Themes of Bose-Einstein Condensation*, pp. 205–230, Cambridge University Press, 2017.

[151] G. Lerario, A. Fieramosca, F. Barachati, D. Ballarini, K. S. Daskalakis, L. Dominici, M. De Giorgi, S. A. Maier, G. Gigli, S. Kéna-Cohen, and D. Sanvitto, "Room-temperature superfluidity in a polariton condensate," *Nature Physics*, vol. 13, pp. 837–841, Sept. 2017.

[152] J. Klaers, F. Vewinger, and M. Weitz, "Thermalization of a two-dimensional photonic gas in a 'white wall' photon box," *Nature Physics*, vol. 6, pp. 512–515, July 2010.

[153] J. Klaers, J. Schmitt, T. Damm, F. Vewinger, and M. Weitz, "Bose-Einstein condensation of paraxial light," *Applied Physics B*, vol. 105, p. 17, Sept. 2011.

[154] J. Klaers and M. Weitz, "Bose-Einstein condensation of photons," *arXiv:1210.7707 [cond-mat]*, Oct. 2012.

[155] J. Schmitt, T. Damm, D. Dung, F. Vewinger, J. Klaers, and M. Weitz, "Observation of Grand-Canonical Number Statistics in a Photon Bose-Einstein Condensate," *Physical Review Letters*, vol. 112, p. 030401, Jan. 2014.

[156] J. Marelic and R. A. Nyman, "Experimental evidence for inhomogeneous pumping and energy-dependent effects in photon Bose-Einstein condensation," *Physical Review A*, vol. 91, p. 033813, Mar. 2015.

[157] J. Schmitt, T. Damm, D. Dung, F. Vewinger, J. Klaers, and M. Weitz, "Thermalization kinetics of light: From laser dynamics to equilibrium condensation of photons," *Physical Review A*, vol. 92, p. 011602, July 2015.

[158] T. Damm, J. Schmitt, Q. Liang, D. Dung, F. Vewinger, M. Weitz, and J. Klaers, "Calorimetry of a Bose-Einstein-condensed photon gas," *Nature Communications*, vol. 7, p. 11340, Apr. 2016.

[159] J. Marelic, L. F. Zajiczek, H. J. Hesten, K. H. Leung, E. Y. X. Ong, F. Mintert, and R. A. Nyman, "Spatiotemporal coherence of non-equilibrium multimode photon condensates," *New Journal of Physics*, vol. 18, no. 10, p. 103012, 2016.

[160] J. Marelic, B. T. Walker, and R. A. Nyman, "Phase-space views into dye-microcavity thermalized and condensed photons," *Physical Review A*, vol. 94, p. 063812, Dec. 2016.

[161] T. Damm, D. Dung, F. Vewinger, M. Weitz, and J. Schmitt, "First-order spatial coherence measurements in a thermalized two-dimensional photonic quantum gas," *Nature Communications*, vol. 8, p. 158, July 2017.

[162] D. Dung, C. Kurtscheid, T. Damm, J. Schmitt, F. Vewinger, M. Weitz, and J. Klaers, "Variable potentials for thermalized light and coupled condensates," *Nature Photonics*, vol. 11, pp. 565–569, Sept. 2017.

[163] S. Greveling, F. van der Laan, H. C. Jagers, and D. van Oosten, "Polarization of a Bose-Einstein Condensate of Photons in a Dye-Filled Microcavity," *arXiv:1712.08426 [cond-mat, physics:quant-ph]*, Dec. 2017.

[164] S. Greveling, K. L. Perrier, and D. van Oosten, "Density distribution of a Bose-Einstein condensate of photons in a dye-filled microcavity," *Physical Review A*, vol. 98, p. 013810, July 2018.

[165] B. T. Walker, L. C. Flatten, H. J. Hesten, F. Mintert, D. Hunger, A. A. P. Trichet, J. M. Smith, and R. A. Nyman, "Driven-dissipative non-equilibrium Bose–Einstein condensation of less than ten photons," *Nature Physics*, vol. 14, p. 1173, Dec. 2018.

[166] R. Weill, A. Bekker, B. Levit, M. Zhurahov, and B. Fischer, "Thermalization of one-dimensional photon gas and thermal lasers in erbium-doped fibers," *Optics Express*, vol. 25, pp. 18963–18973, Aug. 2017.

[167] R. Weill, A. Bekker, B. Levit, and B. Fischer, "Bose-Einstein condensation of photons in an erbium-ytterbium co-doped fiber cavity," *Nature Communications*, vol. 10, p. 747, Feb. 2019.

[168] A. Chiocchetta, A. Gambassi, and I. Carusotto, "Laser Operation and Bose-Einstein Condensation: Analogies and Differences," in *Universal Themes of Bose-Einstein Condensation*, pp. 409–423, Cambridge University Press, 2017.

[169] J. Klaers, J. Schmitt, T. Damm, F. Vewinger, and M. Weitz, "Statistical Physics of Bose-Einstein-Condensed Light in a Dye Microcavity," *Physical Review Letters*, vol. 108, p. 160403, Apr. 2012.

[170] P. Kirton and J. Keeling, "Nonequilibrium Model of Photon Condensation," *Physical Review Letters*, vol. 111, p. 100404, Sept. 2013.

[171] P. Kirton and J. Keeling, "Thermalization and breakdown of thermalization in photon condensates," *Physical Review A*, vol. 91, p. 033826, Mar. 2015.

[172] H. J. Hesten, R. A. Nyman, and F. Mintert, "Decondensation in Nonequilibrium Photonic Condensates: When Less Is More," *Physical Review Letters*, vol. 120, p. 040601, Jan. 2018.

[173] R. A. Nyman and B. T. Walker, "Bose-Einstein condensation of photons from the thermodynamic limit to small photon numbers," *Journal of Modern Optics*, vol. 65, pp. 754–766, Mar. 2018.

[174] M. Radonjić, W. Kopylov, A. Balaž, and A. Pelster, "Interplay of coherent and dissipative dynamics in condensates of light," *New Journal of Physics*, vol. 20, p. 055014, May 2018.

[175] J. Keeling, "Superfluid Density of an Open Dissipative Condensate," *Physical Review Letters*, vol. 107, p. 080402, Aug. 2011.

[176] I. Carusotto and C. Ciuti, "Quantum fluids of light," *Reviews of Modern Physics*, vol. 85, pp. 299–366, Feb. 2013.

[177] L. M. Sieberer, S. D. Huber, E. Altman, and S. Diehl, "Dynamical Critical Phenomena in Driven-Dissipative Systems," *Physical Review Letters*, vol. 110, p. 195301, May 2013.

[178] D. Vorberg, W. Wustmann, R. Ketzmerick, and A. Eckardt, "Generalized Bose-Einstein Condensation into Multiple States in Driven-Dissipative Systems," *Physical Review Letters*, vol. 111, p. 240405, Dec. 2013.

[179] E. Altman, L. M. Sieberer, L. Chen, S. Diehl, and J. Toner, "Two-Dimensional Superfluidity of Exciton Polaritons Requires Strong Anisotropy," *Physical Review X*, vol. 5, p. 011017, Feb. 2015.

[180] P. Kirton and J. Keeling, "Superradiant and lasing states in driven-dissipative Dicke models," *New Journal of Physics*, vol. 20, p. 015009, Jan. 2018.

[181] A. Strashko, P. Kirton, and J. Keeling, "Organic Polariton Lasing and the Weak to Strong Coupling Crossover," *Physical Review Letters*, vol. 121, p. 193601, Nov. 2018.

[182] N. Shammah, S. Ahmed, N. Lambert, S. De Liberato, and F. Nori, "Open quantum systems with local and collective incoherent processes: Efficient numerical simulations using permutational invariance," *Physical Review A*, vol. 98, p. 063815, Dec. 2018.

[183] P. Kirton, M. M. Roses, J. Keeling, and E. G. D. Torre, "Introduction to the Dicke Model: From Equilibrium to Nonequilibrium, and Vice Versa," *Advanced Quantum Technologies*, vol. 2, no. 1-2, p. 1800043, 2019.

[184] Wikipedia, "Normal mode." https://en.wikipedia.org/wiki/Normal_mode. Accessed 7/5/2019.

[185] Q. Le-Van, E. Zoethout, E.-J. Geluk, M. Ramezani, M. Berghuis, and J. G. Rivas, "Enhanced Quality Factors of Surface Lattice Resonances in Plasmonic Arrays of Nanoparticles," *Advanced Optical Materials*, vol. 7, no. 6, p. 1801451, 2019.

[186] R. J. Moerland, T. K. Hakala, J.-P. Martikainen, H. T. Rekola, A. I. Väkeväinen, and P. Törmä, "Strong Coupling Between Organic Molecules and Plasmonic Nanostructures," in *Quantum Plasmonics* (S. I. Bozhevolnyi, L. Martin-Moreno, and F. Garcia-Vidal, eds.), Springer Series in Solid-State Sciences, pp. 121–150, Cham: Springer International Publishing, 2017.

[187] R. Guo, T. K. Hakala, and P. Törmä, "Geometry dependence of surface lattice resonances in plasmonic nanoparticle arrays," *Physical Review B*, vol. 95, p. 155423, Apr. 2017.

[188] J. D. Joannopoulos, S. G. Johnson, J. N. Winn, and R. D. Meade, *Photonic Crystals: Molding the Flow of Light*. Princeton University Press, 2nd ed., 2008.

[189] P. S. J. Russell, "Photonic band gaps," *Physics World*, vol. 5, pp. 37–42, Aug. 1992.

[190] W. L. Barnes, T. W. Preist, S. C. Kitson, and J. R. Sambles, "Physical origin of photonic energy gaps in the propagation of surface plasmons on gratings," *Physical Review B*, vol. 54, pp. 6227–6244, Sept. 1996.

[191] U. Fano, "Effects of Configuration Interaction on Intensities and Phase Shifts," *Physical Review*, vol. 124, pp. 1866–1878, Dec. 1961.

[192] B. Luk'yanchuk, N. I. Zheludev, S. A. Maier, N. J. Halas, P. Nordlander, H. Giessen, and C. T. Chong, "The Fano resonance in plasmonic nanostructures and metamaterials," *Nature Materials*, vol. 9, pp. 707–715, Sept. 2010.

[193] A. E. Miroshnichenko, S. Flach, and Y. S. Kivshar, "Fano resonances in nanoscale structures," *Reviews of Modern Physics*, vol. 82, pp. 2257–2298, Aug. 2010.

[194] V. Giannini, Y. Francescato, H. Amrania, C. C. Phillips, and S. A. Maier, "Fano Resonances in Nanoscale Plasmonic Systems: A Parameter-Free Modeling Approach," *Nano Letters*, vol. 11, pp. 2835–2840, July 2011.

[195] B. Gallinet and O. J. F. Martin, "Ab initio theory of Fano resonances in plasmonic nanostructures and metamaterials," *Physical Review B*, vol. 83, p. 235427, June 2011.

[196] H. T. Rekola, *Ensembles of Plasmonic Nanoparticles*. Aalto University, 2018.

[197] Wikipedia, "Franck-Condon principle." https://en.wikipedia.org/wiki/Franck-Condon_principle. Accessed 30/5/2019.

[198] R. C. Hilborn, "Einstein coefficients, cross sections, f values, dipole moments, and all that," *arXiv:physics/0202029*, 2002.

[199] G. Bjork and Y. Yamamoto, "Analysis of semiconductor microcavity lasers using rate equations," *IEEE Journal of Quantum Electronics*, vol. 27, pp. 2386–2396, Nov. 1991.

[200] T. P. H. Sidiropoulos, *Enhanced Light-Matter Interactions in Laser Systems Incorporating Metal-Based Optical Confinement*. Imperial College London, 2015.

[201] L. Novotny, "Strong coupling, energy splitting, and level crossings: A classical perspective," *American Journal of Physics*, vol. 78, pp. 1199–1202, Oct. 2010.

[202] M. O. Scully and M. S. Zubairy, *Quantum Optics*. Cambridge University Press, 1997.

[203] Sigma-Aldrich, "IR laser dyes, Rhodamine 6G, DCM, Styryl 9M." https://www.sigmaaldrich.com/finland.html. Accessed 2/6/2019.

[204] Wikipedia, "Rhodamine 6G." https://en.wikipedia.org/wiki/Rhodamine_6G. Accessed 15/6/2019.

[205] FEW-Chemicals, "FEW Cyanine Dyes: 790-819 nm." https://www.few.de/en/menue-oben/spezialchemikalien/funktionelle-farbstoffe/loesungsmittelloesliche-cyanine/790-819-nm/. Accessed 2/6/2019.

[206] OMLC, "Rhodamine 6G absorption and emission spectra." https://omlc.org/spectra/PhotochemCAD/html/083.html. Accessed 2/6/2019.

[207] Sirah-Lasertechnik, "Laser Dyes 532 nm." http://www.sirah.com/dyes-accessories/laser-dyes-532-nm. Accessed 2/6/2019.

[208] Kremer-Pigmente, "Perylene Red." https://www.kremer-pigmente.com/de. Accessed 2/6/2019.

[209] R. Guo, *Dispersions and Light-Matter Interactions in Plasmonic Lattices of Different Geometries*. Aalto University, 2018.

[210] V. Lucarini, J. J. Saarinen, K.-E. Peiponen, and E. M. Vartiainen, *Kramers-Kronig Relations in Optical Materials Research*. Springer Series in Optical Sciences, Berlin: Springer, 2005.

[211] P. Vasa, W. Wang, R. Pomraenke, M. Lammers, M. Maiuri, C. Manzoni, G. Cerullo, and C. Lienau, "Real-time observation of ultrafast Rabi oscillations between excitons and plasmons in metal nanostructures with J-aggregates," *Nature Photonics*, vol. 7, pp. 128–132, Feb. 2013.

[212] P. Sperber, W. Spangler, B. Meier, and A. Penzkofer, "Experimental and theoretical investigation of tunable picosecond pulse generation in longitudinally pumped dye laser generators and amplifiers," *Optical and Quantum Electronics*, vol. 20, pp. 395–431, Sept. 1988.

[213] C. Sauvan, J. P. Hugonin, I. S. Maksymov, and P. Lalanne, "Theory of the Spontaneous Optical Emission of Nanosize Photonic and Plasmon Resonators," *Physical Review Letters*, vol. 110, p. 237401, June 2013.

[214] J.-P. Martikainen, T. K. Hakala, H. T. Rekola, and P. Törmä, "Modelling lasing in plasmonic nanoparticle arrays," *Journal of Optics*, vol. 18, no. 2, p. 024006, 2016.

[215] C. J. Pethick and H. Smith, *Bose-Einstein Condensation in Dilute Gases*. Cambridge University Press, 2nd ed., Sept. 2008.

[216] D. Bajoni, P. Senellart, A. Lemaître, and J. Bloch, "Photon lasing in GaAs microcavity: Similarities with a polariton condensate," *Physical Review B*, vol. 76, p. 201305, Nov. 2007.

[217] K. Santhosh, O. Bitton, L. Chuntonov, and G. Haran, "Vacuum Rabi splitting in a plasmonic cavity at the single quantum emitter limit," *Nature Communications*, vol. 7, p. ncomms11823, June 2016.

[218] R. Chikkaraddy, B. de Nijs, F. Benz, S. J. Barrow, O. A. Scherman, E. Rosta, A. Demetriadou, P. Fox, O. Hess, and J. J. Baumberg, "Single-molecule strong coupling at room temperature in plasmonic nanocavities," *Nature*, vol. 535, pp. 127–130, July 2016.

[219] A. Thomas, L. Lethuillier-Karl, K. Nagarajan, R. M. A. Vergauwe, J. George, T. Chervy, A. Shalabney, E. Devaux, C. Genet, J. Moran, and T. W. Ebbesen, "Tilting a ground-state reactivity landscape by vibrational strong coupling," *Science*, vol. 363, pp. 615–619, Feb. 2019.

[220] D. S. Dovzhenko, S. V. Ryabchuk, Y. P. Rakovich, and I. R. Nabiev, "Light–matter interaction in the strong coupling regime: Configurations, conditions, and applications," *Nanoscale*, vol. 10, no. 8, pp. 3589–3605, 2018.

[221] R. F. Ribeiro, L. A. Martínez-Martínez, M. Du, J. Campos-Gonzalez-Angulo, and J. Yuen-Zhou, "Polariton chemistry: Controlling molecular dynamics with optical cavities," *Chemical Science*, vol. 9, no. 30, pp. 6325–6339, 2018.

[222] J. Flick, N. Rivera, and P. Narang, "Strong light-matter coupling in quantum chemistry and quantum photonics," *Nanophotonics*, vol. 7, no. 9, pp. 1479–1501, 2018.

[223] M. Hertzog, M. Wang, J. Mony, and K. Börjesson, "Strong light–matter interactions: A new direction within chemistry," *Chemical Society Reviews*, vol. 48, no. 3, pp. 937–961, 2019.

[224] N. G. Berloff, M. Silva, K. Kalinin, A. Askitopoulos, J. D. Töpfer, P. Cilibrizzi, W. Langbein, and P. G. Lagoudakis, "Realizing the classical *XY* Hamiltonian in polariton simulators," *Nature Materials*, vol. 16, pp. 1120–1126, Nov. 2017.

[225] M. Heyl, "Dynamical quantum phase transitions: A review," *Reports on Progress in Physics*, vol. 81, p. 054001, Apr. 2018.

[226] N. Somaschi, L. Mouchliadis, D. Coles, I. E. Perakis, D. G. Lidzey, P. G. Lagoudakis, and P. G. Savvidis, "Ultrafast polariton population build-up mediated by molecular phonons in organic microcavities," *Applied Physics Letters*, vol. 99, p. 143303, Oct. 2011.

[227] K. Yamashita, U. Huynh, J. Richter, L. Eyre, F. Deschler, A. Rao, K. Goto, T. Nishimura, T. Yamao, S. Hotta, H. Yanagi, M. Nakayama, and R. H. Friend, "Ultrafast Dynamics of Polariton Cooling and Renormalization in an Organic Single-Crystal Microcavity under Nonresonant Pumping," *ACS Photonics*, vol. 5, pp. 2182–2188, June 2018.

[228] T. Gao, P. S. Eldridge, T. C. H. Liew, S. I. Tsintzos, G. Stavrinidis, G. Deligeorgis, Z. Hatzopoulos, and P. G. Savvidis, "Polariton condensate transistor switch," *Physical Review B*, vol. 85, p. 235102, June 2012.

[229] D. Ballarini, M. De Giorgi, E. Cancellieri, R. Houdré, E. Giacobino, R. Cingolani, A. Bramati, G. Gigli, and D. Sanvitto, "All-optical polariton transistor," *Nature Communications*, vol. 4, p. 1778, Apr. 2013.

[230] A. V. Zasedatelev, A. V. Baranikov, D. Urbonas, F. Scafirimuto, U. Scherf, T. Stöferle, R. F. Mahrt, and P. G. Lagoudakis, "A room-temperature organic polariton transistor," *Nature Photonics*, vol. 13, p. 378, June 2019.

[231] F. Boitier, A. Godard, E. Rosencher, and C. Fabre, "Measuring photon bunching at ultrashort timescale by two-photon absorption in semiconductors," *Nature Physics*, vol. 5, pp. 267–270, Apr. 2009.

[232] L. Gao, J. Liang, C. Li, and L. V. Wang, "Single-shot compressed ultrafast photography at one hundred billion frames per second," *Nature*, vol. 516, pp. 74–77, Dec. 2014.

[233] F. Herrera and F. C. Spano, "Theory of Nanoscale Organic Cavities: The Essential Role of Vibration-Photon Dressed States," *ACS Photonics*, vol. 5, pp. 65–79, Jan. 2018.

[234] J. del Pino, F. A. Y. N. Schröder, A. W. Chin, J. Feist, and F. J. Garcia-Vidal, "Tensor Network Simulation of Non-Markovian Dynamics in Organic Polaritons," *Physical Review Letters*, vol. 121, p. 227401, Nov. 2018.

Physics is a natural science that studies the surrounding nature: matter, energy, and motion, in space and time. Interactions, forces and the exchange of energy create an incredibly complex universe we are living in. Physicists explore the laws of nature, construct theories and mathematical models, and validate the hypotheses and theories by experimental observations. In essence, physics is an experimental and exact science.

In this dissertation, I have studied the interaction of light and metallic nanoparticles combined with organic dye molecules. I will introduce the quantum mechanical phenomena of lasing and Bose-Einstein condensation of quasiparticles, particles that are not real particles but composition of light and matter.

A dissertation is just a little stab into the darkness of unknown, an attempt to widen our common scientific knowledge. I believe this book has fulfilled its purpose and I wish you exciting moments in exploring it, and beyond...

ISBN 978-952-60-8860-0 (printed)
ISBN 978-952-60-8861-7 (pdf)
ISSN 1799-4934 (printed)
ISSN 1799-4942 (pdf)

Aalto University
School of Science
Department of Applied Physics
www.aalto.fi

BUSINESS + ECONOMY

ART + DESIGN + ARCHITECTURE

SCIENCE + TECHNOLOGY

CROSSOVER

DOCTORAL DISSERTATIONS

Aalto-DD 227/2019